©2015

Zhichao Hu

ALL RIGHTS RESERVED

LUMINESCENT METAL-ORGANIC FRAMEWORKS FOR CHEMICAL SENSING AND SOLID-STATE LIGHTING

by

ZHICHAO HU

A dissertation submitted to the

Graduate School-New Brunswick

Rutgers, The State University of New jersey

In partial fulfillment of the requirements

For the degree of

Doctor of Philosophy

Graduate Program in Chemistry and Chemical Biology

Written under the direction of

Jing Li

And approved by

_____

_____

_____

_____

New Brunswick, New Jersey

May 2015

ABSTRACT OF THE DISSERTATION

Luminescent metal-organic frameworks for chemical sensing and solid-state lighting

ZHICHAO HU

Dissertation Director:

Jing Li

Luminescent metal-organic frameworks (LMOFs) are crystalline solids constructed via self-assembly of metal cations and organic ligands. The organic ligands often contain aromatic moieties that are subject to excitation, giving rise to optical emission upon irradiation. Utilizing this ligand-based emission, the applications of LMOFs to chemical sensing and solid-state lighting are explored.

LMOFs' tunable porosity (non-porous LMOFs are not the focus of this study) and easy-to-functionalize surface enable them to selectively capture targeted analytes. By monitoring the changes in their optical emission profiles caused by strong guest-host interactions, the accurate identification of analytes is achieved. The electron and energy transfer mechanisms which govern the fluorescence signal transduction are also studied by a combination of experimental and computational (density functional theory or DFT) approaches.

LMOFs are also strong candidates as rare-earth-free phosphors for solid-state lighting. The immobilization of molecular chromophores into rigid LMOF backbones

inhibits the non-radiative decay caused by ligand rotation, vibration, and torsion, therefore enhances the quantum efficiency of the resulting compounds. The prescreening of the electronic properties of molecular chromophores through a computational (DFT) method facilitates the design of LMOF phosphors with desired emissions.

Overall, LMOFs' applications to chemical sensing and solid-state lighting are studied; the sensing mechanisms and principles of designing LMOF phosphors are also addressed.

ACKNOWLEDGEMENTS

I would like to take this opportunity to express my deepest gratitude to my advisor, Prof. Jing Li. I thank her for her excellent research projects, her diligent mentorship, and her always insightful suggestions, without which I might well have dropped out of the program years ago. In my dark moments of self-doubt, and there have been many, she was always there, taking me under her wing. Her dedication to research and her "true love" to science as she describes it, constantly motivate me to overcome the hurdles along the way, and to make it this far. I thank her from the bottom of my heart.

I would also like to thank my previous and present advisory committee members, Profs. Teddy Asefa, Xumu Zhang, Ralf Warmuth, Karsten Krogh-Jespersen, and Dr. Long Pan, for their generous support; my previous and present group members, especially Dr. Kunhao Li, Dr. Sanhita Pramanik, Dr. Debasis Banerjee, Dr. Haohan Wu, William P. Lustig, David J. Golembieski, and Aaminah b'Hat, Dr. Xiao Zhang, Dr. Qihan Gong, Wei Liu, Hao Wang, Dr. Mojgan Roushan, and Voshadhi Amarasinghe, whom I worked with very closely; my collaborators around the globe, especially Drs. Kui Tan and Guangxi Huang; my dear friends, especially Dr. Bu Wang and Jacob Baron; everyone else who helped me in any way in the past; last but not least my parents.

Table of Contents

ABSTRACT OF THE DISSERTATION ii

ACKNOWLEDGEMENTS iv

Table of Contents v

List of Tables vii

List of Figures viii

1. Introduction 1

1.1. The Origin of Luminescence in LMOFs 2

1.2. Utilizing the Optical Signals of LMOFs 3

1.3. The Advantages of LMOFs as Sensory Materials 5

1.4. The Advantages of LMOFs as Phosphors 8

2. LMOFs as Chemical Sensors 9

2.1. The Direct Detection of Explosive and Explosive-like Molecules 9

2.1.1. Introduction 9

2.1.2. Results and Discussion 12

2.1.3. Conclusions 23

2.2. The Indirect Detection of a Non-volatile Explosive 23

2.2.1. Introduction 23

2.2.2. Results and discussion 29

2.2.3. Conclusions 47

2.3. The Detection of Mycotoxins 48

2.3.1. Introduction 48

2.3.2. Results and Discussion 54

2.3.3. Conclusions 69

3. LMOFs as Phosphors 69

3.1. The Design and Characterization of a New LMOF Phosphor 69

3.1.1. Introduction 69

3.1.2. Results and Discussion 75

3.1.3. Conclusions 81

4. Conclusions 82

Appendices 83

List of Abbreviations 83

Notes on Computation 84

List of LMOFs 86

References 86

Acknowledgements of Previous Publications 93

List of Tables

Table 1. Single crystal data for LMOF-161 12

Table 2. Single crystal data for LMOF-201 30

Table 3. Single crystal data for LMOF-202 based on the SQUEEZE model 30

Table 4. Relative intensities of ν(C=O) bands for the ketone molecules adsorbed in LMOF-202' and LMOF-121' 37

Table 5. Single crystal data of LMOF-241 based on the SQUEEZE model 52

Table 6. Single crystal data of LMOF-212 based on the SQUEEZE model 61

Table 7. Single crystal data of LMOF-221 based on the SQUEEZE model 61

Table 8. Single crystal data of LMOF-292 62

Table 9. Summary of K_{sv} for AFB_1 68

Table 10. Single crystal data of LMOF-231 based on the SQUEEZE model 73

Table 11. Photophysical properties of H_4tcbpe and LMOF-231 77

List of Figures

Figure 1. Crystal structure illustration of [$Zn_2(ndc)_2P$]. a) Ball and stick model of the paddle-wheel SBU (Zn: aqua; O: red; N: blue; C: grey). b) Space-filling model demonstrating two-fold interpenetration. c) Simplified overall 3D framework with 1D channels along the *a*-axis. 12

Figure 2. Powder X-ray diffraction (PXRD) patterns of outgassed sample LMOF-161' (top) and as made sample LMOF-161 (middle) compared with the simulated pattern from single crystal data (bottom). 13

Figure 3. PXRD patterns of outgassed sample LMOF-162' (top) and as made sample LMOF-162 (middle) compared with the simulated pattern from single crystal data (bottom). 14

Figure 4. Thermogravimetric profiles of LMOF-161 (a) and 162 (b) under nitrogen flow. ...15

Figure 5. Optical absorption spectrum of LMOF-161 (red solid). Fluorescent emission of LMOF-161 (black solid), ndc (blue dashed), and bpe (blue dashed). Excitation wavelength was 300 nm. All measurements were carried out on solid samples. 16

Figure 6. Optical absorption spectrum of LMOF-162 (red solid). Fluorescent emission of LMOF-162 (black solid), ndc (blue dashed), bpe (blue dashed). Excitation wavelength was 300nm. All measurements were carried out on solid samples. 16

Figure 7. A 2D (color coded) map of analyte recognition of **2**. Data were taken after 5 minutes of exposure to analyte vapor at room temperature. Group-A (circle), Group-B (square), Group-C (triangle) and solvents (diamond). 18

Figure 8. Recyclability test on LMOF-162. Fluorescence was recovered by applying vacuum to the sample for 3 minutes followed by DMF vapor curing for 6 minutes. Nitromethane was used as a model analyte. Analyte vapor exposure time was 5 minutes. Red bar: emission

of sample before exposure. Blue bar: emission after exposure to nitromethane for 5 minutes. 19

Figure 9. Difference spectra of benzene, toluene, nitrobenzene and nitrotoluene upon adsorption into LMOF-162 at RT and equilibrium vapor pressures of analytes, referenced to the blank LMOF-162. The black dashed lines correspond to the analytes bands; The blue dashed lines correspond to LMOF-162 and indicate the perturbation of absorption bands of LMOF-162. (Courtesy of Dr. Kui Tan) 20

Figure 10. Schematic diagram showing the changes in the VB and CB of LMOF-162 when exposed to nitrobenzene (NB) and nitromethane (NM). (Courtesy of Dr. Chong Zheng) ...21

Figure 11. SEM images of LMOF-162 by solvothermal synthesis (top, scale bar 100 μm) and surfactant assisted method (bottom, scale bar 10 μm). 22

Figure 12. SBU of (a) LMOF-201 and (b) LMOF-202; (c) Illustrations of the connectivity of ligands (green) to the Zn core (aqua) and (d) a single cage of the framework; (e) The overall 3D structure of LMOF-202 viewing along the a axis. Colour code: White (H), Orange (C), Blue (N), Red (O), Aqua (Zn). 26

Figure 13. PXRD patterns of outgassed sample LMOF-201' (blue), diethyl ether washed sample (cyan), and as-made sample LMOF-201 (red) compared with the simulated pattern from the single crystal data (black). 27

Figure 14. PXRD patterns of outgassed sample LMOF-202' (blue), dichloromethane washed sample (cyan), and as-made sample LMOF-202 (red) compared with the simulated pattern from the single crystal data (black). 28

Figure 15. Thermogravimetric profile of LMOF-201 (blue) and LMOF-201' (burgundy) under nitrogen flow. 28

Figure 16. Thermogravimetric profile of LMOF-202 (blue) and LMOF-202' (burgundy) under nitrogen flow. 29

Figure 17. Calculated density of states (*DOS*) for LMOF-202 using Extended Hückel method. The solid curve denotes the total *DOS*. The shaded arearefers to the contribution from hfdc (left), bpy (middle), and Zn (right) respectively. The dashed horizontal line denotes the Fermi level. (Courtesy of Dr. Chong Zheng) 31

Figure 18. An illustration of molecular orbital energy levels of LMOF-121, LMOF-202, and analytes computed at B3LYP/SDD (on Zn), 6-31+G*(on H, C, N, O). 32

Figure 19. A comparison of fluorescence enhancement after 10 s exposure of LMOF-121' and LMOF-202' to the vapors of ketones.....32

Figure 20. A 2D colour coded map of ketones based on the fluorescence response of LMOF-202'. 33

Figure 21. PL emission spectra of LMOF-202' (black) and the same sample after 900 s exposure to dry RDX (red) at room temperature.....34

Figure 22. PL emission spectra of LMOF-202' (black) and the same sample after gradual exposure to a RDX sample freshly recrystallized in cyclohexanone at room temperature.....35

Figure 23. A summary of the emission intensity change of LMOF-202' after exposure to analytes for 10 s at room temperature.....35

Figure 24. IR absorption spectra of activated (top) LMOF-202' and (bottom) LMOF-121' reference to KBr pellet under N_2 purge. (Courtesy of Dr. Kui Tan) 36

Figure 25. IR absorption spectra of vapor phase analytes from top to bottom: acetone, 2-octanone, cyclpentanone, cyclohexanone. (Courtesy of Dr. Kui Tan) 36

Figure 26. IR absorption spectra of adsorbed ketone molecules: acetone, 2-octanone, cyclopentanone, cylcohexanone in LMOF-202' (top) and LMOF-121' (bottom) referenced

to IR spectrum of blank LMOF samples respectively. The spectra were recorded after exposing LMOF samples to vapors for 3 min. (Courtesy of Dr. Kui Tan) 37

Figure 27. (a) IR spectra of adsorbed acetone in LMOF-202' (left) and LMOF-121' (right) under N_2 purge as a function of time. (b) Integrated areas of ν(C=O) band of adsorbed acetone decrease as a function of time. Blue, LMOF-121'; red, LMOF-202'. (Courtesy of Dr. Kui Tan).....38

Figure 28. Time-dependent IR spectra of adsorbed 2-octanone, cyclopentanone and cyclohexanone in LMOF-202' under N_2 purge. Blue, data recorded within 0.5 min; red, after 5.4 min. (Courtesy of Dr. Kui Tan).....39

Figure 29. Optical adsorption spectra of solid samples of LMOF-121, LMOF-201, and LMOF-202. 40

Figure 30. (a) Emission spectra of ketones (solid lines) at λ_{ex} = 300 nm and UV absorbance of LMOF-121' (dashed blue) and LMOF-202' (dashed burgundy). (b) UV absorbance of DNT (dashed blue) and emission spectra of LMOF-121' (solid blue, λ_{ex} = 280 nm) and LMOF-202' (solid burgundy, λ_{ex} = 300 nm).....41

Figure 31. Heat of adsorption of acetone in LMOF-121 (red) and LMOF-202 (black). 42

Figure 32. (a) Quenching of the fluorescence of LMOF-121 upon the incremental addition of DNT (10 μL, 0.01 M aliquot). (b) Stern-Volmer plot of LMOF-121 showing the quenching efficiency of DNT. (c) Quenching of the fluorescence of LMOF-121 upon the incremental addition of lower concentration DNT (10 μL, 0.001 M aliquot). (d) Detection limit determined from (c): DNT = 4.98 μM or 0.91 μg/mL, from this point on, a steeper slope is observed. 45

Figure 33. (a) Quenching of the fluorescence of LMOF-202 upon the incremental addition of DNT (10 μL, 0.01 M aliquot). (b) Stern-Volmer plot of LMOF-202 showing the quenching efficiency of DNT.....46

Figure 34. (a) The primary building unit showcasing a tetrahedrally coordinated Zn center. (b) A segment cut along the c axis featuring a hexagonal cage. (c) Ligand simplification: bpdc as a 2-c node and tppe as a 4-c node. (d) Simplified framework with 3-fold interpenetration and distorted hexagonal channels along the c axis. (C: grey, N: blue, O: red, and Zn: aqua; H is omitted for clarity.) 51

Figure 35. (a) The excitation (dotted blue) and emission (solid red) spectra of LMOF-241 in DCM. (b) Emission spectra of LMOF-241 with the incremental addition of AFB_1 in DCM. (c) The Stern-Volmer curves acquired at λ_{ex} = 340 nm and λ_{ex} = 410 nm (insert) for AFB_1 (red dot), AFB_2 (orange triangle), AFG_1 (green dimand), and OTA (blue square). 54

Figure 36. SV curves for AFB_1 (a) and AFB_2 (b).....56

Figure 37. (a) Limit of detection of AFB_1 determination. (b) is a zoom-in of (a). 57

Figure 38. Calculated frontier orbital energies for LMOF-241 (fragment model) and analytes at B3LYP/DGDZVP.....58

Figure 39. (a) Molar absorptivity of AFB1 (dotted red), AFB_2 (dotted orange), AFG_1 (dotted green), and OTA (dotted blue), and the emission spectrum of LMOF-241 in DCM (λ_{ex} = 340 nm). (b) Excitation spectra (dotted lines) and emission spectra (solid lines, λ_{ex} = 340 nm) of AFG_1 (green), and OTA (blue) in DCM with intensity normalized to concentration.....59

Figure 40. An illustration of the formation of a series of LMOFs with the paddle-wheel type SBU. 61

Figure 41. (a) The PL titration curves of LMOF-211 with the addition of AFB_1 (λ_{ex} = 300 nm). (b) The Stern-Volmer curve of LMOF-211. 64

Figure 42. (a) The PL titration curves of LMOF-221 with the addition of AFB_1 (λ_{ex} = 300 nm). (b) The Stern-Volmer curve of LMOF-221. 65

Figure 43. (a) The PL titration curves of LMOF-281 with the addition of AFB_1 (λ_{ex} = 325 nm). (b) The Stern-Volmer curve of LMOF-281. 66

Figure 44. (a) The PL titration curves of LMOF-282 with the addition of AFB_1 (λ_{ex} = 350 nm). (b) The Stern-Volmer curve of LMOF-282. 67

Figure 45. (a) The PL titration curves of LMOF-292 with the addition of AFB_1 (λ_{ex} = 350 nm). (b) The Stern-Volmer curve of LMOF-292. 68

Figure 46. Estimated HOMO-LUMO energy gaps of ligands at B3LYP/DGDZVP. ΔE is normalized to the experimental value of L_7 (or H_4tcbpe) extrapolated from the diffuse reflectance spectrum. 71

Figure 47. (a) A chain formed along the c axis containing alternating eight-membered rings. (b) An illustration of the chain emphasizing the alternating rings. (c) The polyhedral representation of the SBU as an infinite rod of edge-sharing tetrahedra. (d) The tcbpe ligand simplified as a butterfly shape. (e) The overall simplified structure of LMOF-231 showing 1D rod SBU and 1D open channel along the c axis. Color code: H (white in (d), omitted for clarity in (a) and (c)), C (grey), O (red), Zn (aqua). 73

Figure 48. PXRD patterns of actived sample LMOF-231' (top), as-made sample LMOF-231 (middle), and simulated pattern from the single crystal data (bottom). 74

Figure 49. Thermogravimetric profile of H_4tcbpe (blue) and LMOF-231 (red) under nitrogen flow. 75

Figure 50. (a) Optical absorption spectra of H_4tcbpe, LMOF-231, and LMOF-231'. (b) Excitation spectra of H_4tcbpe (black dotted) and LMOF-231' (red dotted). Emission spectra of H_4tcbpe (black solid) and LMOF-231' (red solid) at λ_{ex} = 455 nm. (c) Emission spectra of H_4tcbpe, LMOF-231', and solvent exchanged LMOFs. Solvent abbreviation: ethyl acetate (EA), acetophenone (AP), N,N'-diethylformamide (DEF). All emission spectra were acquired with λ_{ex} = 455 nm. 77

Figure 51. Excitation (dotted line) and emission (solid line) spectra of LMOF-231' (red) and YAG:Ce^{3+} (black) 77

Figure 52. CIE coordionates of YAG:Ce^{3+}, black dot, (0.43, 0.54), H_4tcbpe, burgundy dot, (0.39, 0.55), LMOF-231, pink dot, (0.39, 0.56), and LMOF-231', red dot, (0.42, 0.54) calculated from their emission spectra respectively (λ_{ex} = 455 nm) 79

Figure 53. (a) to (d). Blue LED bulb (455-460 nm, (a) and (b)) and plate (450-455 nm, (c) and (d)), before and after coating with solution-processed LMOF-231' to create PC-WLEDs, with the top and bottom rows corresponding to device states 'off' and 'on', respectively. (e) A flexible ribbon coated with LMOF-231' under day light, and blue light (450-470 nm, LED lamp, (e')) 80

1. Introduction

Metal-organic frameworks (MOFs) are a class of fascinating materials that are both fundamentally important and technologically relevant. They have been extensively studied for their rich structural chemistry[1-5] and potential applications in numerous areas,[6,7] including but not limited to, gas storage,[8-10] gas separation,[11-15] heterogeneous catalysis,[16-20] chemical sensing,[21-25] optoelectronics (ferroelectronics, non-linear optics, and LEDs),[26-30] energy storage and conversion (batteries and solar cells),[31-36] drug delivery and bio-imaging.[37-39] MOFs, as indicated by the name, are crystalline solids constructed via self-assembly of single metal cations (primary building unit or PBU) or metal clusters (secondary building unit or SBU) and organic ligands having multiple binding sites, forming one, two, or three dimensional extended coordination networks.[40] The organic ligands often contain aromatic or conjugated π moieties that are subject to excitation, giving rise to optical emission or photoluminescence (PL) upon irradiation. In addition, the metal components can also contribute to photoluminescence, in which case lanthanides[41] or various inorganic clusters[42-46] are often involved. Naturally, these properties of luminescent MOFs (LMOFs) can potentially be used for real-world applications. The PL in LMOFs can be utilized conveniently; often it does not require the fabrication of thin films, which, while proven possible in some cases, can be challenging with respect to the general pool of these materials.[47,48]

Given the nearly limitless choices of metal and ligand combinations, MOFs thrive on structural diversity and tunable chemical and physical properties. The intrinsic permanent porosity in a large number of MOFs further enables the adsorption of guest molecules and therefore enhances host-guest interactions, since the pore size and shape, chemical composition and surface environment within the pores can be finely controlled, and

therefore, the selective seizing of certain guest molecules is often times achieved. This merit of MOFs is the foundation of many well explored applications, especially in gas storage and separation. Additionally, the perturbation from adsorbed guest molecules can alter LMOFs' photoemission profiles, making them excellent candidates for chemosensing. The immobilization of molecular chromophores into rigid LMOFs inhibits non-radiative decay involving ligand rotation, vibration, and torsion, potentially enhancing the overall fluorescence of the resulting compounds; this anchoring effect is the foundation for LMOF-based phosphors.

1.1. The Origin of Luminescence in LMOFs

Luminescence can be defined as the emission of light upon absorption of energy under the condition that the energy source is not heat based, which refers to incandescence.[21,23,49,50] There are two main types of luminescence: fluorescence, which is a spin-allowed radiative transition from the lowest singlet excited state S_1 of the fluorophore to its singlet ground state S_0; and phosphorescence, which refers to the spin-forbidden radiative transition from the triplet state T_1 to ground state S_0.[21,23,49,50] Photoluminescence initiated by photo-excitation is one type of luminescence that is the major focus of this study.[21] Luminescence in MOFs generally arises from the building components: conjugated organic ligands and/or metal ions or clusters, although in some cases adsorbed guest molecules may also contribute to the emission. Organic linkers with aromatic moieties or extended π systems are commonly used in the construction of porous MOFs due to their rigid molecular backbone. The π electrons in these linkers contribute greatly to luminescence, which can be classified as linker based luminescence or ligand to ligand charge transfer (LLCT). As the organic fluorophores are immobilized in an ordered arrangement and in close proximity with one another in a MOF structure, the nature of their intermolecular communication can be altered resulting in

photoemissions that are different from their free form.[51] Ligand to metal charge transfer (LMCT) and metal to ligand charge transfer (MLCT) are also common among d^{10} transition metal based MOFs: LMCT is often observed in Zn (II) and Cd (II) compounds,[52,53] while MLCT is generally seen in Cu (I) and Ag (I) compounds.[45,54] It should be noted that these mechanisms are not mutually exclusive; more than one emission pathway can coexist in a competitive manner with another. Metal-centered luminescence is often found in lanthanide MOFs. Strongly photon absorbing linkers with efficient intersystem crossing are preferred in constructing lanthanide LMOFs because they ensure the delivery of excitation energy from their triplet excited states to the emissive states of lanthanides through an antenna effect.[21,41]

1.2. Utilizing the Optical Signals of LMOFs

The permanent porosity of many MOFs makes them stand out as a unique family of functional materials. Their intrinsically porous structures harbor nearly all of the major applications developed for this material class, many of which take advantage of the adsorption of guest molecules within the cavity of the framework. The capture of guest molecules in the pores allows them to be in close proximity with the organic walls or metal centers of the host structure, and thus, readily interact with the MOF. The perturbation induced by these guest molecules can alter multiple aspects of the physicochemical properties of the captor, including light absorption and emission profiles. Color change that is visible to the naked eye is arguably the most preferred signal for sensing, simply because it does not require instrumentation and represents the most convenient method of detection. In some cases, performing an exchange of solvent guest molecules will shift the emission energy and tune the color of the compound. Identification of a guest molecule can be realized by utilizing a guest-dependent color change. Some ionic species are also known to have a similar colorimetric effect.[55-57]

For LMOFs, in principle any change in their spectroscopic characteristics can potentially be used as a sensing signal, while the most commonly observed change is the fluorescence intensity. Depending on the electronic nature of the molecule being detected (also referred to as the analyte), either quenching or enhancement of the luminescence can occur. This can be attributed to either electron transfer or energy transfer between the analyte molecule and the LMOF, or a combination of the two.[49,58-66] Nitroaromatics, which are exemplary explosives or explosive-like molecules, are known as strong quenchers owing to their high electron affinity.[59,61,62,67] Paramagnetic metal ions, such as Mn^{2+}, Co^{2+}, Ni^{2+}, and Cu^{2+}, are also capable of quenching fluorescence since they can induce LMCT and relax the excitation energy through a non-radiative pathway.[21,68,69] On the other hand, electron rich species, such as benzene and its derivatives with electron donating substituents, can enhance fluorescence of certain systems (most common among ligand-based emissions), possibly due to their ability to donate an electron from an excited state to the LUMO or conduction band (CB) of the LMOF.[62,70-73]

Another method of luminescence sensing is "turn-on" detection, where the capture of an analyte molecule results in the shift of an emission peak or a new emission peak (typically in the visible range) evolving from a previously dark background.[74-76] For example, the selective binding of analyte molecules can trigger a strong emission of an originally low-emitting or non-emitting MOF, which is known as guest induced emission.[75] Focusing on the shifting of emission peaks or the evolution of a new peak has several advantages: first, monitoring the evolution of a new emission peak is more sensitive than comparing the changes in emission intensity of the same peak, which may translate to lower detection limits. Second, intensity change of an emission is not always specific; molecules of similar electronic properties tend to affect intensity in a similar fashion. For example, nitroaromatics can all act

as strong quenchers, and as such, judging solely by the changes in fluorescence intensity is often insufficient for identifying the individual nitroaromatic species. However, the host material can be designed to have strong interactions with a particular analyte molecule resulting in an additional energy shift of the emission peak. With the aid of this additional signal, more accurate identification of analyte molecules can be achieved. The guest-host chemistry involved in these processes is intriguing, and understanding this interaction is fundamental and vital to designing LMOFs with high selectivity and sensitivity for sensing applications.

Confinement of ligands (molecular chromophores) in rigid LMOFs inhibits or reduces ligand rotation, vibration, and torsion, molecular motions related to non-radiative decay; this anchoring effect could potentially enhance the overall fluorescence of the resulting compounds. Another benefit of the immobilization of molecular chromophores into LMOFs is increased thermal stability, as LMOFs are found more thermally robust then their constituent ligands. LMOFs are feasible candidate as new generation solid-state phosphors.

1.3. The Advantages of LMOFs as Sensory Materials

LMOFs are often compared with organic conjugate polymers when evaluating their performance as sensory materials. Their crystalline nature, diverse and easily modifiable structures and topology, permanent porosity, systematically tunable band gaps and electronic structures, and a wide range of physicochemical properties all highlight some of their advantages. Most notably, the sustainable pores within LMOFs provide a natural habitat for guest molecules. The capture of guest molecules within the pores not only increases the chances of guest-host interactions, but also pre-concentrates the guest molecule, which may be responsible for sensitive detection.[21,24] In addition, functional groups within the

framework, such as Lewis acidic or basic sites in the ligands, and/or open metal sites, further promote preferred analyte binding for selective detection. Thirdly, the electronic properties of an LMOF structure may be fine-tuned. For example, given the same metal center and network connectivity, band gaps can be varied by changing the size of the SBU and the degree of conjugation of the organic linkers.[77] Needless to say, changes to a framework's metal centers or their connectivity also lead to changes in band gaps and atomic compositions of the valence band (or HOMO) and/or conduction band (or LUMO). Such tunability is crucial for sensing applications as it directly relates to the optical absorption and emissions properties. Fourthly, immobilization of organic linkers in a rigid framework can potentially reduce non-radiative relaxation caused by free rotation and vibration of the linker, and therefore lead to stronger emissions.[78-80] Aggregation induced emission (AIE) is a perfect example: a low-emissive linker when in a dilute solution may exhibit strong fluorescence upon assembly into a rigid MOF structure.[51] Furthermore, MOFs generally have relatively high thermal-stability, and it is not uncommon for them to remain crystalline at a few hundred degrees Celsius. Fluorescent conjugate polymers typically lose their emission at elevated temperatures, especially upon melting or glassifying. Several MOFs have been reported to maintain their fluorescence at relatively high temperatures, and thus it becomes possible to utilize their fluorescence when a specific analyte's binding requires an elevated temperature.[74] Last but not the least, compared to amorphous materials, the highly ordered crystalline samples of MOFs allow precise and easy identification and characterization of their structures (e.g. by X-ray diffraction methods), making them perfect systems for investigating structure-property correlations and host-guest interactions. This merit has significant implications in both applications and fundamental studies. Overall, LMOFs have great potential as a unique class of sensory materials.

In order to fully explore the virtues of LMOFs as sensory materials, rational design, control, and construction of their structures become a necessity. The existing gas and hydrocarbon adsorption studies are among the most valuable assets for MOF based applications, and have profound significance in designing sensors with superb performance. When screening existing LMOFs as potential sensors, priority should be given to those that selectively adsorb targeted analytes. Precision for the adsorption of an analyte molecule is usually achieved through the accurate construction of a desired pore on the molecular level.[22,81] Size exclusivity is the most intuitive selection rule, where only molecules slimmer than the pore can be captured. Thus, controlling the pore size is seemingly the most obvious first step to consider when designing LMOF based sensors. The porosity of MOFs provides such a versatile platform to work with, and is subject to various chemical manipulations. Many physicochemical properties within the porous environment, such as hydrophobicity, polarity, polarizability, acidity and proton affinity, can be finely-tuned. By controlling the chemical environment of the pore, selective capture of targeted molecules can often be achieved. For instance, the incorporation of Lewis basic site (LBS) facilitates the attraction of metal ions[82] and the acidic 2,4,6-trinitrophenol (TNP)[66]. Earlier study also demonstrated the utilization of open metal site (OMS) for sensing small molecules.[83] In a recent case, the effective detection of NH_3 is realized by the preferential binding of this guest molecule at an OMS.[74] In another case, anion recognition is attained through the hydrogen bonding between analyte and terminal solvent molecule.[84] The electronic properties of LMOFs are also crucial with respect to their sensing behaviors. Electron and/or energy transfer between an LMOF and an analyte are the main reasons for a fluorescent response, and as such, rational design of a LMOF should aim at promoting these features. The introduction of highly conjugated linkers in a framework is expected to better attract aromatic or conjugated

analytes through π-π interactions.[85] The relative orbital energies of the CB (or LUMO) of LMOFs can be tailored by incorporating electron-donating or electron withdrawing groups into the ligands.[86] In terms of energy transfer, it has been demonstrated that the overlap between the emission spectrum of an LMOF and the absorption spectrum of a specific analyte induces a dramatic decrease in the fluorescence intensity of the LMOF.[66] The real-world use of LMOF sensors demands superb sensitivity and selectivity. As more and more LMOF sensors are being discovered, it is foreseeable that precise identification of a targeted analyte may eventually become possible by a cross-referencing method employing a series of LMOFs selected from a large library of sensory materials.

1.4. The Advantages of LMOFs as Phosphors

The vast majority of current commercially available solid-state phosphors, such as YAG:Ce^{3+}, predominantly reply on rare-earth elements. However, due to the increasing demand of these elements in many other high-tech applications, their prices have increased up to 49 times from 2001 to 2011. Utilizing ligand-based emission, LMOFs are strong candidates as substitutes for rare-earth-based phosphors. As potential phosphors, luminescent MOFs (LMOFs) have several intrinsic advantages: The diverse building components available for the construction of LMOFs offer various sources of fluorescence, which makes it possible to design phosphors independent of rare-earth elements or elements with adverse environmental impacts (such as cadmium and selenium) — the former are the essential ingredients in current commercially available inorganic phosphors, and the latter are the key components in quantum-dot based phosphors. The synthesis conditions for LMOFs are much milder than those for solid-state inorganic phosphors; the fabrication process only requires moderate heating or even no heating (e.g. reactions at room temperature), which conserves energy from the very beginning of their life cycle. Anchoring organic

chromophores into the rigid MOF backbone effectively inhibits or reduces non-radiative decay as a result of ligand rotation, vibration, and torsion, potentially enhancing the overall fluorescence of the resulting compounds. An added bonus is that LMOFs are often more thermally stable than their constituent ligands.

2. LMOFs as Chemical Sensors

2.1. The Direct Detection of Explosive and Explosive-like Molecules

2.1.1. Introduction

The selective and rapid detection of chemical explosives is of increasing importance in areas such as homeland security, civilian safety and environmental protection. From nitroaromatics to nitroaliphatics, chemical explosives encompass diverse groups of compounds.[61] Among them, high explosives such as RDX (1,3,5-trinitroperhydro-1,3,5-triazine) have extremely low vapor pressure (4.6×10^{-9} torr or 6×10^{-3} ppb)[87,88] and thus, effective detection of these species in the vapor-phase remains one of the most challenging tasks. Optical sensing is a common detection method, in which a luminescent active material is used and detection is achieved by changes in its optical signal response[61,89]. Fluorescent conjugated polymers represent a group of such materials.[59] Their detection is typically based on fluorescence quenching. Often, analytes with similar electronic properties lead to similar responses.[61,67] For instance, electron deficient molecules as a group can act as fluorescent quenchers.[59]

As a new class of crystalline porous materials, metal-organic frameworks (MOFs) have been investigated for their fluorescent properties[21,23] in addition to other applications such as catalysis,[21,43,90] gas storage and separation,[13,14,91-93] However, it was until very recently that MOFs were exploited for explosive detection.[94] We reported the first study demonstrating that highly fluorescent MOF $Zn_2(bpdc)_2(bpee)$ (or RPM3-Zn, bpdc = 4,4'-

biphenyldicarboxylate; bpee = 1,2-bis(4-pyridyl)ethylene) is capable of fast, sensitive, and reversible detection of trace vapors of explosive and taggant.[94,95] Subsequently, we carried out a more systematic study on [$Zn_2(oba)_2(bpy)$] (oba = 4,4'-oxybis(benzoate); bpy = 4,4'-bipyridine) that covered a broad range of analytes with different electronic properties.[62] We discussed the general response mechanism for MOF based sensors and offered possible explanations for the effect of electron-withdrawing (or electron-donating) groups on the fluorescence quench (or enhancement) behavior of aromatic analytes.

Despite recent progress on utilizing MOF-based sensors, no experimental work has been reported on their detection of RDX vapors to date. It is also important to mention that the majority of the current detection methodologies focus on the fluorescent intensity change (quenching/enhancing), which may be efficient in identifying analytes from different categories, but will be unable to distinguish analytes having similar properties (e.g. various nitroaromatics). Emission frequency (wavelength) shift may result from very strong analyte-sensor interactions (e.g. formation of an exciplex during excitation process) and is strongly structure dependent.[96-99] This phenomenon has hardly been explored for MOF sensory materials. Factoring in the frequency shift parameter can potentially add a new dimension to the detection map, and can form a powerful tool in effectively identifying and differentiating analytes on a two-dimensional (2D) basis. Herein we demonstrate this strategy with a new dynamic and microporous MOF and a closely related analogue as sensory materials with drastically enhanced selectivity and sensitivity for a variety of high explosives including RDX.

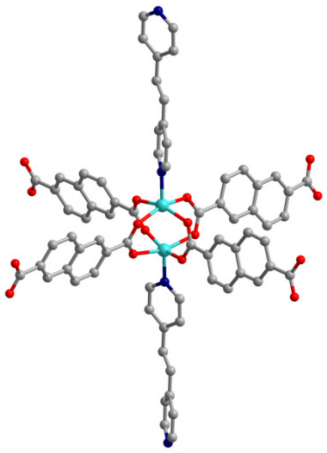

(a)

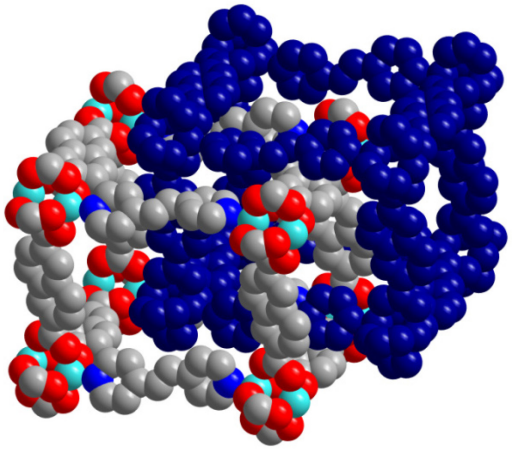

(b)

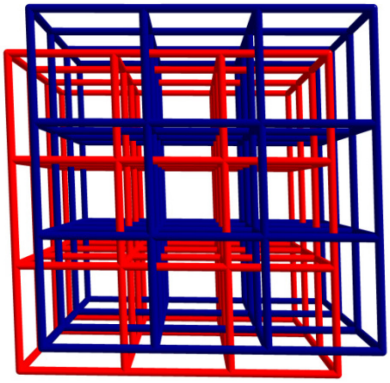

(c)

Figure 1. Crystal structure illustration of $[Zn_2(ndc)_2P]$. a) Ball and stick model of the paddle-wheel SBU (Zn: aqua; O: red; N: blue; C: grey). b) Space-filling model demonstrating two-fold interpenetration. c) Simplified overall 3D framework with 1D channels along the *a*-axis.

2.1.2. Results and Discussion

Single crystals of $[Zn_2(ndc)_2(bpe)]\cdot 2.5DMF\cdot 0.25H_2O$ (LMOF-161) (ndc = 2,6-naphthalenedicarboxylate; bpe = 1,2-bis(4-pyridyl)ethane; DMF = N,N'-dimethylformamide) were grown under solvothermal conditions. The crystal growth of LMOF-161 was controlled by adjusting the pH of the reaction mixture. Neutral or basic conditions did not favor the formation of LMOF-161. High quality pure phased crystals of LMOF-161 can only be acquired under acidic conditions. The crystal structure of LMOF-161 was determined by single crystal X-ray diffraction method (Table 1). The structure is built on a $Zn_2(ndc)_4$ paddle-wheel secondary building unit (SBU, Figure 1a) which connects to four identical units to form a two-dimensional net. The net is further bridged by the pillar bpe ligands to form a three-dimensional network. Two of such networks interpenetrate to result in the final structure (Figure 1b-c) containing one-dimensional channels. A closely related structure, $[Zn_2(ndc)_2(bpee)]\cdot 2.25DMF\cdot 0.5H_2O$ (LMOF-162), was synthesized according to the literature method.[100] Both compounds exhibit dynamic structure change (Figure 2 and Figure 3) upon removal of guest molecules (Figure 4) which is likely due to the absence of specific interaction between the two interpenetrated frameworks.[100]

Table 1. Single crystal data for LMOF-161

Compound	$[Zn_2(ndc)_2(bpe)]\cdot 2.5DMF\cdot 0.25H_2O$ (LMOF-161)
Formula	$C_{43.50}H_{43}N_{4.50}O_{11.25}Zn_2$
M	939.56
Crystal system	Monoclinic
Space group	C 2/m
a/Å	17.2783(14)
b/Å	19.6504(14)

c/Å	16.1383(13)
α/°	90.00
β/°	93.623(2)
γ/°	90.00
V, Å^3	5468.4(7)
Z	4
Temperature (K)	100(2)
μ (Mo Kα)mm^{-1}	0.929
D, g/cm^3	1.141
Reflections collected	36375
R1[a] [I > 2σ(*I*)]	0.0731
wR2[b] [I > 2σ(*I*)]	0.2231
Goodness-of-fit	1.087
CCDC No.	911294

[a] $R1 = \sum \left| F_o - F_c \right| / \sum \left| F_o \right|$
[b] $wR2 = \sum[w(F_o^2 - F_c^2)^2] / w(F_o^2)^2]^{1/2}$

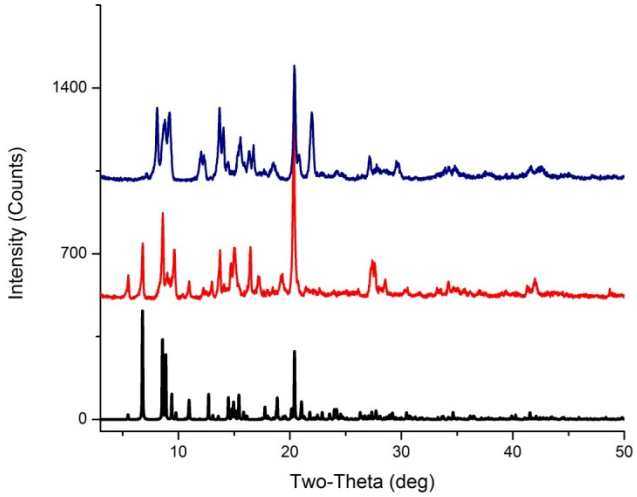

Figure 2. Powder X-ray diffraction (PXRD) patterns of outgassed sample LMOF-161' (top) and as made sample LMOF-161 (middle) compared with the simulated pattern from single crystal data (bottom).

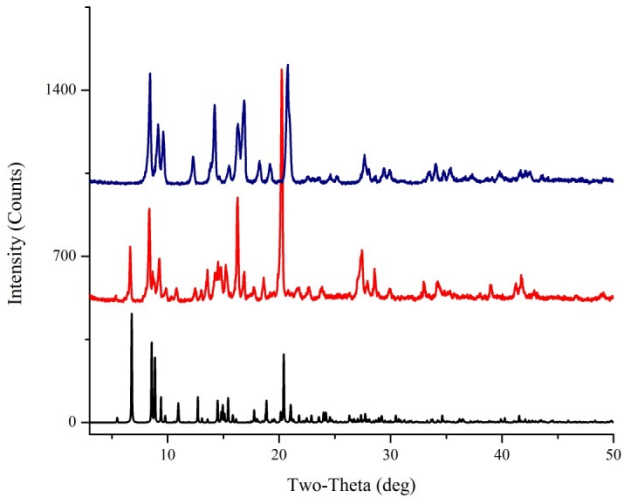

Figure 3. PXRD patterns of outgassed sample LMOF-162' (top) and as made sample LMOF-162 (middle) compared with the simulated pattern from single crystal data (bottom).

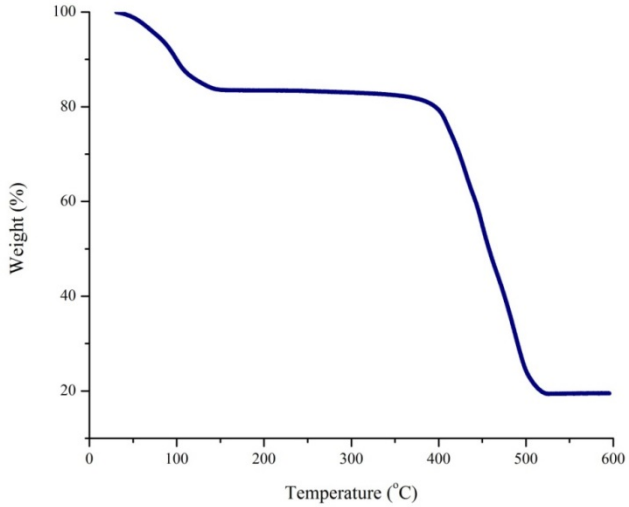

(a)

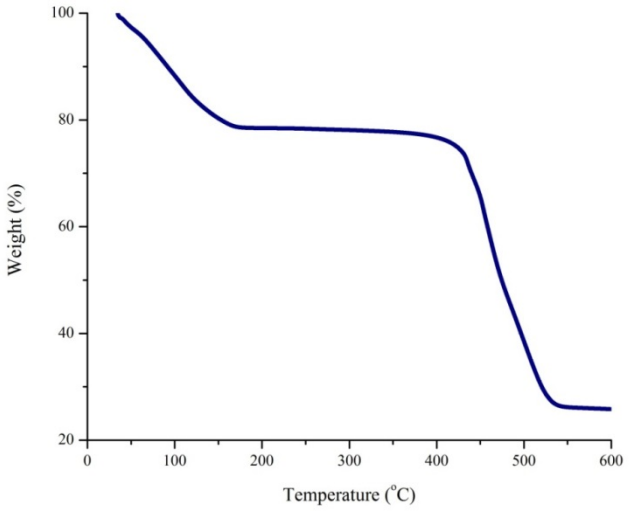

(b)

Figure 4. Thermogravimetric profiles of LMOF-161 (a) and 162 (b) under nitrogen flow.

Fluorescence measurements were performed on both compounds LMOF-161 and 162. Compared to their constituent ligands, the emission peaks of both LMOFs shift to lower energy region (Figure 5 and Figure 6). All detection experiments were carried out in vapor phase, under dynamic process, and set up as previously described, targeting two groups of analytes[62,94] and a number of other molecules. The electron deficient analytes (nitroaromatics, Group A) act as fluorescence quenchers, greatly reducing the fluorescence intensity of the MOFs after exposure. The electron rich analytes (Group B), on the other hand, enhance the fluorescence intensity of the MOFs. Fluorescence was also measured on a number of nitroaliphatics (Group-C) and other small molecules or solvents.

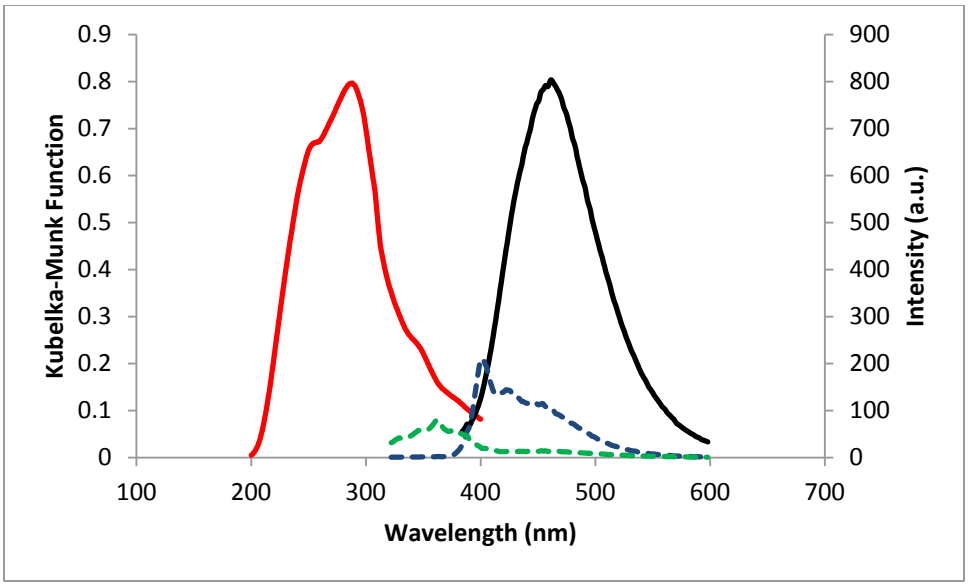

Figure 5. Optical absorption spectrum of LMOF-161 (red solid). Fluorescent emission of LMOF-161 (black solid), ndc (blue dashed), and bpe (blue dashed). Excitation wavelength was 300 nm. All measurements were carried out on solid samples.

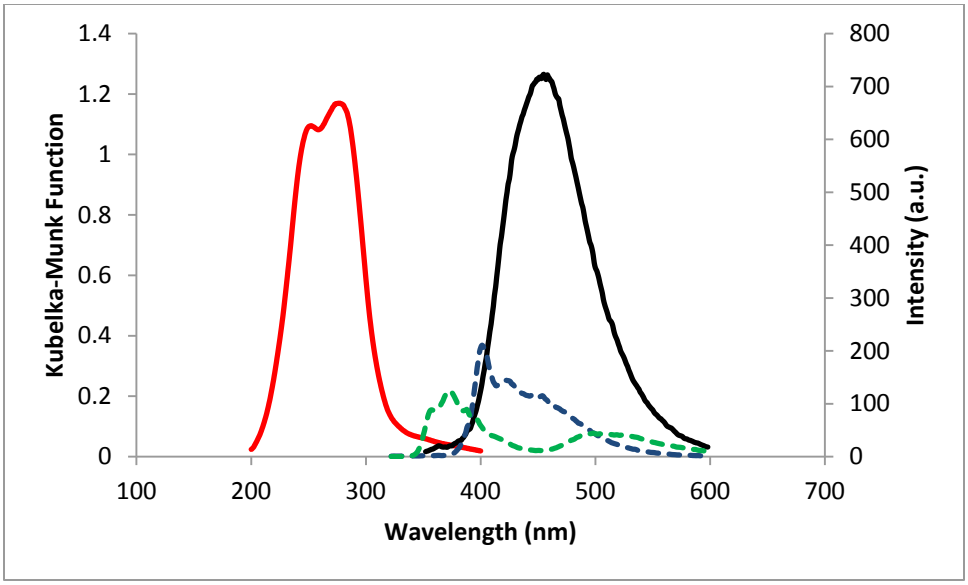

Figure 6. Optical absorption spectrum of LMOF-162 (red solid). Fluorescent emission of LMOF-162 (black solid), ndc (blue dashed), bpe (blue dashed). Excitation wavelength was 300nm. All measurements were carried out on solid samples.

Interestingly, an emission frequency shift was observed for both structures LMOF-161 and 162, indicative of strong analyte-MOF interactions. As stated above, this property is

very attractive and useful in terms of signal transduction: the evolution of peak placement at a specific wavelength is easily tracked and monitored, especially for high explosives such as RDX. Because of its exceedingly low vapor pressure at room temperature, detection of this explosive in vapor phase based on fluorescence intensity change is extremely challenging. Furthermore, analytes of similar chemical nature often affect the fluorescence intensity of the sensory material in a similar fashion. For example, DMNB (2,3-dimethyl-dinitrobutane) and RDX (1,3,5-trinitroperhydro-1,3,5-triazine) can both quench the fluorescent emission of LMOF-162 to a very similar extent. It is therefore almost impossible to unambiguously distinguish the two analytes solely by the change in their fluorescence intensity. However, in conjunction with fluorescence intensity change, the evaluation of emission frequency shift introduces a new and powerful variable for sensing data analysis and processing. When taking into consideration both factors, an analyte can be described as a point (emission peak shift, fluorescent intensity change) on a two-dimensional (2D) Cartesian coordinate system (emission peak shift, fluorescent intensity change). Thus pin-pointing an analyte on a 2D map becomes possible.

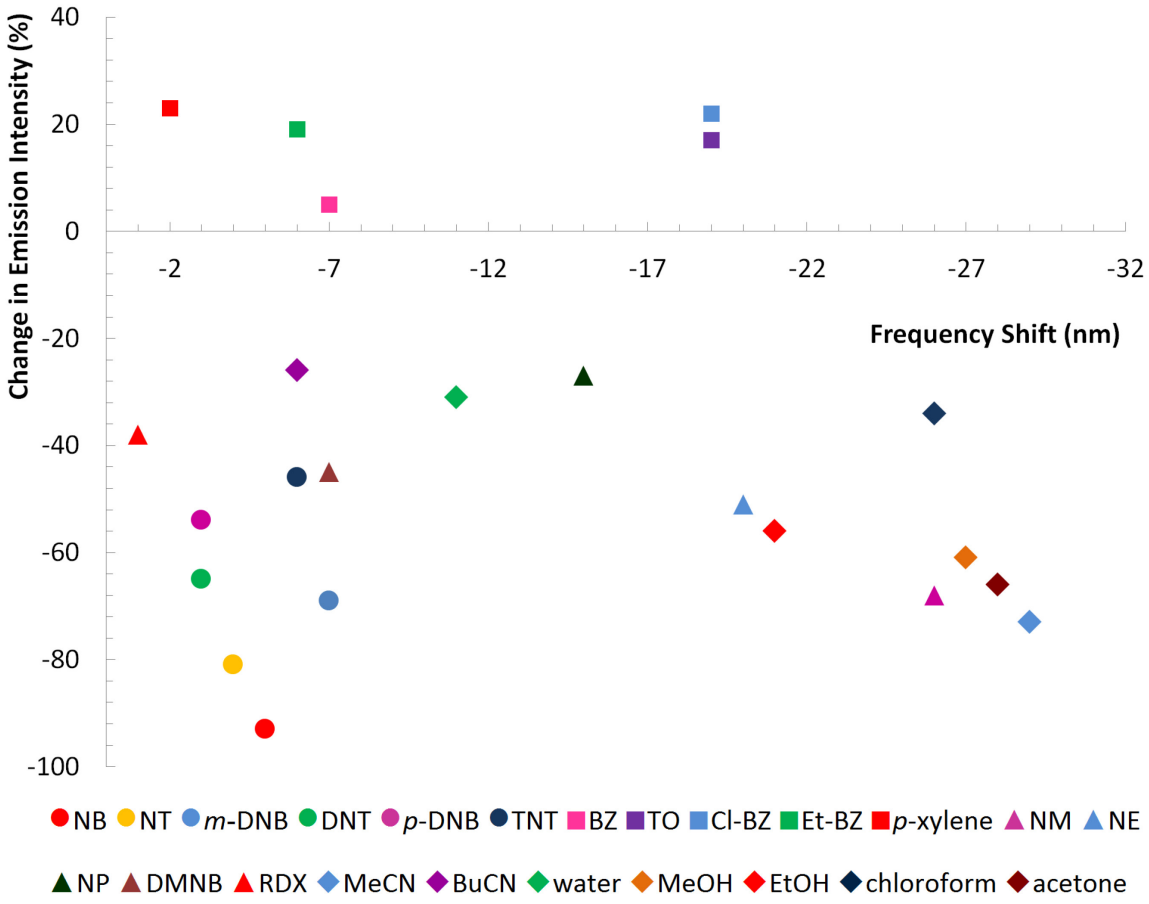

Figure 7. A 2D (color coded) map of analyte recognition of **2**. Data were taken after 5 minutes of exposure to analyte vapor at room temperature. Group-A (circle), Group-B (square), Group-C (triangle) and solvents (diamond).

Both MOF structures were examined for their ability to fingerprint analytes on a 2D map. Both fluorescence intensity change and emission frequency shift are plotted in Figure 7 for compound LMOF-162 after 5 minutes exposure to a variety of analyte vapors. All analytes selected in this study, including high explosives (e.g. RDX, TNT), explosive taggant (DMNB), analytes of Groups A, B, and C, are well spread on the 2D map and can be uniquely identified. Control experiments on a blank analyte or use of a single ligand as sensory material did not produce any notable response. Compared to our previous study on $[Zn_2(oba)_2(bpy)]$,[62] a rigid MOF with very similar chemical composition and porosity, for

which no luminescence frequency shift was observed when exposed to the same groups of analytes, it is clear that the specific structural conformation of the two flexible MOFs is crucial for the observed analyte-framework interactions. In addition, the recyclability of sample LMOF-162 was also examined. For a given analyte, LMOF-162 exhibits excellent reversible sensing ability (Figure 8).

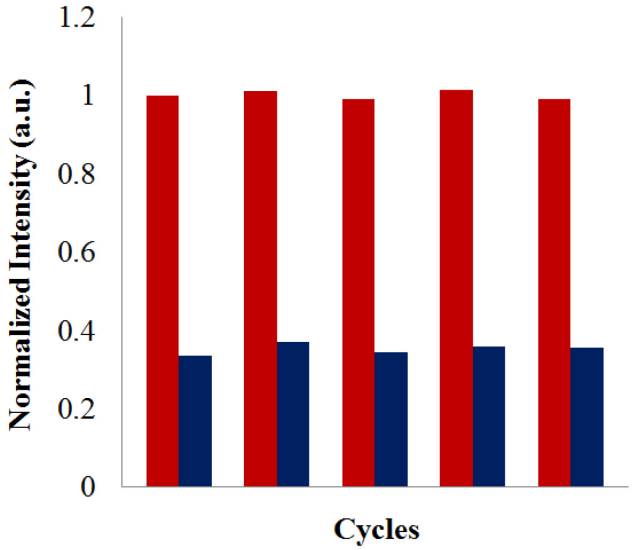

Figure 8. Recyclability test on LMOF-162. Fluorescence was recovered by applying vacuum to the sample for 3 minutes followed by DMF vapor curing for 6 minutes. Nitromethane was used as a model analyte. Analyte vapor exposure time was 5 minutes. Red bar: emission of sample before exposure. Blue bar: emission after exposure to nitromethane for 5 minutes.

In-situ infrared (IR) absorption spectroscopy measurements were carried out to characterize the interaction of selected analytes nitrobenzene, nitrotoluene (Group A) and benzene, toluene (Group B) with LMOF-162. Upon adsorption of analyte molecules into the MOF, the clear absorption features of the most prominent modes, including phenyl C-C stretching mode ν_{19} and nitro-group N-O stretching bands ν_s and ν_{as}, reveal that these guest molecules adopt a well-defined arrangement within the framework pores (Figure 9). The red shift of the ν_{19} band in adsorbed benzene and toluene (compared to the free gas molecules) suggests the weakening of phenyl bonds, which could be due to withdrawal of electron

density from the phenyl ring π orbitals as a result of their interactions with LMOF-162 as predicted in previous study of metal benzene complexes.[101,102] For nitrobenzene and nitrotoluene with a large electron affinity, the mode of interest is the nitro ($-NO_2$) stretching bands, which are expected to redshift after receiving an electron to the LUMO orbitals of neutral molecules.[103,104] The $\nu_{as}(NO_2)$ and $\nu_s(NO_2)$ modes in adsorbed nitrobenzene and nitrotoluene redshift by -24, -9 and -23 cm^{-1}, and -20 cm^{-1} from their gas phase values (Figure 9), indicating an electron-density redistribution from LMOF to adsorbed analytes. These observed shifts provide additional evidence for our proposed model that the fluorescence quenching/enhancing effects in LMOFs can be explained by the donor-acceptor electron transfer mechanism.[62] Several other factors, such as the vapor pressure and reduction potential of the analytes, also affect the fluorescent response.

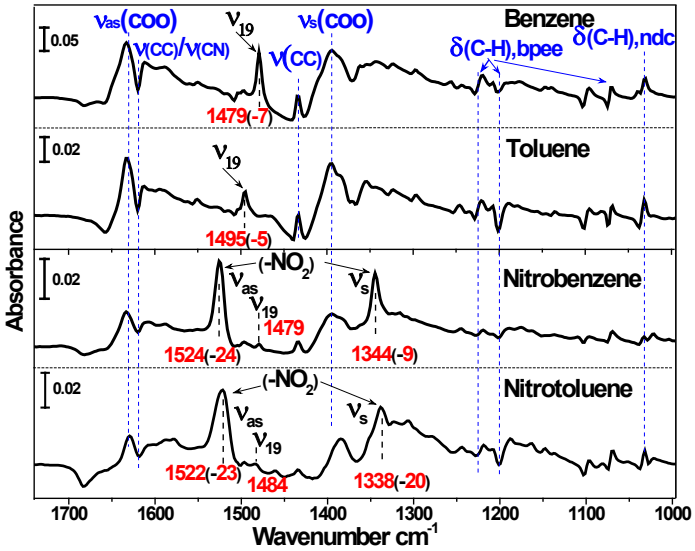

Figure 9. Difference spectra of benzene, toluene, nitrobenzene and nitrotoluene upon adsorption into LMOF-162 at RT and equilibrium vapor pressures of analytes, referenced to the blank LMOF-162. The black dashed lines correspond to the analytes bands; The blue dashed lines correspond to LMOF-162 and indicate the perturbation of absorption bands of LMOF-162. (Courtesy of Dr. Kui Tan)

To understand the nature of emission frequency shift, we also performed theoretical calculations on LMOF-162 with two selected analytes, nitrobenzene (NB, Group-A) and nitromethane (NM, Group-C). Using molecular dynamics methods, we obtained simulated structures of NB@LMOF-162 and NM@LMOF-162. An *ab initio* method (Gaussian 03) was employed to calculate the blue shifted bands observed in emission peaks.[105] Since the LUMO of the analytes are lower in energy than the CB of LMOF-162, the interaction between the analytes and LMOF-162 pushed the CB up, leading to a small increase in the band gap and thereby a blue shift in the PL emission (Figure 10). Further, the extent of such an interaction is stronger for NM@LMOF-162 than for NB@LMOF-162, and hence a larger blue shift was observed for the former than for the latter. Clearly, LMOFs with different structures have different energy levels, and the extent of their interactions with different analytes varies.[106]

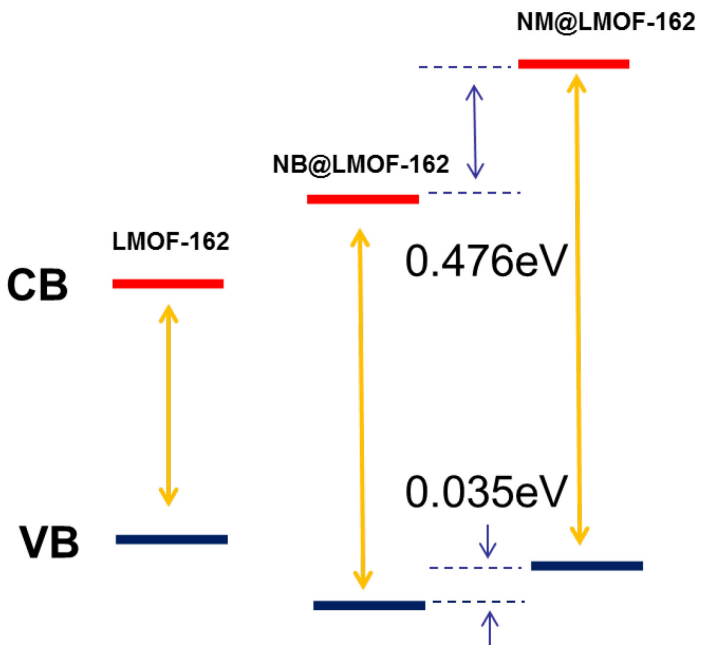

Figure 10. Schematic diagram showing the changes in the VB and CB of LMOF-162 when exposed to nitrobenzene (NB) and nitromethane (NM). (Courtesy of Dr. Chong Zheng)

We anticipate that for suitable MOF sensory materials, such 2D maps can be generated for accurate and effective recognition and identification of a large number of analytes, particularly those that show similar quenching/enhancement behavior and are generally difficult to identify otherwise.

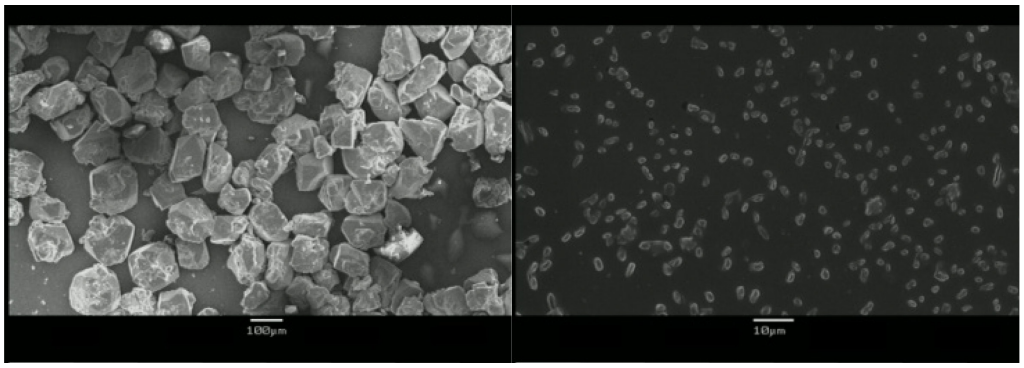

Figure 11. SEM images of LMOF-162 by solvothermal synthesis (top, scale bar 100 μm) and surfactant assisted method (bottom, scale bar 10 μm).

For practical applications, a short response time is one of the most important parameters to consider. We demonstrated in the case of RPM3-Zn that decreasing particle size can substantially shorten the response time.[94] Aiming at more rapid detection by the title compounds, we adapted a surfactant-assisted method[107] to reduce their particle size. As shown in Figure 11, bulk samples synthesized by solvothermal reactions have an average size of approximately 50-120 μm. Utilizing the hexadecyltrimethyl-ammonium bromide (CTAB) assisted synthesis, we successfully downsized the particles to around 1-5 μm. The fluorescence sensing ability of small sized particles of LMOF-162 was tested on DMNB, TNT and RDX. For a given emission frequency shift, the response time was improved by 4-5 times.

2.1.3. Conclusions

In summary, a new porous and flexible MOF structure LMOF-161 was synthesized and structurally characterized. The fluorescent properties and sensing performance of this compound and its structural analogue LMOF-162 were investigated. These compounds exhibit a unique response towards analytes of interest, including high explosives such as TNT and RDX. Strong analyte-framework interactions generate a fluorescence signal in two dimensions: emission intensity change (quenching or enhancement) and frequency shift. Utilizing both variables in signal transduction enables the construction of a 2D map on which specific analytes can be unambiguously identified. Overall, the strategy described here would be of great assistance in developing high-performance MOF based sensors.

2.2. The Indirect Detection of a Non-volatile Explosive

2.2.1. Introduction

The detection of energetic materials has attracted much attention over the past decade.[59,61,67,89] RDX as a common explosive in terrorist activities, is of great current interest due to the enormous difficulty in its detection.[108] First, the vapor pressure of RDX is extremely low (6 ppt or 4.6×10^{-9} torr).[87,109] This issue is compounded by the presence of binders and other components, which reduces the weight percent of the explosive molecule and further decreases the vapor pressure. Furthermore, it is estimated that the vapor pressure of the explosive molecule can be reduced by a factor of 1000 in the presence of wrapping or packing materials.[109] Finally, the unfavorable reduction potential and the absence of an aromatic ring in RDX further diminish its capability to interact with a sensory material, making its effective detection extremely challenging.[61,88,110] A feasible alternative to identifying the explosives is to detect volatile species in their headspace, such as plasticizers, stabilizers, solvents and degradation products, which may make easier targets.[88,111-113]

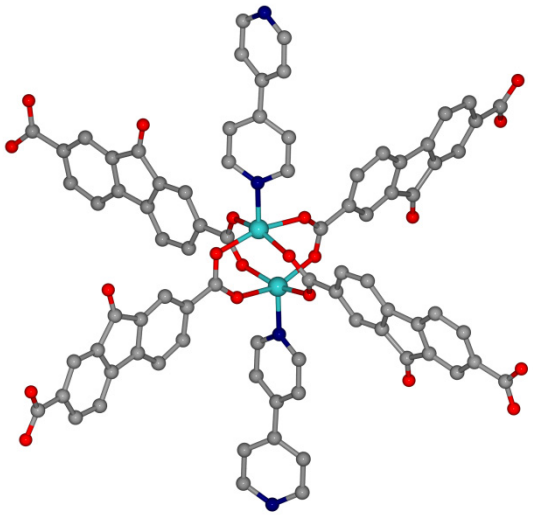

(a)

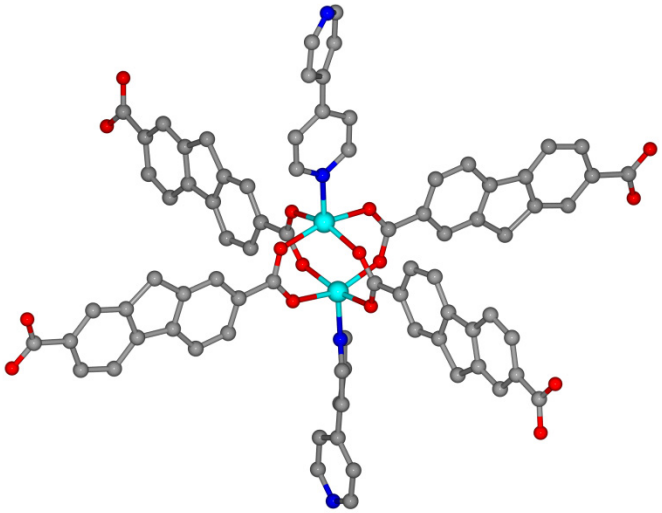

(b)

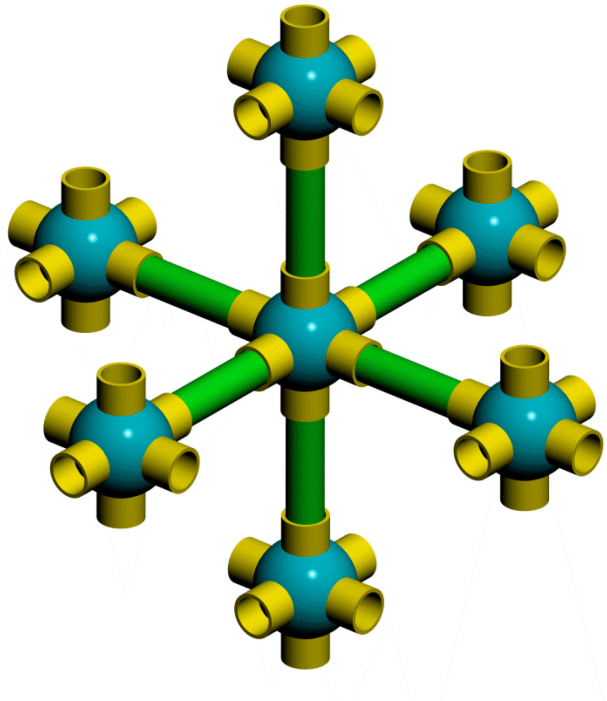

(c)

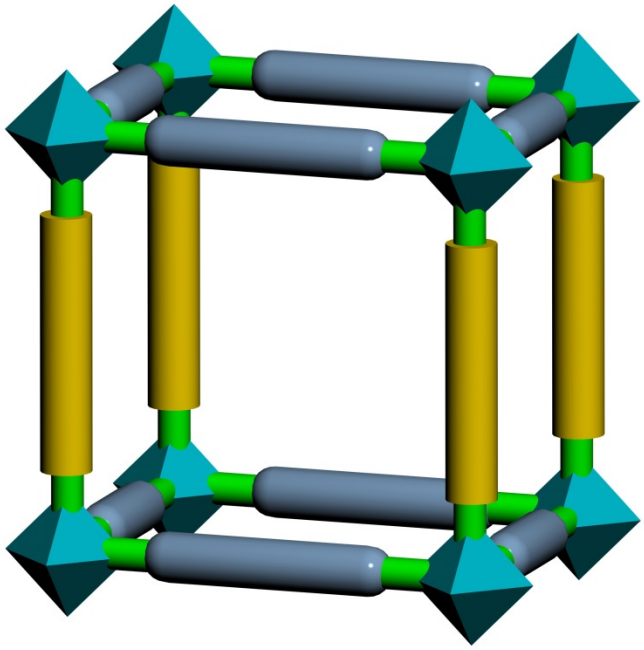

(d)

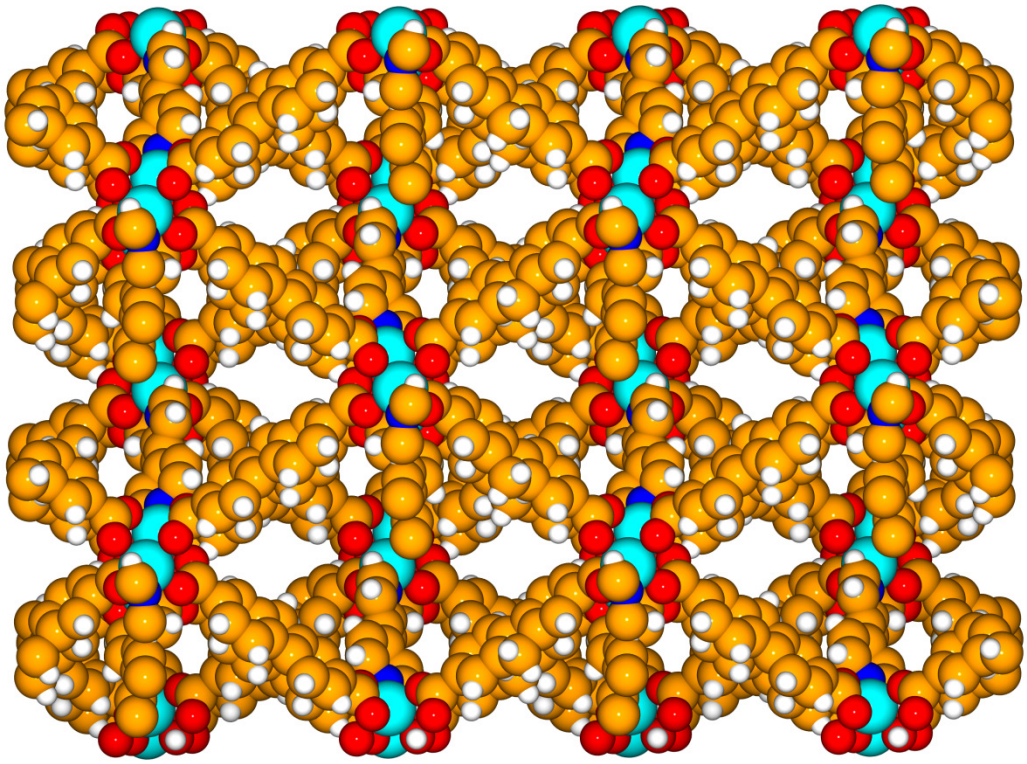

(e)

Figure 12. SBU of (a) LMOF-201 and (b) LMOF-202; (c) Illustrations of the connectivity of ligands (green) to the Zn core (aqua) and (d) a single cage of the framework; (e) The overall 3D structure of LMOF-202 viewing along the a axis. Colour code: White (H), Orange (C), Blue (N), Red (O), Aqua (Zn).

LMOFs made their debut as explosives sensors very recently.[62,94,95] In comparison to conjugate polymers, LMOFs are unique in the following aspects: high crystallinity, intrinsic porosity, and systematically tunable pore surface.[6,21-24,114-116] Engineering these factors can significantly enhance the selectivity and sensitivity of a LMOF material towards a specific target. The first study on explosive detection utilizing a LMOF material, LMOF-111 (or RPM3-Zn, $Zn_2(bpdc)_2(bpee)$), showed that it is capable of very fast, sensitive, and reversible detection of DMNB and DNT in the vapor phase.[94,95] Following this work, a more systematic investigation on LMOF-121 or $Zn_2(oba)_2(bpy)$ uncovered the excited state

electron transfer mechanism for LMOF based sensors.[62] More recently this subject has been expanded to a number of different LMOFs, for the detection of small molecules[74,117] and ionic species,[55,118,119] as well as explosive species.[66,70-72,85,120-124] In the cases of explosive sensing, the detection has always been directly of the explosives and/or explosive-like molecules. Herein, we strategically target a solvent (cyclohexanone) that is used in the recrystallization of RDX and inevitably co-exists in the explosive product, as a way of indirect yet faster and easier detection.

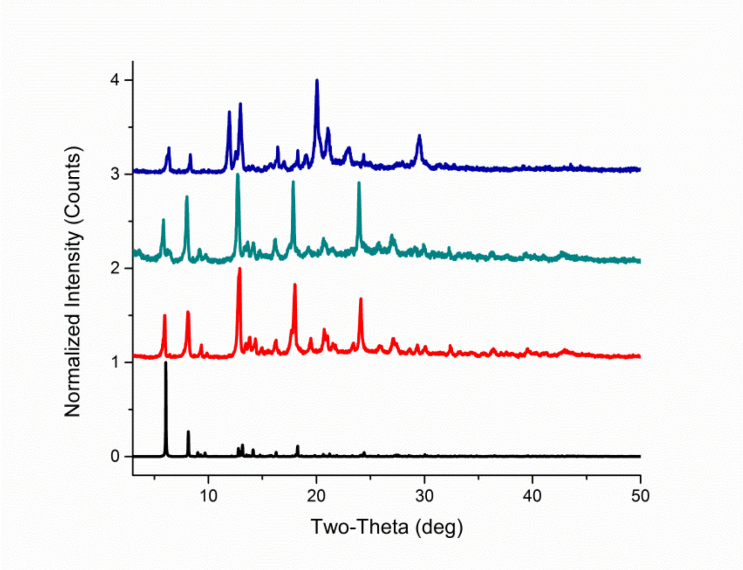

Figure 13. PXRD patterns of outgassed sample LMOF-201' (blue), diethyl ether washed sample (cyan), and as-made sample LMOF-201 (red) compared with the simulated pattern from the single crystal data (black).

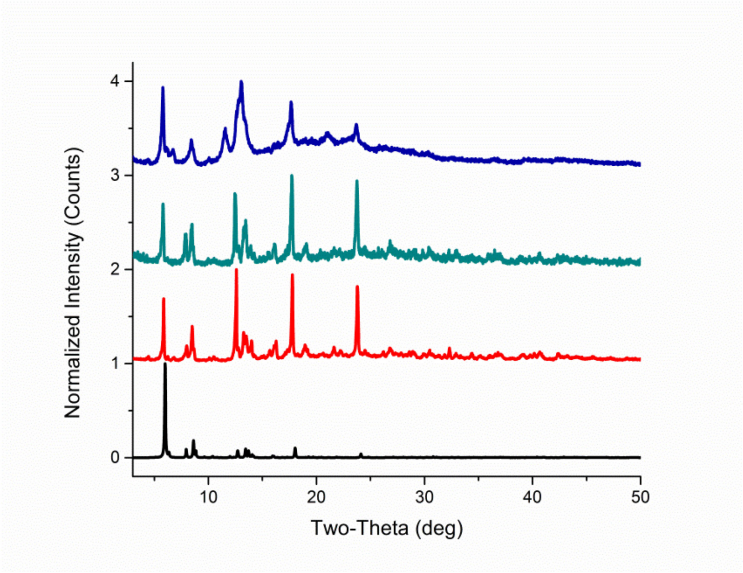

Figure 14. PXRD patterns of outgassed sample LMOF-202' (blue), dichloromethane washed sample (cyan), and as-made sample LMOF-202 (red) compared with the simulated pattern from the single crystal data (black).

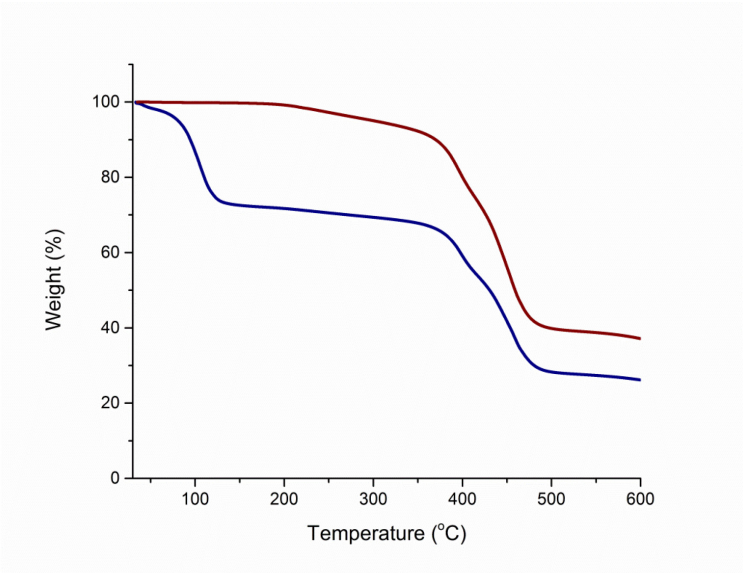

Figure 15. Thermogravimetric profile of LMOF-201 (blue) and LMOF-201' (burgundy) under nitrogen flow.

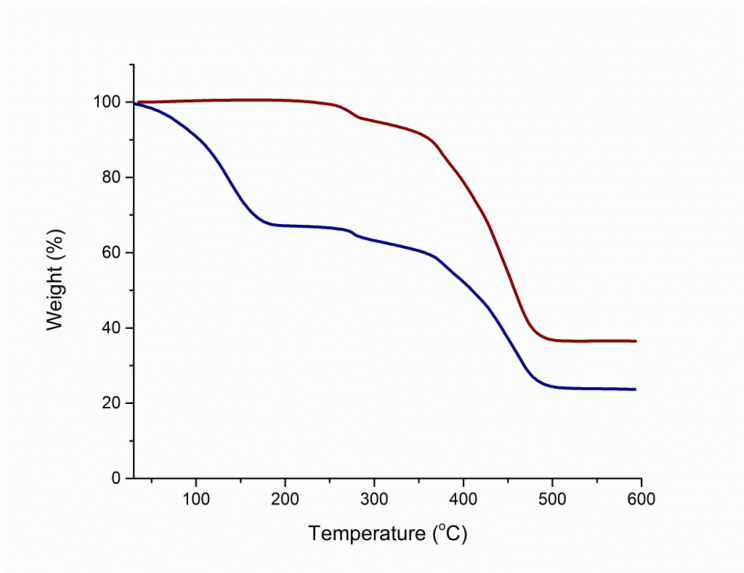

Figure 16. Thermogravimetric profile of LMOF-202 (blue) and LMOF-202' (burgundy) under nitrogen flow.

2.2.2. Results and discussion

LMOF-201 ($Zn_2(ofdc)_2(bpy)\cdot 2.5DMF\cdot 1.25H2O$, ofdc = 9-oxo-9H-fluorene-2,7-dicarboxylate) and LMOF-202 ($Zn_2(hfdc)_2(bpy)\cdot xDMA$, hfdc = 9H-fluorene-2,7-dicarboxylate, DMA = N,N'-dimethylacetamide) were synthesized using solvothermal method. Single crystal X-ray diffraction revealed both structures are three-dimensional (3D) frameworks built on $Zn_2(Rfdc)_4$ (R = O or H) paddle-wheel secondary building unit (SBU), as shown in Figure 12 (

Table 2 and Table 3). Each SBU is connected to four identical units to form a two-dimensional (2D) 4^4 net. The adjacent 2D layers are further bridged by bpy ligands giving rise to a 6 coordinated uninodal net with the Point symbol of $\{4^{12}\cdot 6^3\}$ and Vertex symbol of $[4.4.4.4.4.4.4.4.4.4.4.4.6_4.6_4.6_4]$. Two of such 3D networks interpenetrate to yield the overall structure. The compounds can be activated at 120 °C under vacuum overnight (LMOF-201' and LMOF-202'). Although constructed from similar ligands, the two compounds differ

drastically in porosity: While both compounds experience certain degree of structure change upon activation, LMOF-201' is nearly nonporous in comparison to LMOF-202' as a result of a larger substitution group on the carboxylate. The BET surface areas are 24 m^2/g and 136 m^2/g, respectively.

Table 2. Single crystal data for LMOF-201

Compound	$[Zn_2(ofdc)_2(bpy)]\cdot 2.5DMF\cdot 1.25H_2O$ (LMOF-201)
Formula	$C_{47.5}H_{40}N_{4.5}O_{13.75}Zn_2$
M	1024.58
Crystal system	Monoclinic
Space group	P 2(1)/c
a/Å	13.8166(7)
b/Å	21.7847(12)
c/Å	20.1414(11)
α/°	90.00
β/°	103.312(1)
γ/°	90.00
V, $Å^3$	5899.5(5)
Z	4
Temperature (K)	100(2)
λ (Mo Kα) Å	0.71073
D, g/cm^3	1.154
Reflections collected	59805
R1[a] [I > 2σ(*I*)]	0.0822
wR2[b] [I > 2σ(*I*)]	0.2006
Goodness-of-fit	1.017
CCDC number	979464

[a] $R1 = \sum \lceil F_o - F_c \rceil / \sum \lceil F_o \rceil$
[b] $wR2 = \sum[w(F_o^2 - F_c^2)^2] / w(F_o^2)^2]^{1/2}$

Table 3. Single crystal data for LMOF-202 based on the SQUEEZE model

Compound	$[Zn_2(hfdc)_2(bpy)]\cdot x$DMA (LMOF-202)
Formula	$C_{40}H_{24}N_2O_8Zn_2$
M	791.39
Crystal system	Monoclinic
Space group	C 2/c
a/Å	33.559(7)
b/Å	22.171(4)
c/Å	19.706(4)
α/°	90.00
β/°	124.022(3)
γ/°	90.00

V, Å^3	12152(4)
Z	8
Temperature (K)	295(2)
λ (Mo Kα) Å	0.71073
D, g/cm^3	0.865
Reflections collected	50481
R1^a [I > 2σ(*I*)]	0.0436
wR2^b [I > 2σ(*I*)]	0.1239
Goodness-of-fit	1.002
CCDC number	979466

^{a}R1= $\sum \left| F_o - F_c \right| / \sum \left| F_o \right|$
^{b}wR2= $\sum[w(F_o^2 - F_c^2)^2] / w(F_o^2)^2]^{1/2}$

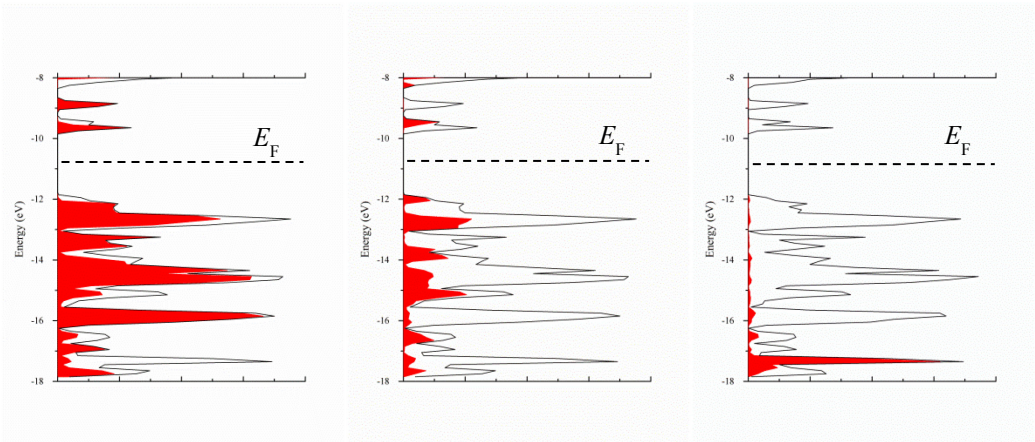

Figure 17. Calculated density of states (*DOS*) for LMOF-202 using Extended Hückel method. The solid curve denotes the total *DOS*. The shaded arearefers to the contribution from hfdc (left), bpy (middle), and Zn (right) respectively. The dashed horizontal line denotes the Fermi level. (Courtesy of Dr. Chong Zheng)

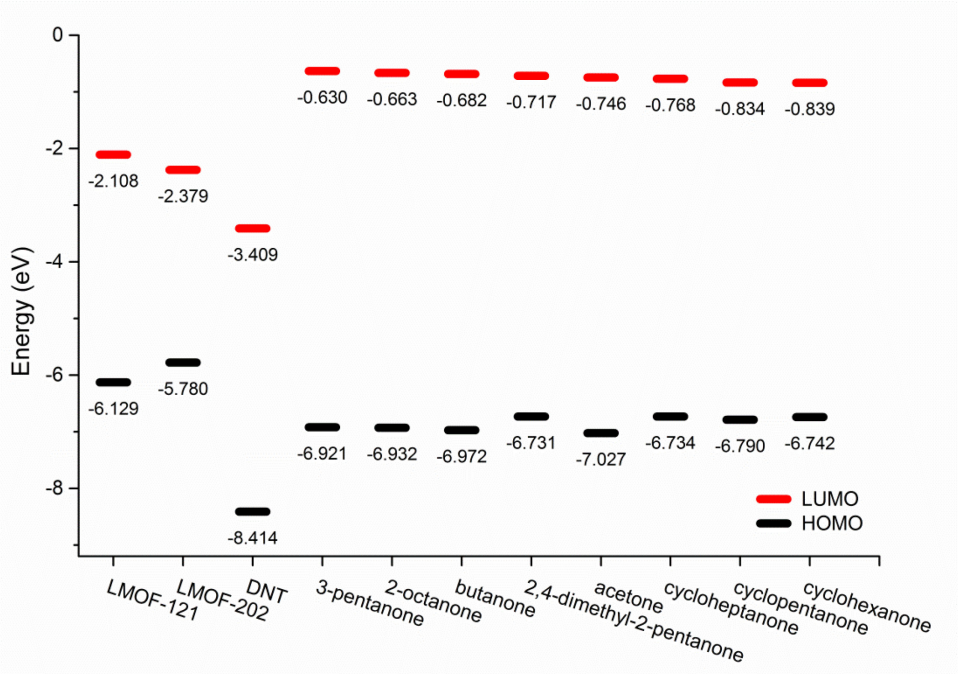

Figure 18. An illustration of molecular orbital energy levels of LMOF-121, LMOF-202, and analytes computed at B3LYP/SDD (on Zn), 6-31+G*(on H, C, N, O).

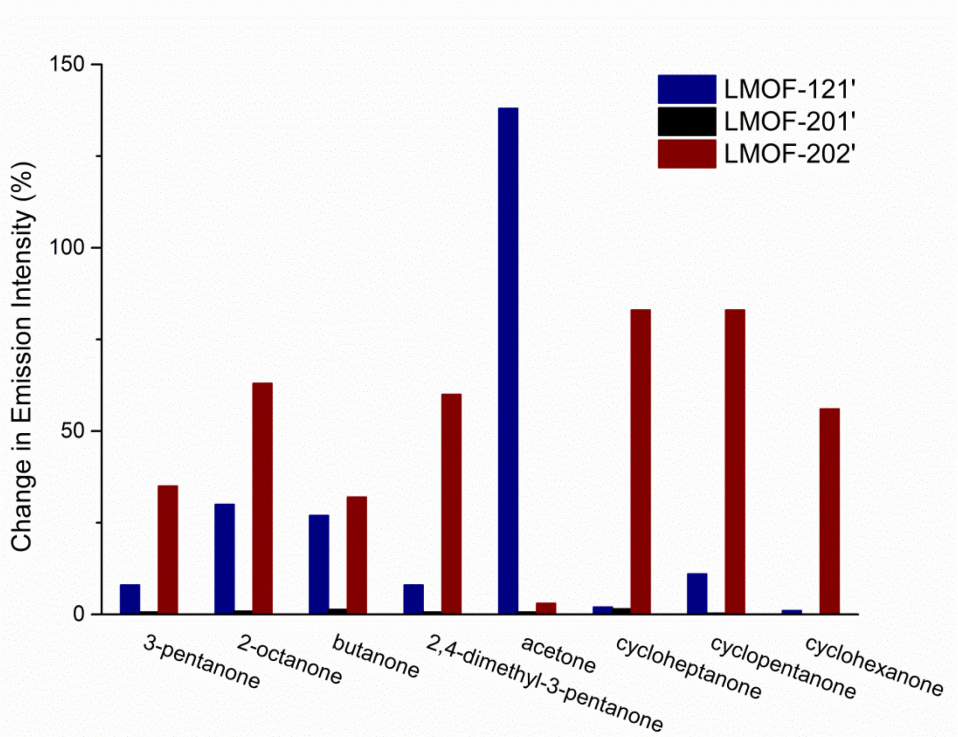

Figure 19. A comparison of fluorescence enhancement after 10 s exposure of LMOF-121' and LMOF-202' to the vapors of ketones.

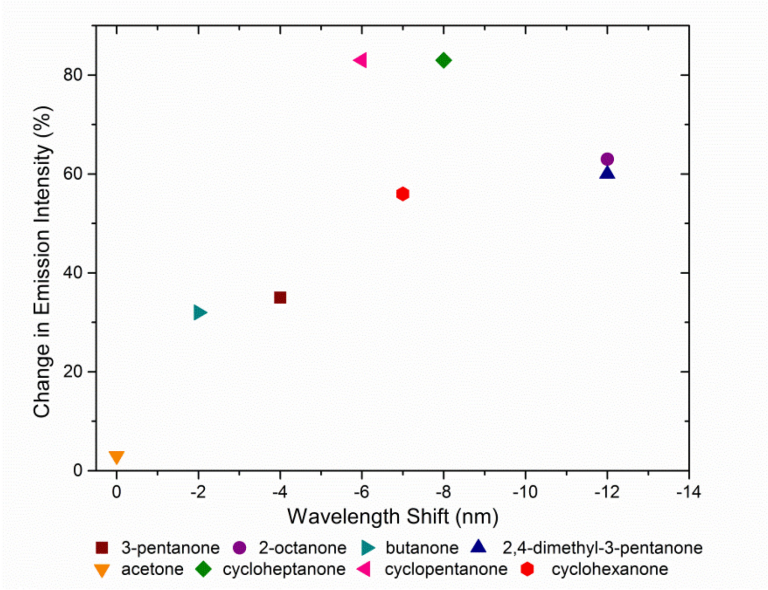

Figure 20. A 2D colour coded map of ketones based on the fluorescence response of LMOF-202'.

The PL response towards ketone vapors was evaluated on activated solid samples. Both compounds display band-gap emission in the blue/green region primarily due to LLCT. Density of states (DOS) calculations on LMOF-202 revealed that the maximum of valance band (VB) consists mostly of bpy while the minimum of conduction band (CB) is largely made of the hfdc (Figure 17).[125,126] A series of chain and cyclic ketones were included in this study. Ketones have high-lying lowest unoccupied molecular orbitals (LUMOs) which are far above the conduction bands of LMOFs (Figure 18).[127] Upon excitation, they act as strong electron donors and therefore enhance the fluorescent emission of LMOFs.[62] The experimental observation of the interaction between LMOF-202' and the saturated vapor of ketones supports this prediction: the fluorescence intensity of LMOF-202' was enhanced significantly after only 10 seconds of exposure (with the exception of acetone, Figure 19). Note that upon exposure to ketone vapors, the emission maximum of LMOF-202' shifted to higher energy, a strong evidence of exciplex formation.[21] Taking emission peak wavelength

and intensity changes into account, each ketone can be pin-pointed on a 2D map as shown in Figure 20. To further testify that detecting cyclohexanone is a feasible method to indirectly identify RDX, a LMOF-202' was exposed to a RDX sample recrystallized in cyclohexanone and its PL signals monitored over a time period. A considerable enhancement in it emission intensity was observed (more than 12% within 15 minutes). A control experiment on an excessively dried (in vacuum oven for 72 hours) RDX gave no PL response (Figure 21 and Figure 22). Therefore the residue cyclohexanone is a proven easier target than RDX itself. Besides being able to rapidly identify ketones, another merit of LMOF-202' is its resistance to interferences from other molecules: common solvents and representative aromatics barely affect its emission (Figure 23).

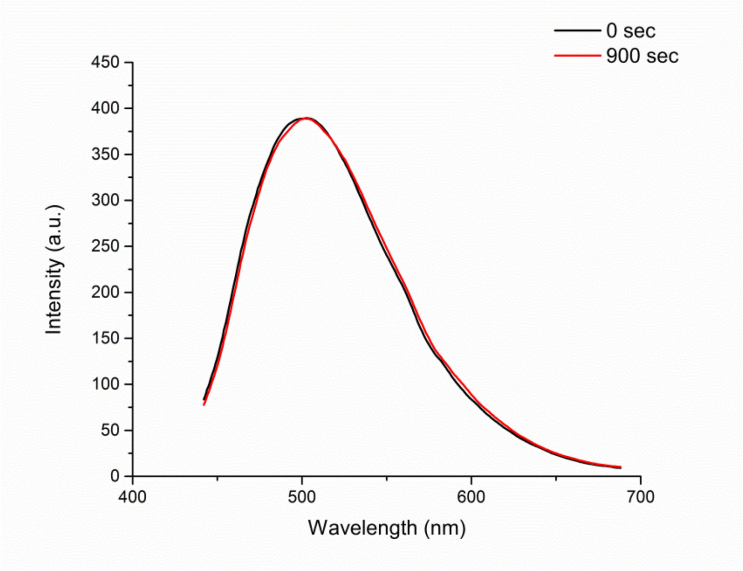

Figure 21. PL emission spectra of LMOF-202' (black) and the same sample after 900 s exposure to dry RDX (red) at room temperature.

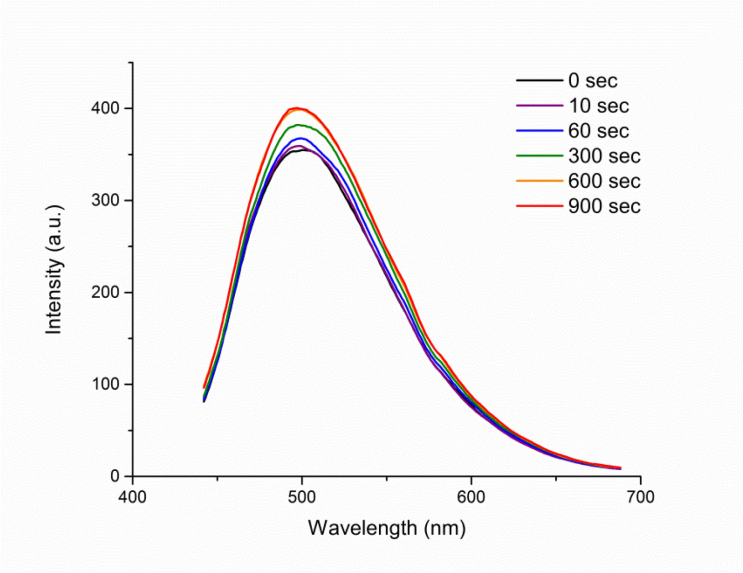

Figure 22. PL emission spectra of LMOF-202' (black) and the same sample after gradual exposure to a RDX sample freshly recrystallized in cyclohexanone at room temperature.

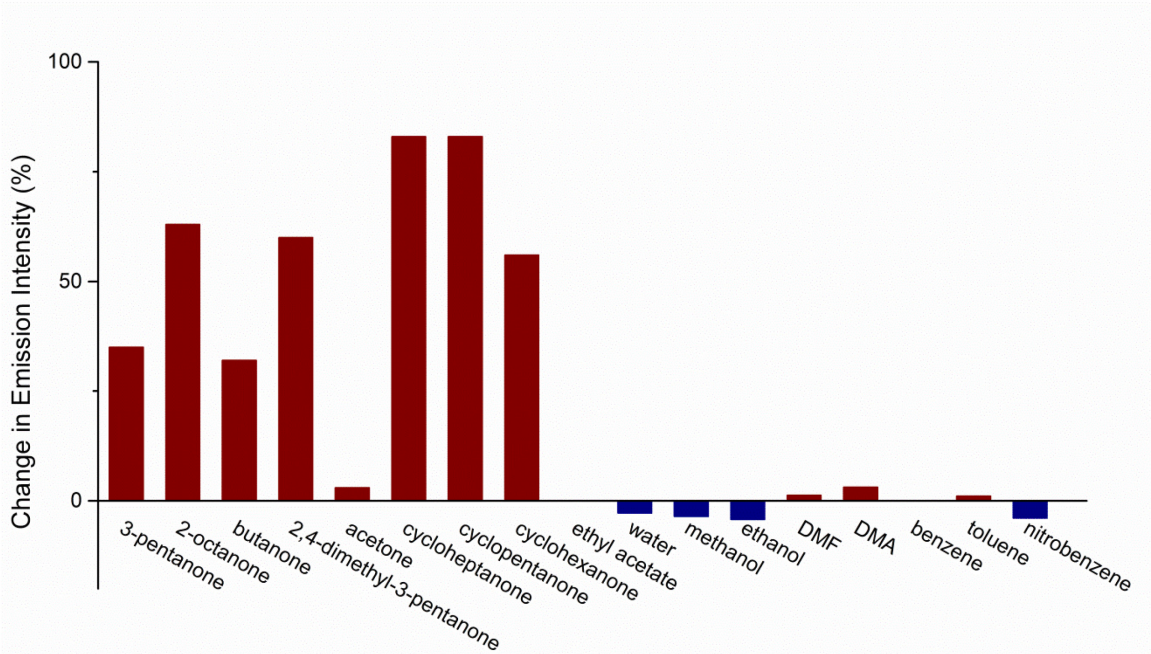

Figure 23. A summary of the emission intensity change of LMOF-202' after exposure to analytes for 10 s at room temperature.

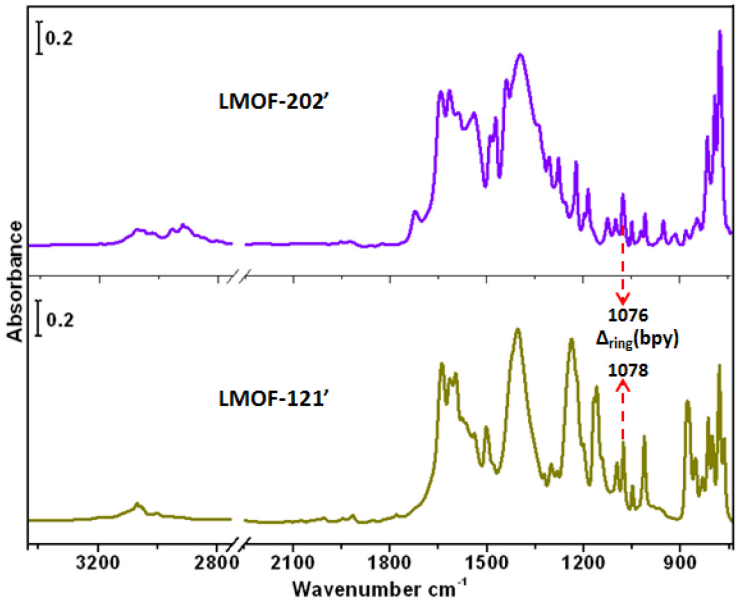

Figure 24. IR absorption spectra of activated (top) LMOF-202' and (bottom) LMOF-121' reference to KBr pellet under N_2 purge. (Courtesy of Dr. Kui Tan)

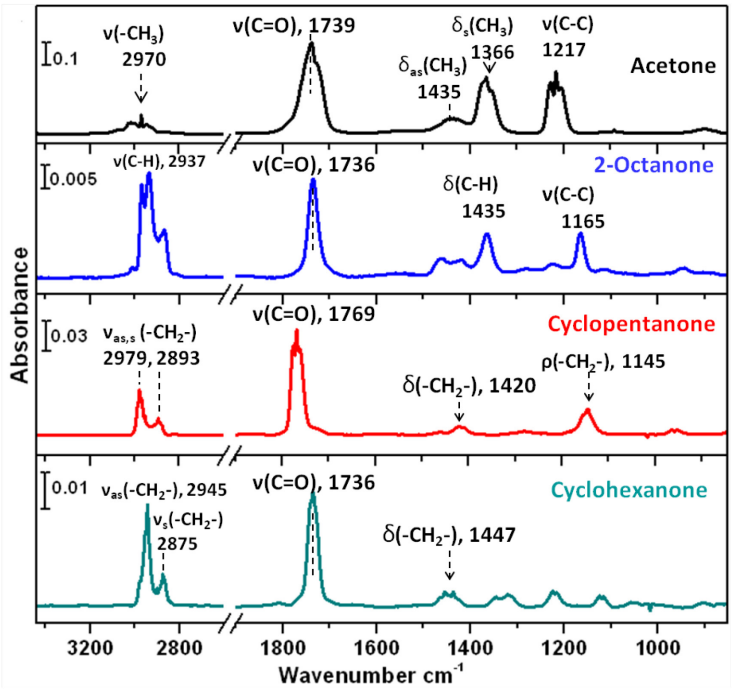

Figure 25. IR absorption spectra of vapor phase analytes from top to bottom: acetone, 2-octanone, cyclpentanone, cyclohexanone. (Courtesy of Dr. Kui Tan)

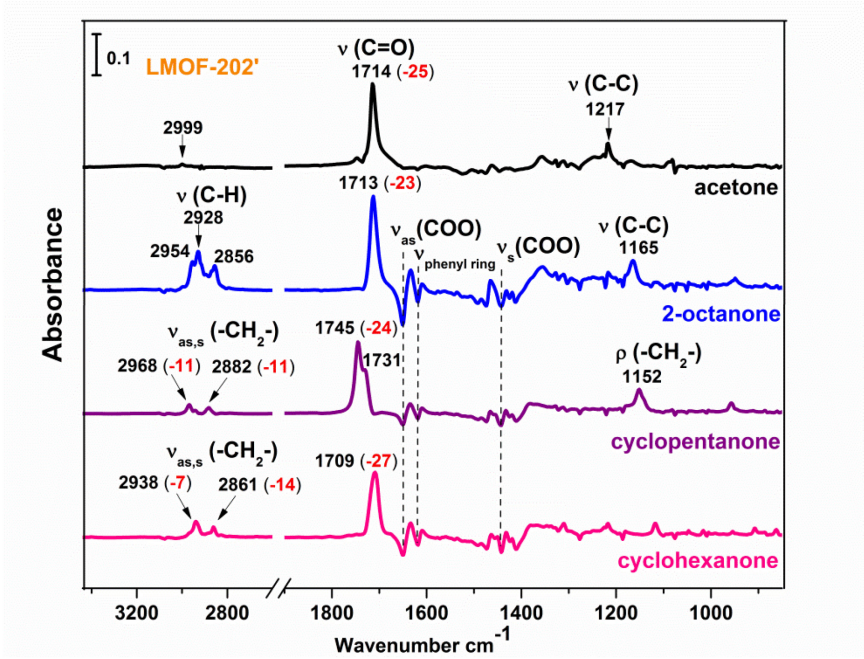

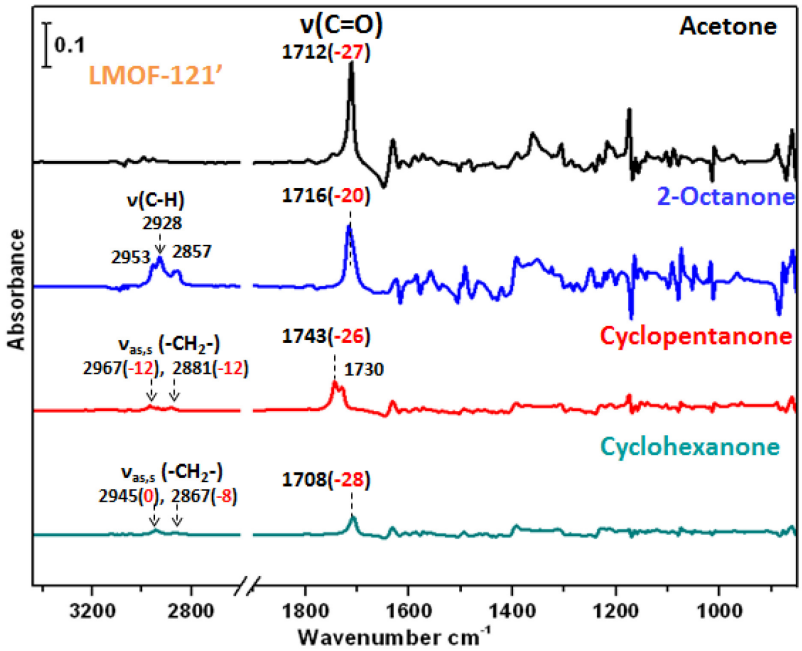

Figure 26. IR absorption spectra of adsorbed ketone molecules: acetone, 2-octanone, cyclopentanone, cylcohexanone in LMOF-202' (top) and LMOF-121' (bottom) referenced to IR spectrum of blank LMOF samples respectively. The spectra were recorded after exposing LMOF samples to vapors for 3 min. (Courtesy of Dr. Kui Tan)

Table 4. Relative intensities of ν(C=O) bands for the ketone molecules adsorbed in LMOF-202' and LMOF-121'.

ν(C=O)	$I_{\nu(C=O)}/ I_{\delta ring}$	
	LMOF-202'	LMOF-121'
Acetone	1.098	1.000
2-Octanone	1.238	0.7013
Cyclopentanone	1.330	0.4137
Cyclohexanone	1.043	0.2133

All bands are normalized to in-plane 4,4'-bipy ring deformation mode δ_{ring} at 1076 for LMOF-202' and 1078 cm^{-1} for LMOF-121'. (Courtesy of Dr. Kui Tan)

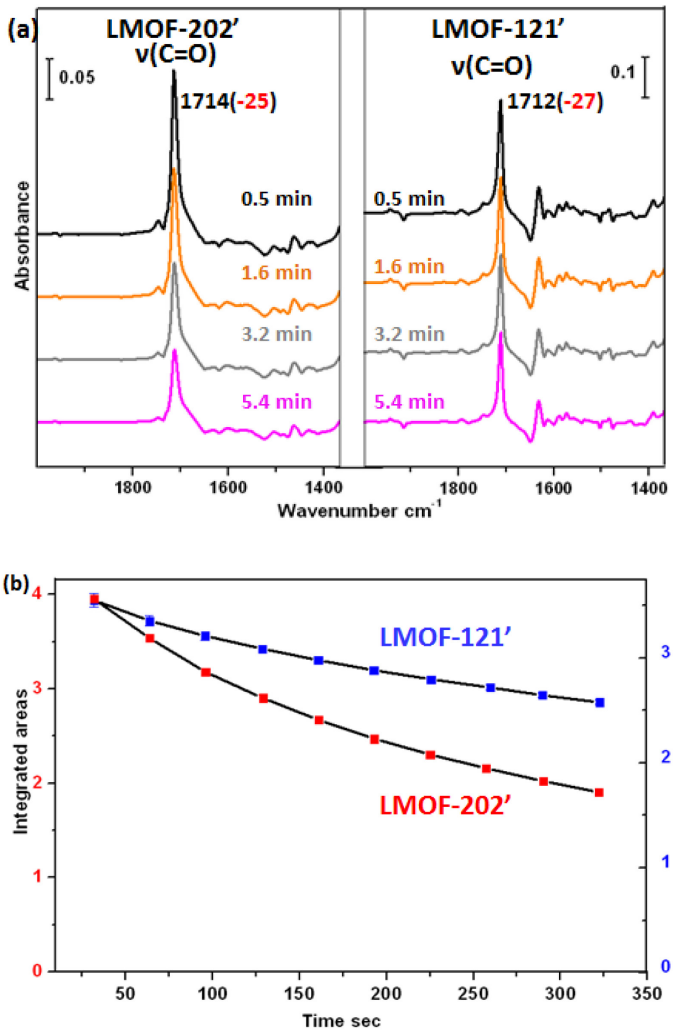

Figure 27. (a) IR spectra of adsorbed acetone in LMOF-202' (left) and LMOF-121' (right) under N_2 purge as a function of time. (b) Integrated areas of ν(C=O) band of adsorbed acetone decrease as a function of time. Blue, LMOF-121'; red, LMOF-202'. (Courtesy of Dr. Kui Tan)

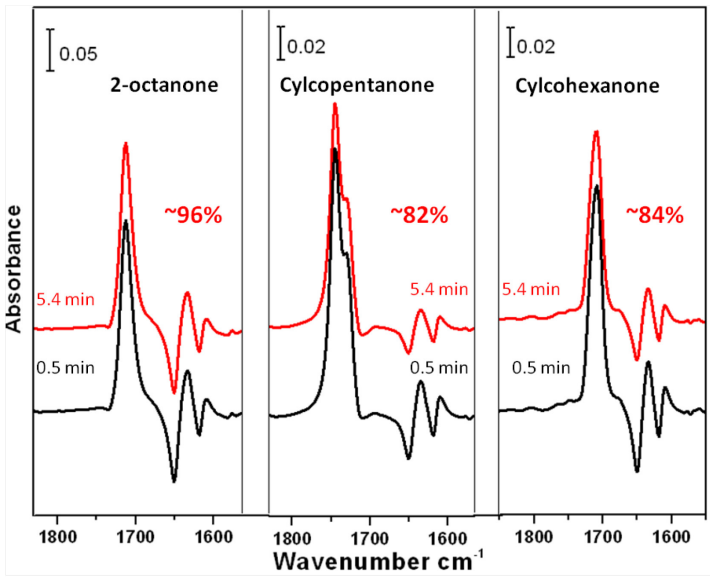

Figure 28. Time-dependent IR spectra of adsorbed 2-octanone, cyclopentanone and cyclohexanone in LMOF-202' under N_2 purge. Blue, data recorded within 0.5 min; red, after 5.4 min. (Courtesy of Dr. Kui Tan)

In-situ infrared spectroscopy indicates that ketone vapors are captured by LMOF-202', with the appearance of several new features specifically associated with ketones such as the ν(C=O), $\nu_{as,s}(CH_2)$ and ν(C-C) bands. These bands are red shifted from their positions in the free ketones by ~20 to ~30 cm^{-1} upon adsorption into LMOFs (Figure 25 and Figure 26). The adsorption of larger ketone molecules such as 2-octanone, cyclopentanone, and cyclohexanone significantly perturbs the skeleton vibrational modes of LMOF-202', as seen in red shifts of the stretching modes of the carboxylate group $\nu_{as,s}(COO^-)$ and of the phenyl ring ν_{phenyl}, as shown in Figure 5 (for reference, the IR spectra of original LMOFs are shown in Figure 24). In contrast, the perturbations induced by the inclusion of acetone into LMOF-202' are much weaker, suggesting a weaker interaction with this framework. This is consistent with the observation that acetone diffuses out of LMOF-202' much faster than other longer chain and cyclic ketones (Figure 27 and Figure 28). Therefore, the notably low response in fluorescence intensity of LMOF-202' to acetone vapor is attributed to the

weaker interaction (i.e. affinity) of this small sized molecule with the framework. (IR data was collected by Dr. Kui Tan.)

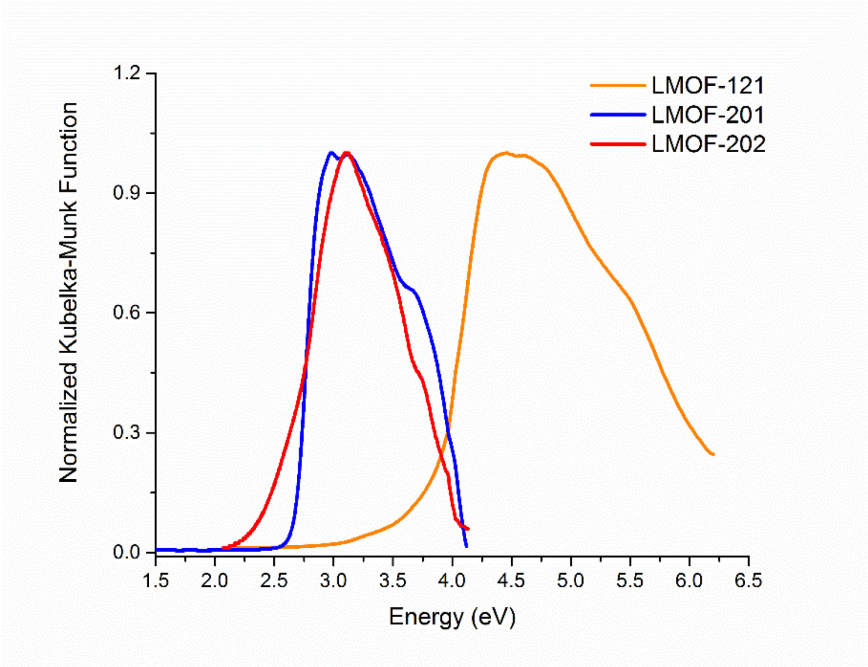

Figure 29. Optical adsorption spectra of solid samples of LMOF-121, LMOF-201, and LMOF-202.

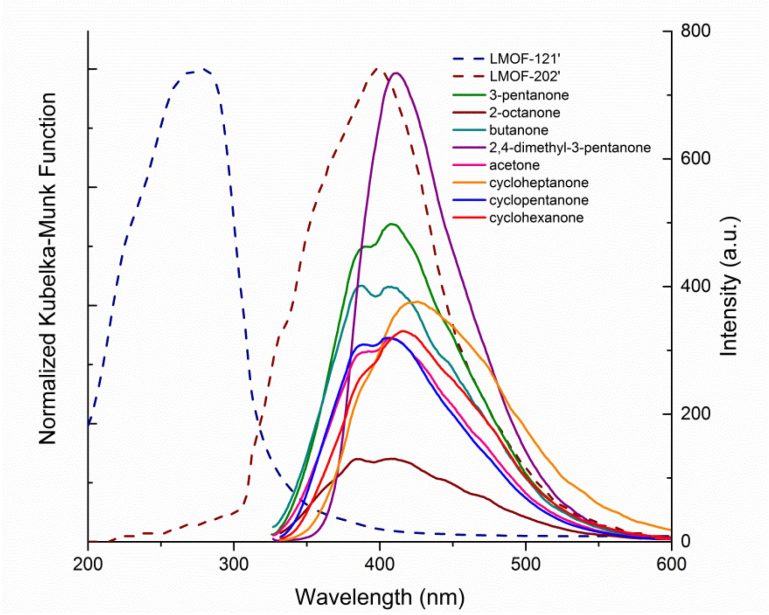

(a)

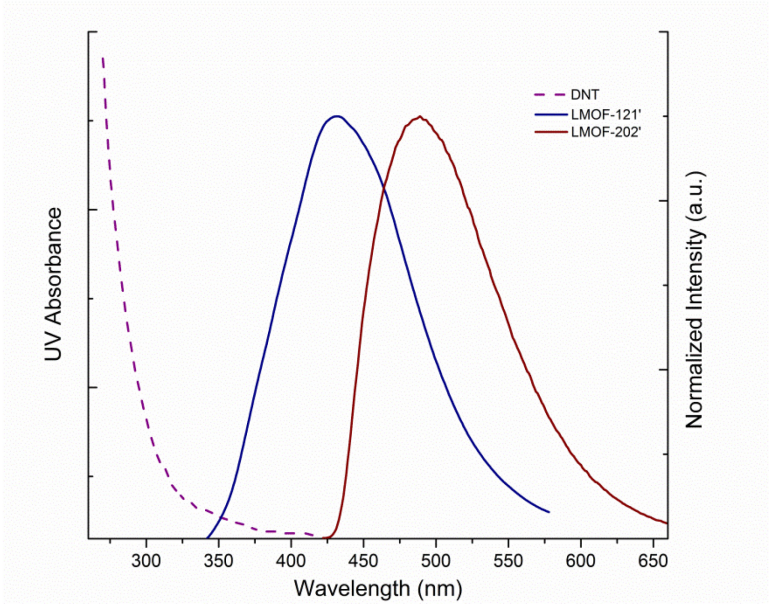

(b)

Figure 30. (a) Emission spectra of ketones (solid lines) at λ_{ex} = 300 nm and UV absorbance of LMOF-121' (dashed blue) and LMOF-202' (dashed burgundy). (b) UV absorbance of DNT (dashed blue) and emission spectra of LMOF-121' (solid blue, λ_{ex} = 280 nm) and LMOF-202' (solid burgundy, λ_{ex} = 300 nm).

Although LMOF-201' and LMOF-202' have very similar band gaps (Figure 29), their responses to ketone vapors are distinctly different. LMOF-201' is quite inert to ketones, as its fluorescence intensity was barely affected upon exposure to ketone vapors. In this case, porosity differentiates the two: The intrinsic pores within the LMOF-202' facilitate the diffusion and accumulation of analytes, and the confined analytes interact more readily with the sensory material, resulting in enhanced response. This does not apply to LMOF-201' as it is nearly nonporous.

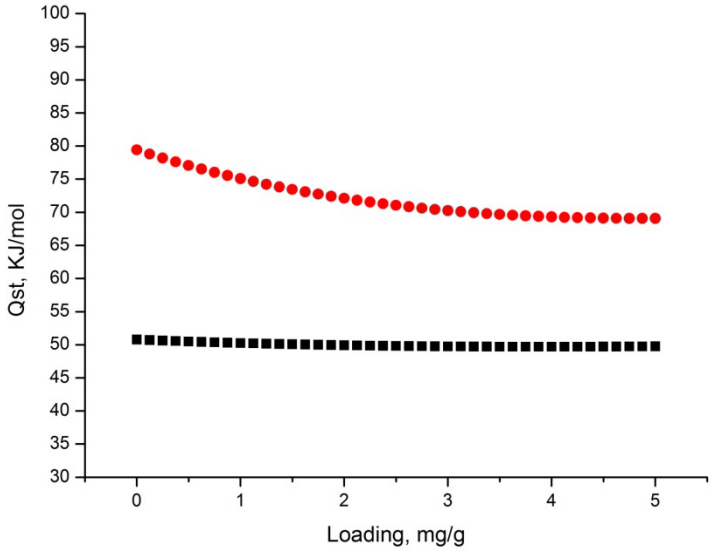

Figure 31. Heat of adsorption of acetone in LMOF-121 (red) and LMOF-202 (black).

The role of electron transfer (short-range) process in the change of fluorescence of a LMOF under excitation has been well examined in numerous studies concerning chemical sensing and explosive detection. Yet energy transfer, a long range process vital to the mediation of the fluorescence response, has only been scarcely explored. In the case of LMOF-202' large spectral overlaps were found between its absorption spectrum and the emission spectra of ketones. A large portion of emitted photons from ketones are re-adsorbed by LMOF-202' which contributes significantly to the enhancement of its emission. To address the impact of energy transfer, LMOF-121 was selected for comparison. The porosity (surface area) of LMOF-121' is similar to that of LMOF-202',but the absorption spectra of the two are very different: LMOF-121' has a notably higher band gap (~ 4.0 eV, Figure 29) and absorbs in a higher energy region (Figure 4a) than LMOF-202' (band gap: ~ 2.5 eV). With the same exposure time (10 seconds), the fluorescence enhancement of LMOF-121' is generally much less than that of LMOF-202' (Figure 19, with a clear exception of acetone). This observation can be partially attributed to the very small spectral

overlap between the absorption spectrum of LMOF-121' and the emission spectra of ketones, limiting the emission enhancement due to the energy transfer effect. On the other hand, large spectral overlaps are attained between the absorption spectrum of LMOF-202' and the emission spectra of ketones, contributing substantially to the enhancement of PL emission. The exception in the case of acetone may be explained by both IR and adsorption studies. The high compatibility between the pore size of LMOF-121' and the molecular size of acetone leads to a particularly strong guest-host interaction, and consequently acetone molecules are adsorbed and held much more strongly in LMOF-121' than in LMOF-202' (Figure 27). This is confirmed by the heat of adsorption (Qst) values calculated from acetone adsorption isotherms, which are ~70-80 kJ/mol for LMOF-121' and only ~50-51 kJ/mol for LMOF-202' (Figure 31). The adsorption/interaction of larger ketones in LMOF-121' is much limited compared to LMOF-202' due to its small pore size (Figure 26 and Table 4), and thereby much lower PL responses (Figure 19).

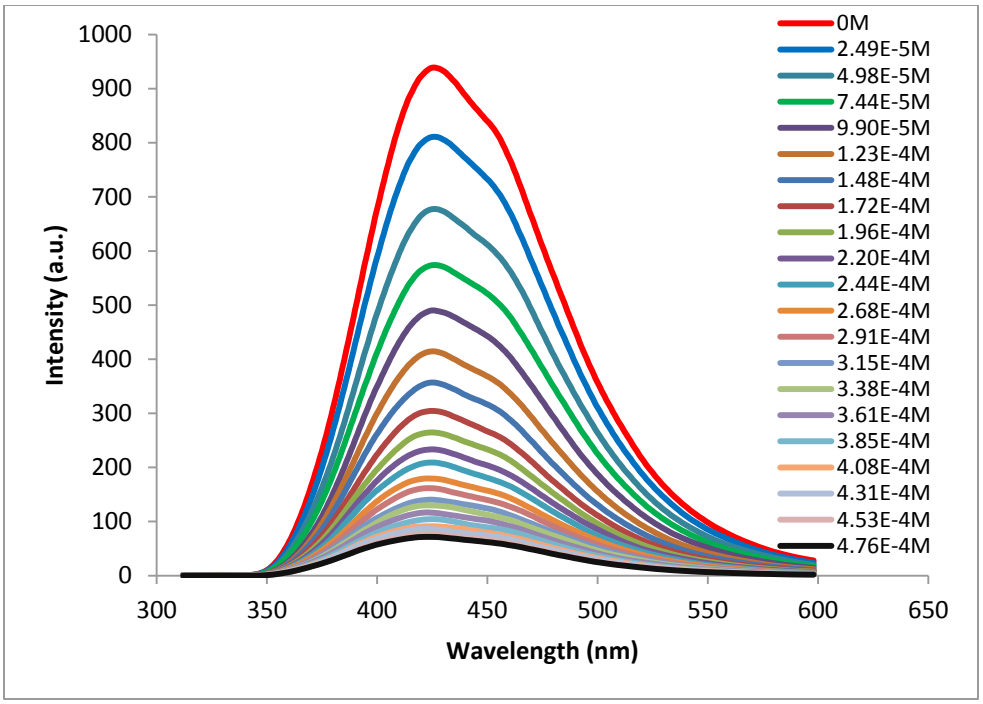

(a)

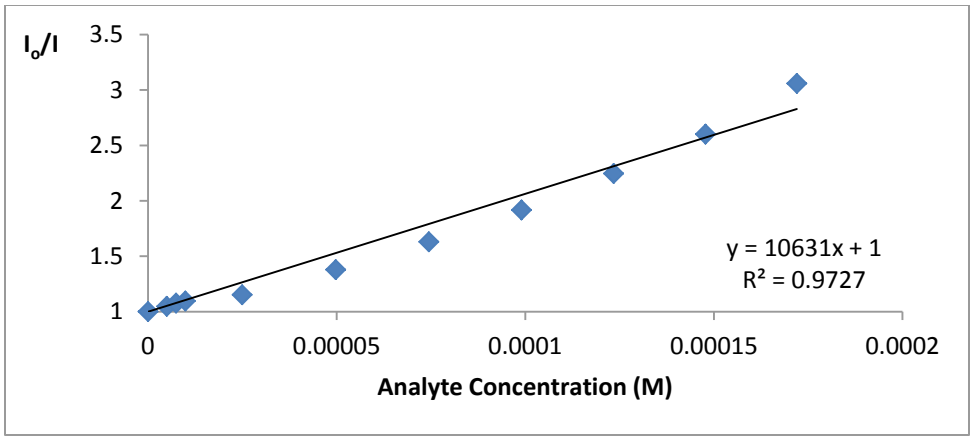
I_o/I
3.5
3
2.5
2
1.5
1
0
0.00005
0.0001
0.00015
0.0002
Analyte Concentration (M)
y = 10631x + 1
R² = 0.9727

(b)

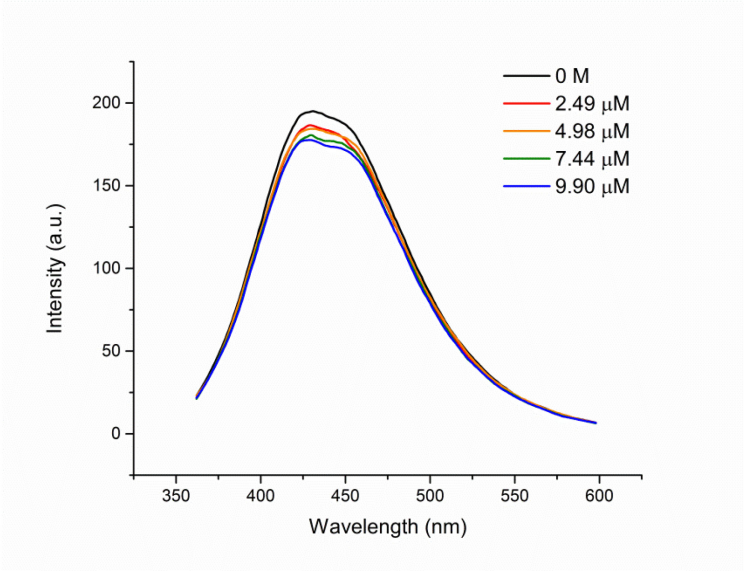
0 M
2.49 μM
4.98 μM
7.44 μM
9.90 μM
Intensity (a.u.)
200
150
100
50
0
350
400
450
500
550
600
Wavelength (nm)

(c)

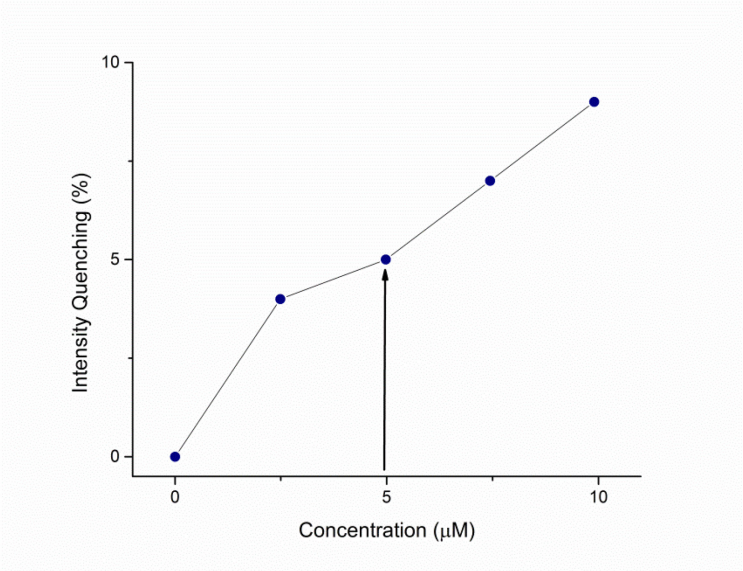

(d)

Figure 32. (a) Quenching of the fluorescence of LMOF-121 upon the incremental addition of DNT (10 μL, 0.01 M aliquot). (b) Stern-Volmer plot of LMOF-121 showing the quenching efficiency of DNT. (c) Quenching of the fluorescence of LMOF-121 upon the incremental addition of lower concentration DNT (10 μL, 0.001 M aliquot). (d) Detection limit determined from (c): DNT = 4.98 μM or 0.91 μg/mL, from this point on, a steeper slope is observed.

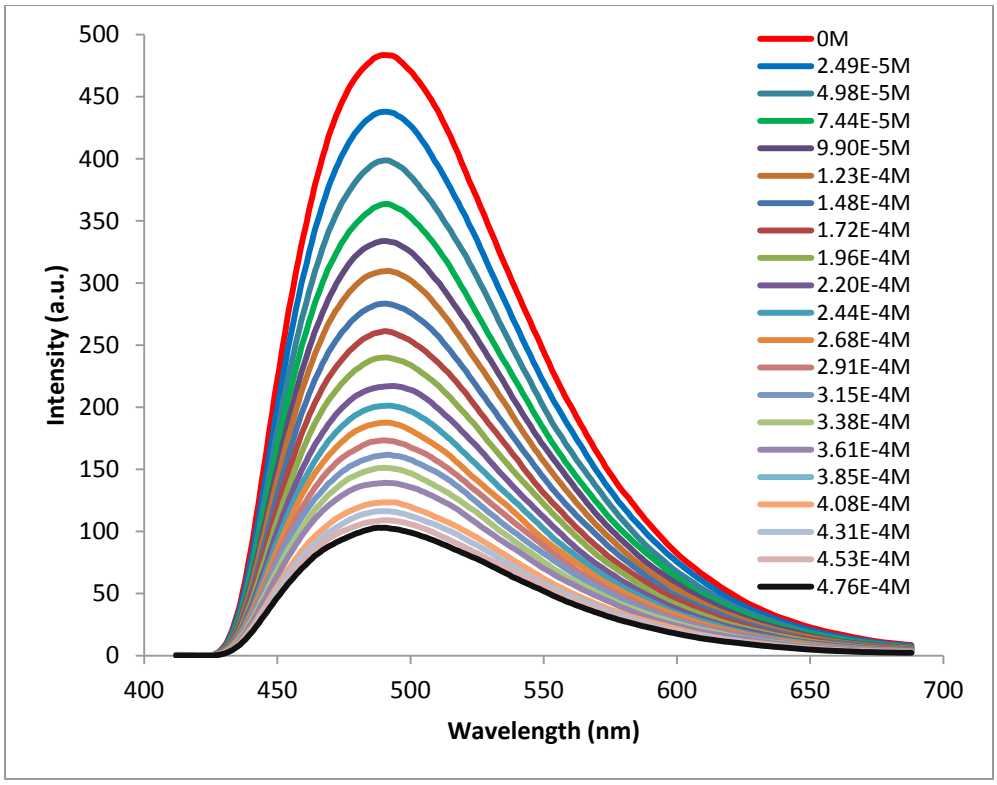

(a)

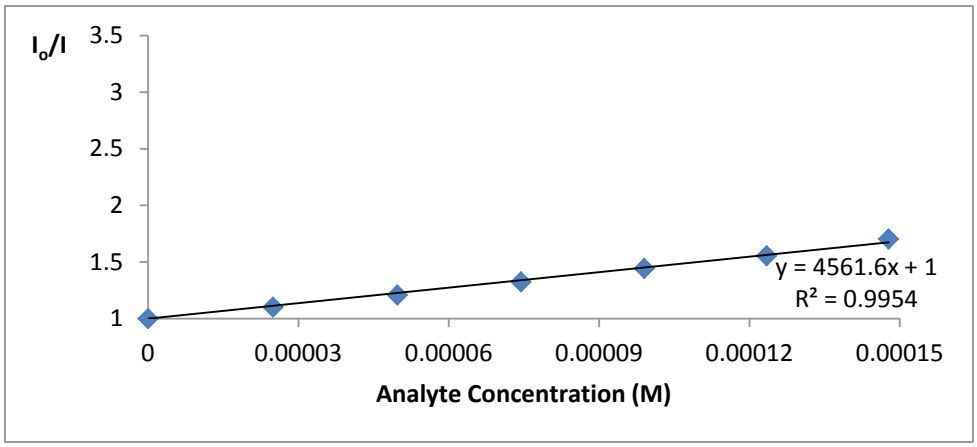

(b)

Figure 33. (a) Quenching of the fluorescence of LMOF-202 upon the incremental addition of DNT (10 μL, 0.01 M aliquot). (b) Stern-Volmer plot of LMOF-202 showing the quenching efficiency of DNT.

The energy transfer mechanism is more recognized in fluorescence quenching where the emission spectrum of sensory material overlaps with the absorption spectrum of

analyte.[64,66,128] To compare the effect of energy transfer on the fluorescence quench response of LMOF-202 and LMOF-121, fluorescence titrations of DNT (2,4-dinitrotulene) were performed on 0.4 mg/mL suspensions of LMOF in DMF respectively (Figure 32 and Figure 33). The Stern-Volmer (SV) equation, $I_0/I = K_{sv}\cdot[Q] + 1$, was employed to evaluate the quenching efficiency of two LMOFs, where I_0 is the initial fluorescence intensity without the quencher, I is the fluorescence intensity with the addition of the quencher, [Q] is the molar concentration of the quencher, and Ksv is the quenching constant. For LMOF-121 a K_{sv} of 1.1×10^4 M^{-1} was obtained, which is comparable to the best performance of reported polymer sensors.[129] Using LMOF-121, the detection limited for DNT is estimated to be 4.98 μM or 0.91 μg/mL (Figure 32). For LMOF-202, a smaller K_{sv} value is obtained, 4.6×10^3 M^{-1} (Figure 33). This difference is due to both electron and energy transfer effects: Electronically, LMOF-121 has a higher CB than that of LMOF-202, thus favoring electron transfer to DNT at excited state (Figure 18). Considering energy transfer, LMOF-121 is more sensitive towards DNT because its emission spectrum overlaps much more strongly with the absorption spectrum of DNT than that of LMOF-202. Such spectral overlap is essentially nonexistent for the latter (Figure 30b) and the quenching effect relies solely on electron transfer.

2.2.3. Conclusions

In summary, two new and closely related members of the LMOF family, LMOF-201 and LMOF-202, were synthesized and structurally characterized. Engineering one of the ligand with different functional groups has led to distinct porosity of the two compounds, which drastically affects their sensing performances. The effective detection of high explosive RDX with extremely low vapor pressure is achieved by an indirect route via fast and highly sensitive sensing of a ketone vapor that inevitably co-exists in the explosive product. The IR

spectroscopic and guest sorption studies show that LMOF-121 interacts more strongly with acetone than with cyclic ketones as a result of size compatibility. On the other hand, LMOF-202 adsorbs other ketones more strongly than LMOF-121. The effects of electron and energy transfer processes on both fluorescence enhancement (by ketones) and quenching (by DNT) have been elucidated for LMOF-202, by comparing to LMOF-121 with similar porosity but different electronic structure. Tuning the porosity and electronic properties specifically towards a detection target can significantly improve sensitivity and selectivity. Such strategy can be very helpful in designing highly efficient sensory materials.

2.3. The Detection of Mycotoxins

2.3.1. Introduction

Mycotoxins are secondary metabolites produced by certain fungi that infect and proliferate on diverse food commodities. Mycotoxins contaminate 25% of the global food crops each year, leading to the loss of 1 billion metric tons of food products annually.[130] In the U.S. alone, the economic damage caused by mycotoxins approaches $1.5 billion per year.[131] Many of these naturally occurring toxins are teratogenic, mutagenic, and carcinogenic which pose significant adverse health effects on human beings and animals.[132]

Aflatoxins (AFs) mainly produced by *Apergillus flavus* and *Apergillus parasiticus* are one of the most dominant mycotoxins worldwide.[133] AFs contaminate a wide variety of important agricultural commodities including corn and tree nuts.[134] There are four major AFs: B_1, B_2, G_1, and G_2; AFB_1 is one of the strongest known natural carcinogens. AF-poisoning leads to the development of live cirrhosis or liver cancer (hepatoceluar carcinoma).[135] Ochratoxin A (OTA) produced by *Aspergillus ochraceus* and *Penicillium verrucosum*, is another common mycotoxin which is hepatotoxic and nephrotoxic.[133]

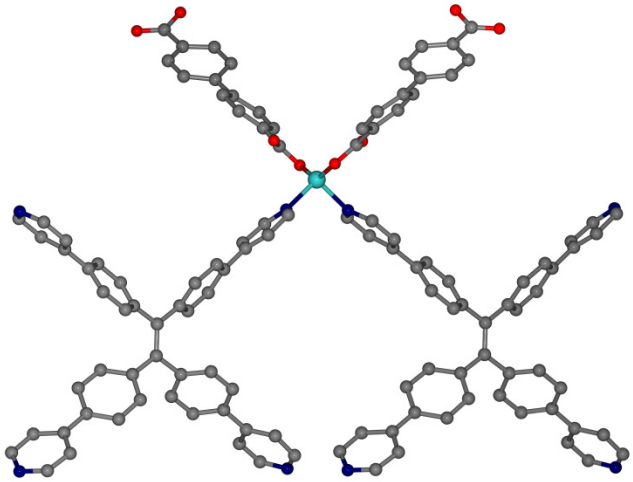

(a)

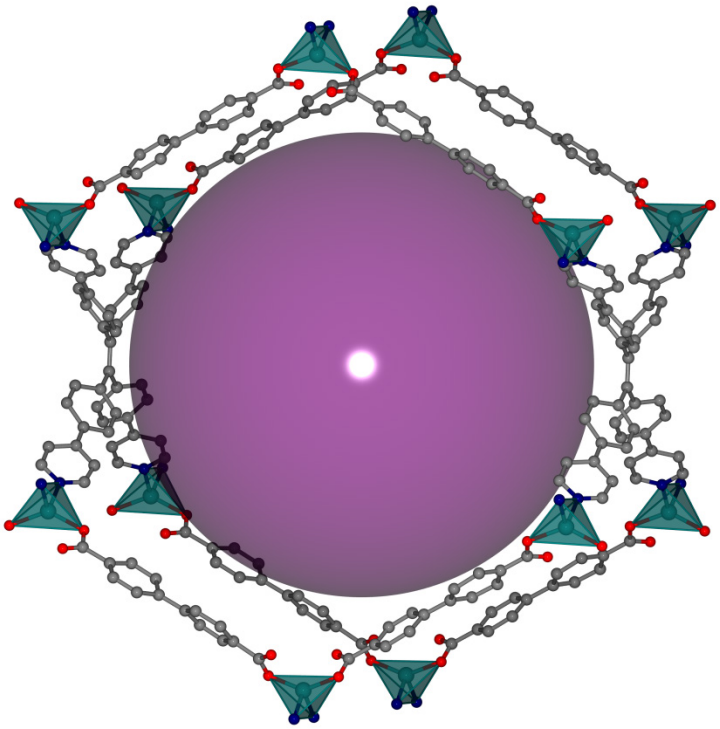

(b)

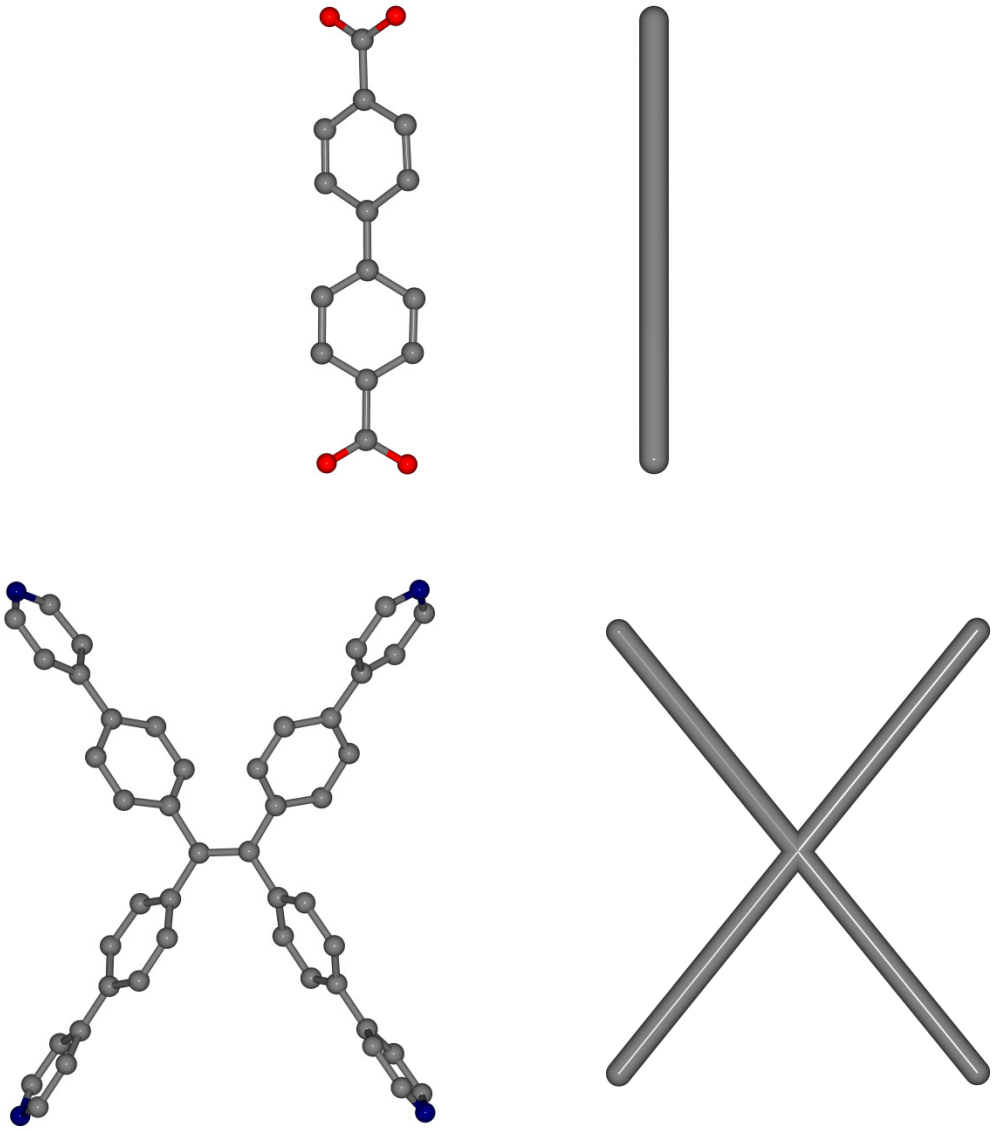

(c)

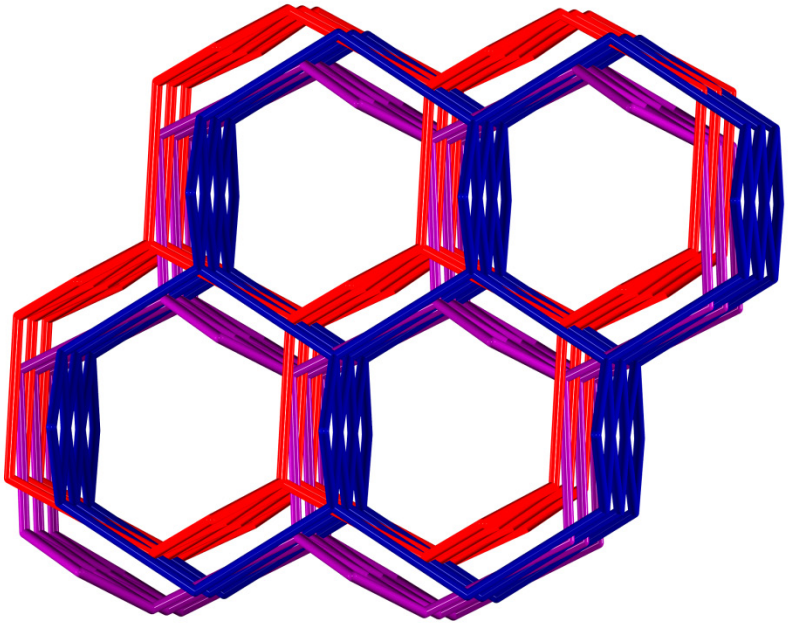

(d)

Figure 34. (a) The primary building unit showcasing a tetrahedrally coordinated Zn center. (b) A segment cut along the c axis featuring a hexagonal cage. (c) Ligand simplification: bpdc as a 2-c node and tppe as a 4-c node. (d) Simplified framework with 3-fold interpenetration and distorted hexagonal channels along the c axis. (C: grey, N: blue, O: red, and Zn: aqua; H is omitted for clarity.)

The chemical stability of most mycotoxins enables their survival through various food manufacture processes such as baking and cooking at elevated temperatures, which make the prevention of their entrance into the food chain extremely difficult.[136] Therefore, monitoring mycotoxins in human foods and animal feeds is crucial to ensure food safety. For example, the U.S. Food and Drug Administration (FDA) establishes AFs tolerant level for corn and peanut feeds intended for finishing beet cattle as 300 ppb.[137] Current mycotoxin

detection methods focus on the use of antibodies, aptamers, immunoassays, and modern instruments (such as chromatograph and mass spectroscopy), which are proven effective. However they share some common drawbacks, such as high cost and complex sample preparation, which makes them less available to developing countries, places most prone to mycotoxin contaminations.[136] Therefore the development for convenient cost-effective mycotoxin detection method has significant impact on global food safety.

Table 5. Single crystal data of LMOF-241 based on the SQUEEZE model

Compound	LMOF-241
Formula	$C_{111}H_{72}N_6O_{12}Zn_3$
M	1877.85
Crystal system	Monoclinic
Space group	C 2
a/Å	44.091(2)
b/Å	25.4060(14)
c/Å	17.1248(9)
α/°	90
β/°	91.176(4)
γ/°	90
V/Å^3	19178.7(17)
Z	4
Temperature/K	260(2)
λ (radiation wavelength)/Å	0.7749
D (g/cm^3)	0.650
Reflections collected	83865
R1[a] [I > 2σ(*I*)]	0.0598
wR2[b] [I > 2σ(*I*)]	0.1463
Goodness-of-fit	0.983
CCDC No.	1006120

[a] $R1 = \sum | F_o - F_c | / \sum | F_o |$
[b] $wR2 = \sum[w(F_o^2 - F_c^2)^2] / w(F_o^2)^2]^{1/2}$

Optical sensing utilizing the change in fluorescence readout induced by sensor-analyte interactions is a powerful detection method.[138] The choice of sensor material is the core to achieve effective detection of targeted analyte.[139] LMOFs are well explored for chemical sensing as their tunable porosity and easy-to-functionalize surface are feasible

platforms to promote strong guest-host interactions.[116,124] Here we demonstrate for the first time the use of a new LMOF for mycotoxin detection.

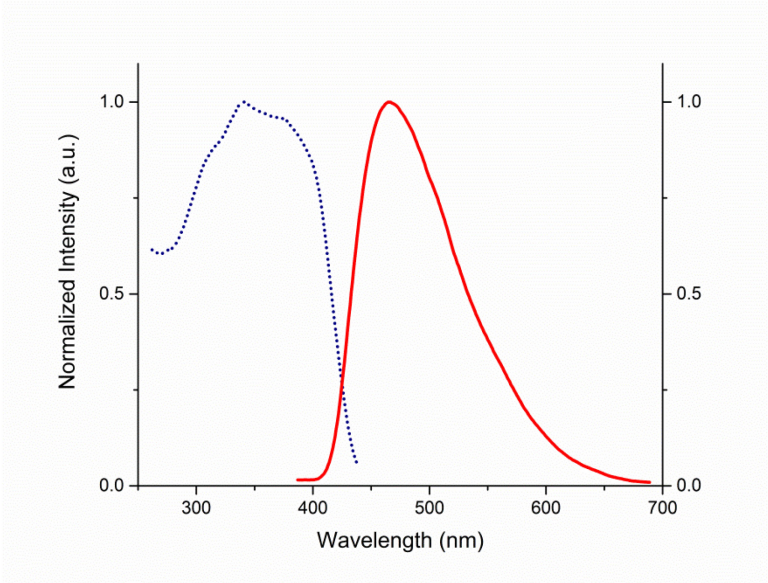

(a)

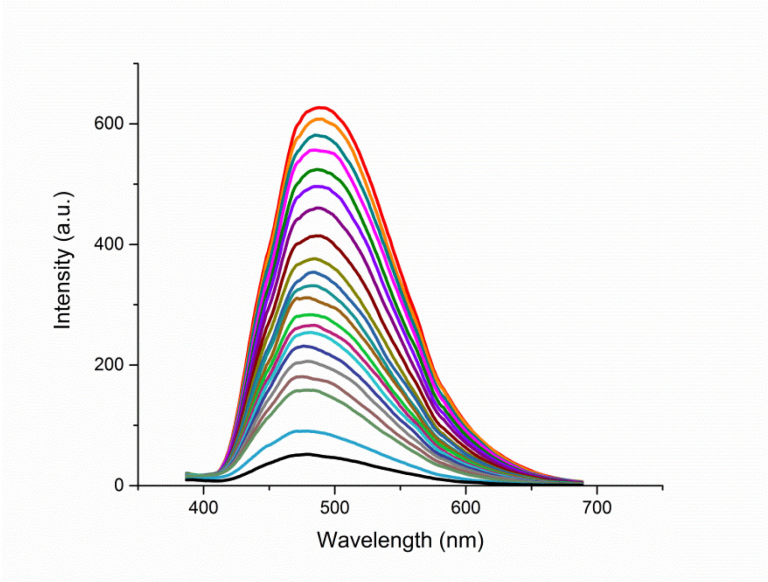

(b)

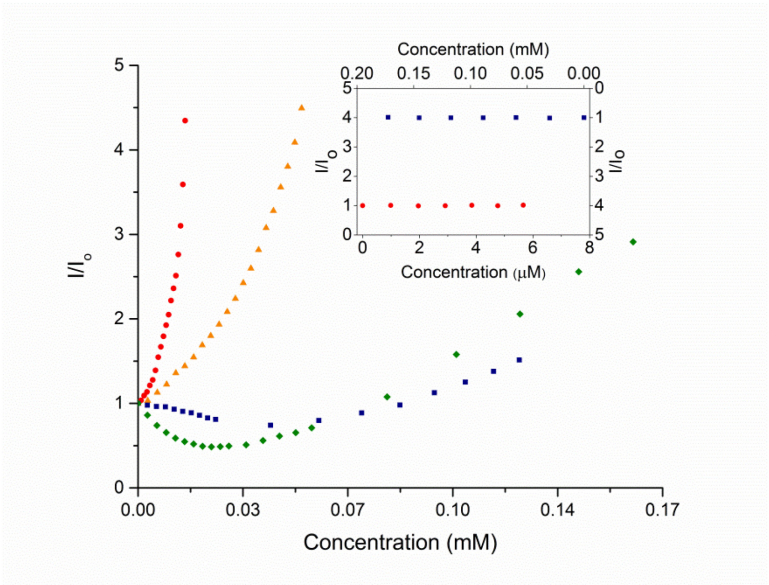

(c)

Figure 35. (a) The excitation (dotted blue) and emission (solid red) spectra of LMOF-241 in DCM. (b) Emission spectra of LMOF-241 with the incremental addition of AFB_1 in DCM. (c) The Stern-Volmer curves acquired at λ_{ex} = 340 nm and λ_{ex} = 410 nm (insert) for AFB_1 (red dot), AFB_2 (orange triangle), AFG_1 (green dimand), and OTA (blue square).

2.3.2. Results and Discussion

LMOF-241 or $Zn_2(bpdc)_2(tppe)\cdot S$ (S = guest solvent molecules) crystalizes in the monoclinic crystal system with space group *C2* (Table 5). Each Zn^{2+} coordinates to two monodentate carboxylates from bpdc ligands and two pyridine groups from tppe ligands (Figure 34a). A hexagonal cage containing 12 Zn centers, 8 bpdc ligands, and 2 tppe ligands proliferates along the c axis to form a channel; the edge-sharing channels expands into a 3 dimensional framework. The overall structure of LMOF-241 contains 3 interpenetrated frameworks with distorted hexagonal channels along the c axis. If bpdc is simplified as a 2-c node and tppe as a 4-c node, the overall structure is a 2-nodal (4,4)-c net (mog type) with Point symbol $\{4\cdot6^4\cdot8\}_2\{4^2\cdot6^2\cdot8^2\}$ (Figure 34c and d). There are currently 12 reported MOF structures with 3 fold interpenetrated mog type topology according to the ToposPro database.[140] If tppe is

simplified as two 3-c nodes, the overall structure is a 2-nodal (3,4)-c net (jeb type, or bbe-3,4-Cmmm, derived from mog) with Point symbol $\{6^3\}\{6^5{\cdot}8\}$.[4,141] To the best of our knowledge, only 1 out of the 8 reported jeb type MOF structures has a 3-fold interpenetration.[142] However the topology of LMOF-241 is unusual because of its non-centrosymmetry: two structural groups not related by any symmetry operations form 3 (2+1) interpenetrated nets.

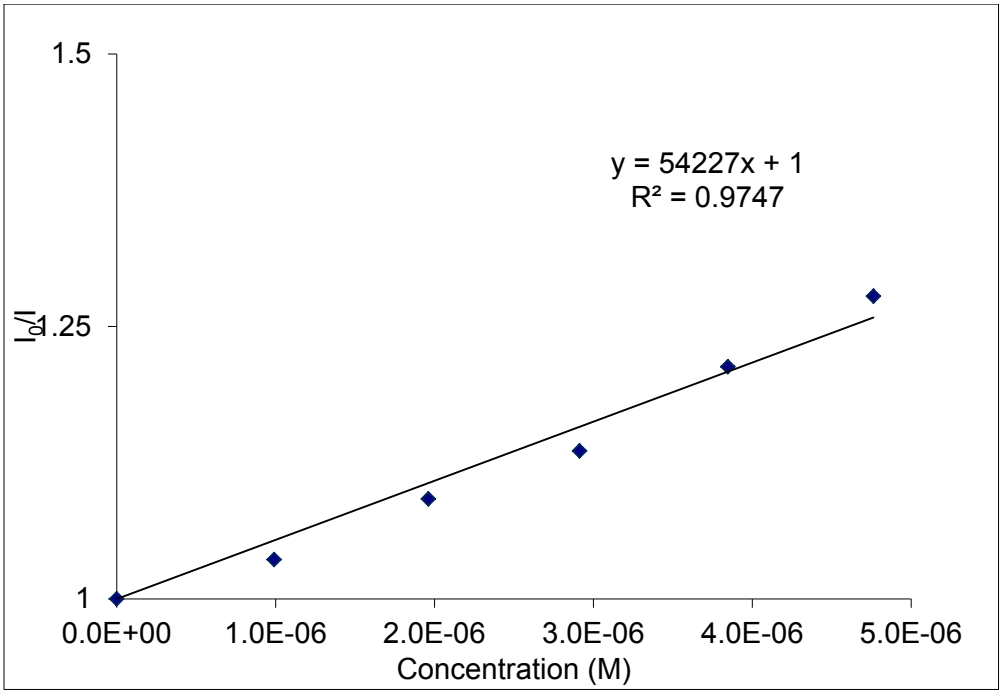

(a)

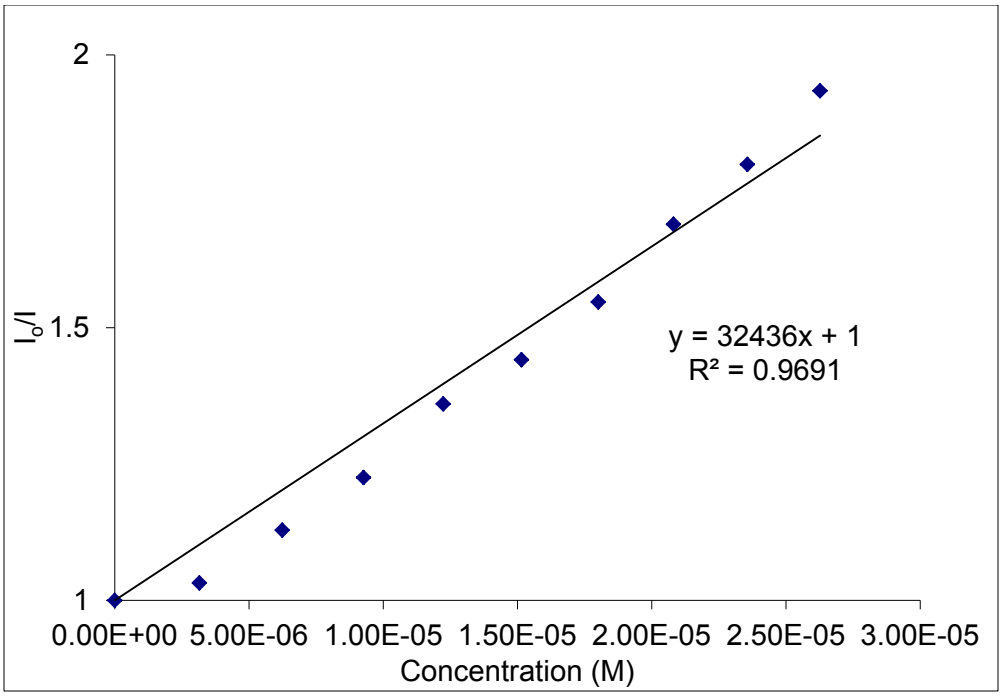

(b)

Figure 36. SV curves for AFB_1 (a) and AFB_2 (b).

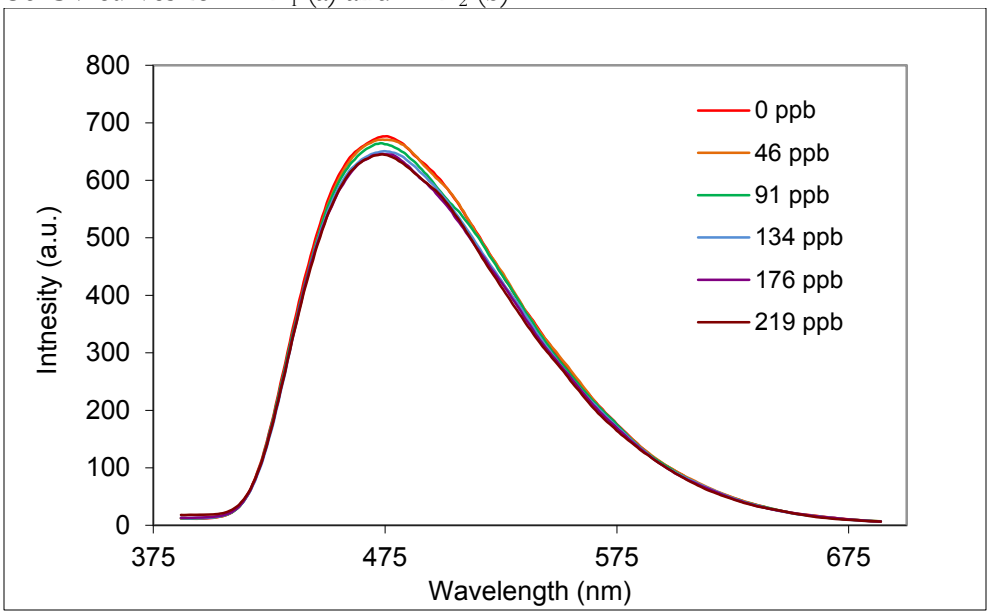

(a)

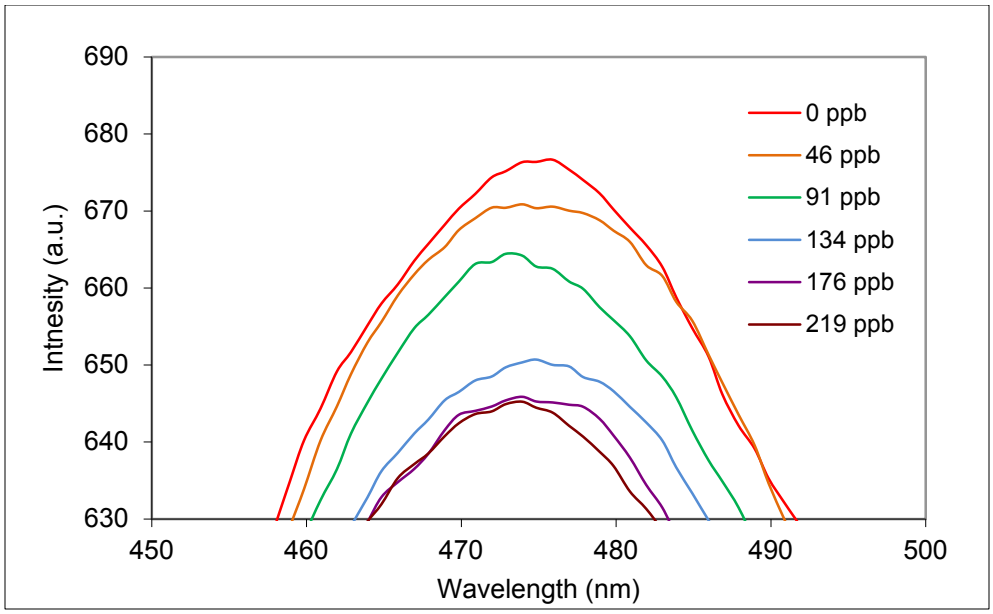

(b)

Figure 37. (a) Limit of detection of AFB_1 determination. (b) is a zoom-in of (a).

LMOF-241 exhibits ligand-based emission in the blue region (Figure 35a). Mycotoxin detection was achieved by monitoring the PL of LMOF-241 before and after the addition of anaylte. AFB_1 and AFB_2 quench the PL intensity of LMOF-241. A representative PL titration curves for AB_1 are shown in Figure 35b. AFG_1 and OTA at low concentrations enhance the PL intensity of LMOF-241; as the concentrations pass certain thresholds, the PL intensity starts decreasing. The Stern-Volmer (SV) equation, $I_o/I = K_{sv}[Q] + 1$, where Io is the initial emission peak intensity, I is the emission peak intensity after the addition of analyte, [Q] is molar concentration of the analyte (quencher), K_{sv} is the quenching efficiency, was used to quantitatively evaluate the performance of LMOF-241 as mycotoxin sensor. For AFB_1 and AFB_2 at low concentrations, the I_o/I is linearly proportional to concentration respectively with a y intercept 1; the slope is the K_{sv}. For AFB_1, K_{sv} is 54227 M^{-1}, which is 1.8 times of that of AFB_2 (32436 M^{-1}), which indicates the strong selectivity of LMOF-241 to AFB_1 (Figure 36). The detection limit for AFB_1 is 15 ppb (Figure 37). The SV curves for

AFG_1 and OTA bend downwards first at low concentration region, and this trend is reversed after certain concentration thresholds. Compared to OTA, AFG_1 is more efficient in enhancing and quenching the emission intensity since the falling and rising of slopes are steeper. The threshold concentration from enhancement to quenching of AFG_1 is lower than that of OTA. In addition to intensity change, AFG_1 causes a blue shift of the emission peak and OTA causes a red shift. Such turn-on and turn-off responses are unique fingerprints of these two mycotoxins.

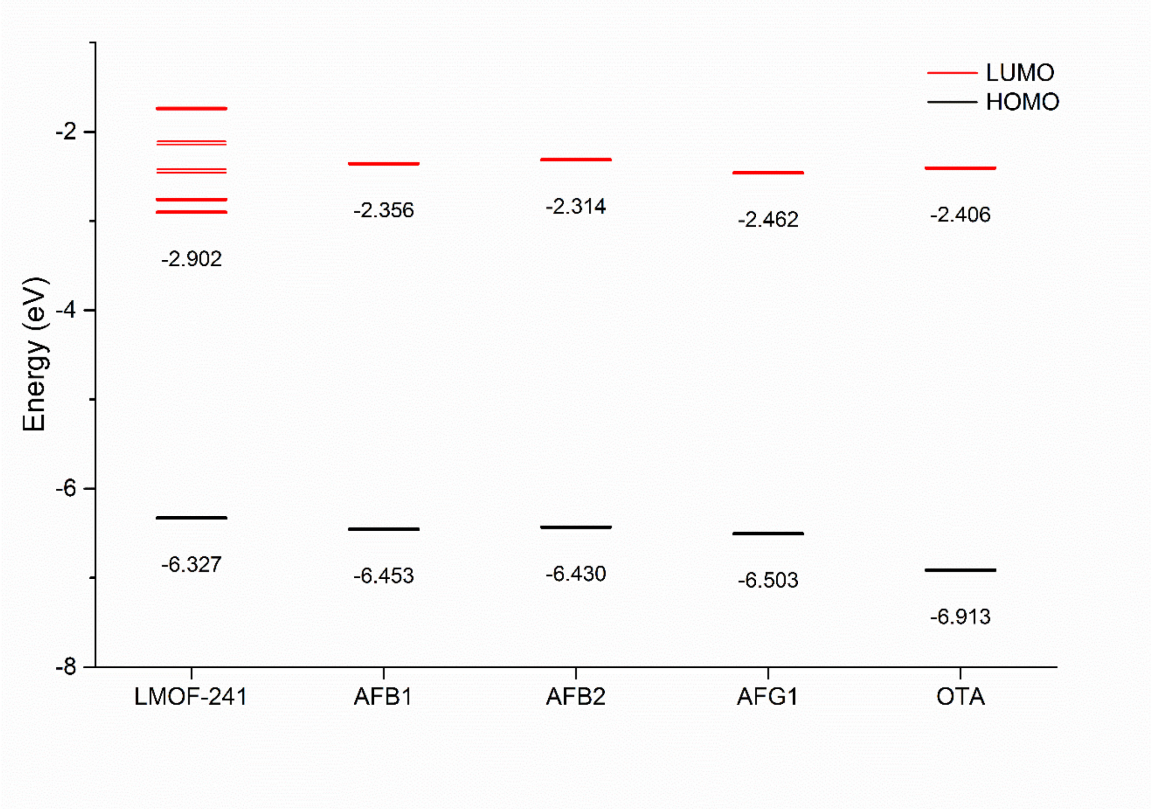

Figure 38. Calculated frontier orbital energies for LMOF-241 (fragment model) and analytes at B3LYP/DGDZVP.

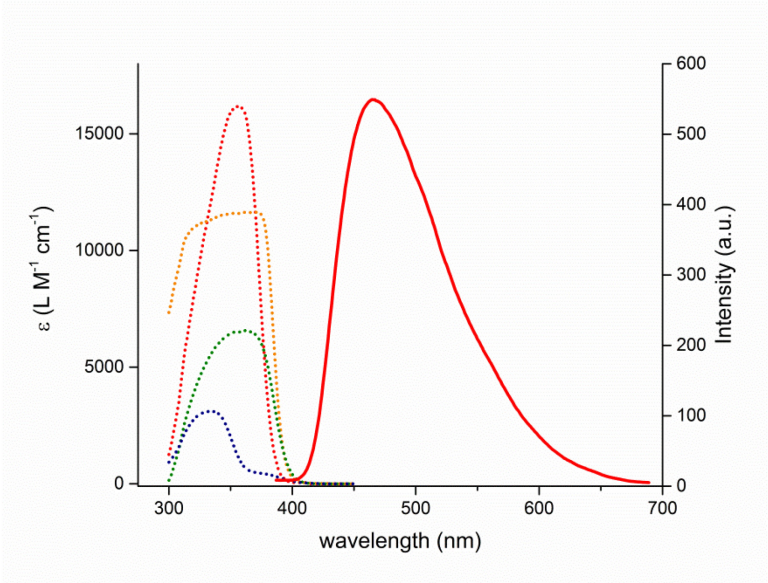

(a)

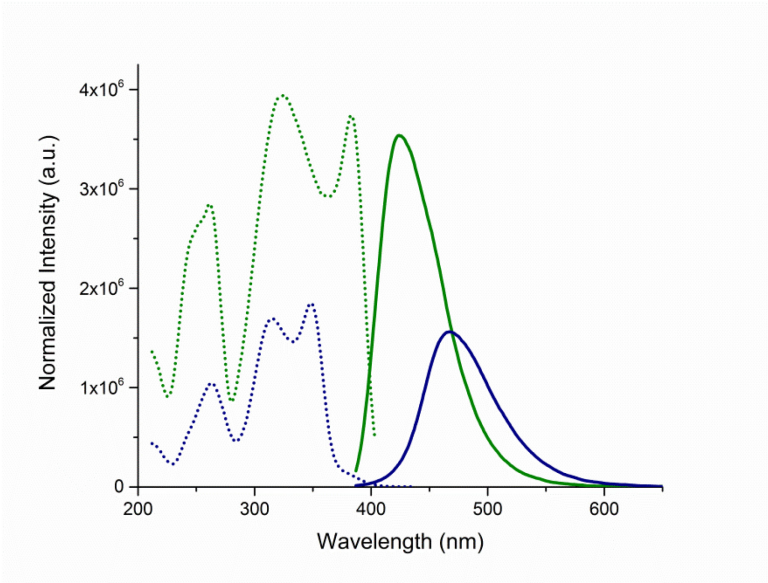

(b)

Figure 39. (a) Molar absorptivity of AFB1 (dotted red), AFB_2 (dotted orange), AFG_1 (dotted green), and OTA (dotted blue), and the emission spectrum of LMOF-241 in DCM (λ_{ex} = 340 nm). (b) Excitation spectra (dotted lines) and emission spectra (solid lines, λ_{ex} = 340 nm) of AFG_1 (green), and OTA (blue) in DCM with intensity normalized to concentration.

The quenching of LMOF-241's emission by AFB_1 and AFB_2 is likely due to an electron transfer mechanism that we previously discussed for LMOF-based sensors.[62,70-72] As

shown in Figure 38, upon excitation, electrons can transfer from the conduction band of LMOF-241 (S_5 and above) to LUMOs of AFB_1 and AFB_2, then non-radiatively relax to their HOMOs. It is also possible according to Hao *et al*, that electrons can directly transfer from the valence band of LMOF-241 to the LUMOs of analytes, facilitated by the guest-host interactions (such as π-π interaction and hydrogen bond).[143] In any case, a sufficient amount of excitation energy is needed to overcome the energy barrier for electron transfer. For example, with λ_{ex} = 340 nm, efficient quenching is achieved; with λ_{ex} = 410 nm the SV curve becomes flat as shown in the insert of Figure 35. However, the electron transfer mechanism alone could not explain LMOF-241's selectivity towards AFB_1 over AFB_2. To better understand LMOF-241's selectivity, the energy transfer aspect should also be considered.

The spectral overlap between the absorption of analytes and the emission of LMOF-241 is very limited which hinders the energy transfer from LMOF-241 to AFB_1 and AFB_2 (Figure 39a).[144] But the absorption of AFB_1 and AFB_2 align almost perfectly with the excitation energy fed to the analyte-sensor system (λ_{ex} = 340 nm). This indicates both AFB_1 and AFB_2 compete with LMOF-241 for excitation energy, while AFB_1 is a stronger competitor as its molar absorptivity is greater than that of AFB_2. AFG_1 and OTA could also share the excitation energy with LMOF-241. Unlike AFB_1 and AFB_2, AFG_1 and OTA relax the excitation radiatively, which may be the reason for emission enhancement of LMOF-241 at low analyte concentrations. AFG_1 is more capable of absorbing the excitation energy (higher ε) and the subsequent emission (higher emission intensity) than OTA, which could explain AFG_1 causes a more rapid enhancement.

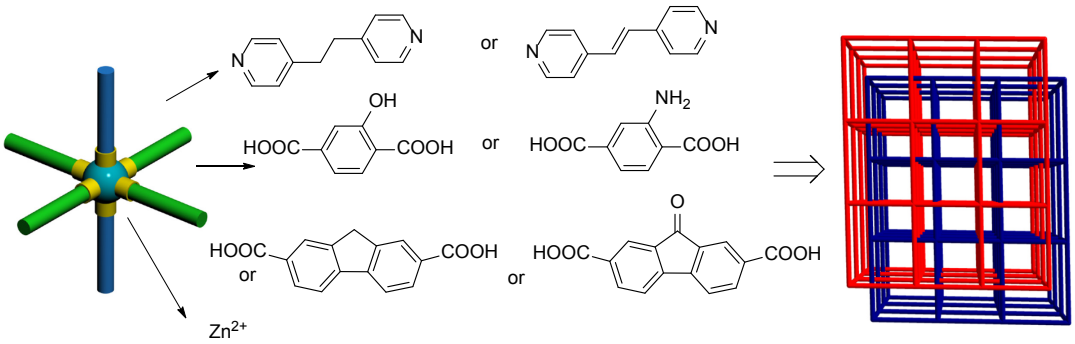

Figure 40. An illustration of the formation of a series of LMOFs with the paddle-wheel type SBU.

Table 6. Single crystal data of LMOF-212 based on the SQUEEZE model

Compound	LMOF-212 or $Zn_2(hfdc)_2(bpe)$
Formula	$C_{21}H_{13}NO_4Zn$
M	408.71
Crystal system	Orthorhombic
Space group	P nna
a/Å	18.533(2)
b/Å	16.1422(18)
c/Å	23.345(3)
α/°	90
β/°	90
γ/°	90
V/Å^3	6983.9(14)
Z	8
Temperature/K	100(2)
λ (radiation wavelength)/Å	0.71073
D (g/cm^3)	0.777
Reflections collected	59877
R1[a] [I > 2σ(*I*)]	0.0528
wR2[b] [I > 2σ(*I*)]	0.1667
Goodness-of-fit	1.105
Sample ID	ZH3-74C

[a] $R1 = \sum | F_o - F_c | / \sum | F_o |$
[b] $wR2 = \sum[w(F_o^2 - F_c^2)^2] / w(F_o^2)^2]^{1/2}$

Table 7. Single crystal data of LMOF-221 based on the SQUEEZE model

Compound	LMOF-221 or $Zn_2(ofdc)_2(bpee)$
Formula	$C_{44}H_{22}N_2O_{10}Zn_2$
M	845.40
Crystal system	Monoclinic
Space group	P 21/c

a/Å	16.0925(18)
b/Å	20.907(2)
c/Å	21.242(2)
α/°	90
β/°	104.912(2)
γ/°	90
V/Å^3	6905.8(13)
Z	4
Temperature/K	150(2)
λ (radiation wavelength)/Å	0.71073
D (g/cm^3)	0.813
Reflections collected	69833
R1[a] [I > 2σ(*I*)]	0.0365
wR2[b] [I > 2σ(*I*)]	0.0991
Goodness-of-fit	0.957
Sample ID	AB1-13B

[a] $R1 = \sum | F_o - F_c | / \sum | F_o |$
[b] $wR2 = \sum[w(F_o^2 - F_c^2)^2] / w(F_o^2)^2]^{1/2}$

Table 8. Single crystal data of LMOF-292

Compound	LMOF-292 or $Zn_2(bdc\text{-}NH_2)_2(bpee)$
Formula	$C_{30.12}H_{23.33}N_{4.71}O_{8.7}Zn_2$
M	721.59
Crystal system	Triclinic
Space group	P -1
a/Å	10.9081(2)
b/Å	10.9133(3)
c/Å	16.3061(4)
α/°	85.6950(10)
β/°	83.9700(10)
γ/°	74.5850(10)
V/Å^3	1858.70(8)
Z	2
Temperature/K	100(2)
λ (radiation wavelength)/Å	0.41328
D (g/cm^3)	1.289
Reflections collected	11168
R1[a] [I > 2σ(*I*)]	0.0824
wR2[b] [I > 2σ(*I*)]	0.2101
Goodness-of-fit	1.108
Sample ID	DB1-152A

[a] $R1 = \sum | F_o - F_c | / \sum | F_o |$
[b] $wR2 = \sum[w(F_o^2 - F_c^2)^2] / w(F_o^2)^2]^{1/2}$

To further assess LMOFs as AFB_1 sensors, a series of LMOFs with the paddle-wheel type of SBU is proposed (some already synthesized by our group, Figure 40): LMOF-211 or $Zn_2(ofdc)_2(bpe)$, LMOF-212 or $Zn_2(hfdc)_2(bpe)$, LMOF-221 or $Zn_2(ofdc)_2(bpee)$, LMOF-222 or $Zn_2(hfdc)_2(bpee)$, LMOF-281 or $Zn_2(bdc\text{-}OH)_2(bpe)$ (bdc-OH = 2-hydroxyterephthalate), LMOF-282 or $Zn_2(bdc\text{-}NH_2)_2(bpe)$ (bdc-NH_2 = 2-aminoterephthalate), LMOF-291 or $Zn_2(bdc\text{-}OH)_2(bpee)$, and LMOF-292 or $Zn_2(bdc\text{-}NH_2)_2(bpee)$. All of these LMOFs are expected to share the same topology with 2-fold interpenetration (6 coordinated uninodal net with the Point symbol of $\{4^{12}\cdot6^3\}$). Single crystal analysis was performed on LMOF-212, 221, and 292 (Table 6, Table 7, and Table 8). LMOF-211, 221, 281, 282, 292 were tested for the detection of AFB_1. Aliquots of AFB_1 solution (0.32 mM in DMF) were added to 1 mL LMOF suspension under constant stirring (0.4 mg/mL in DMF). PL spectra were recorded before and after the addition of analyte.

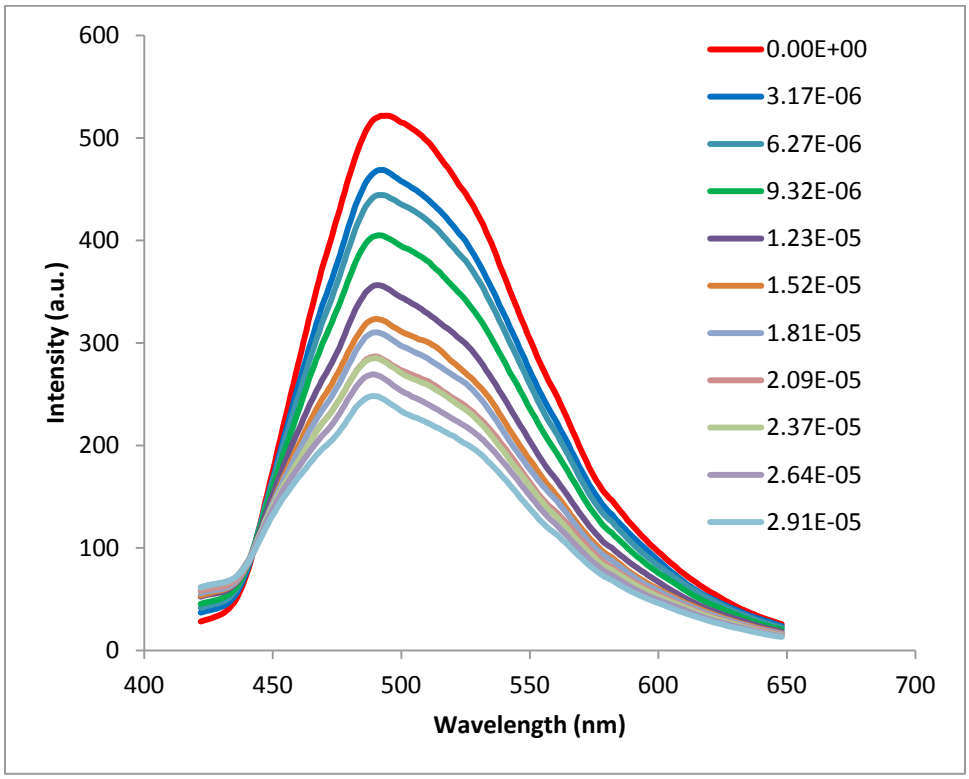

(a)

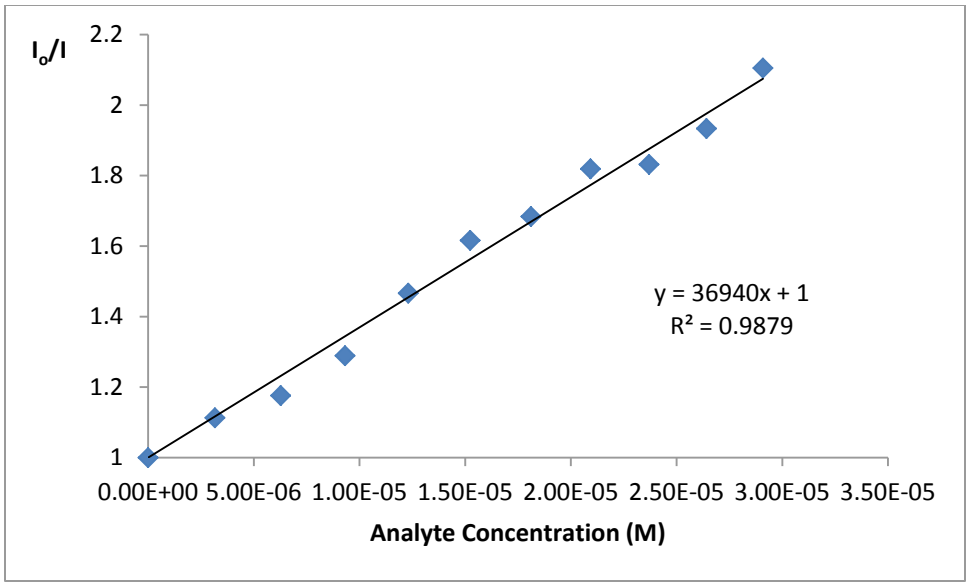

(b)

Figure 41. (a) The PL titration curves of LMOF-211 with the addition of AFB_1 (λ_{ex} = 300 nm). (b) The Stern-Volmer curve of LMOF-211.

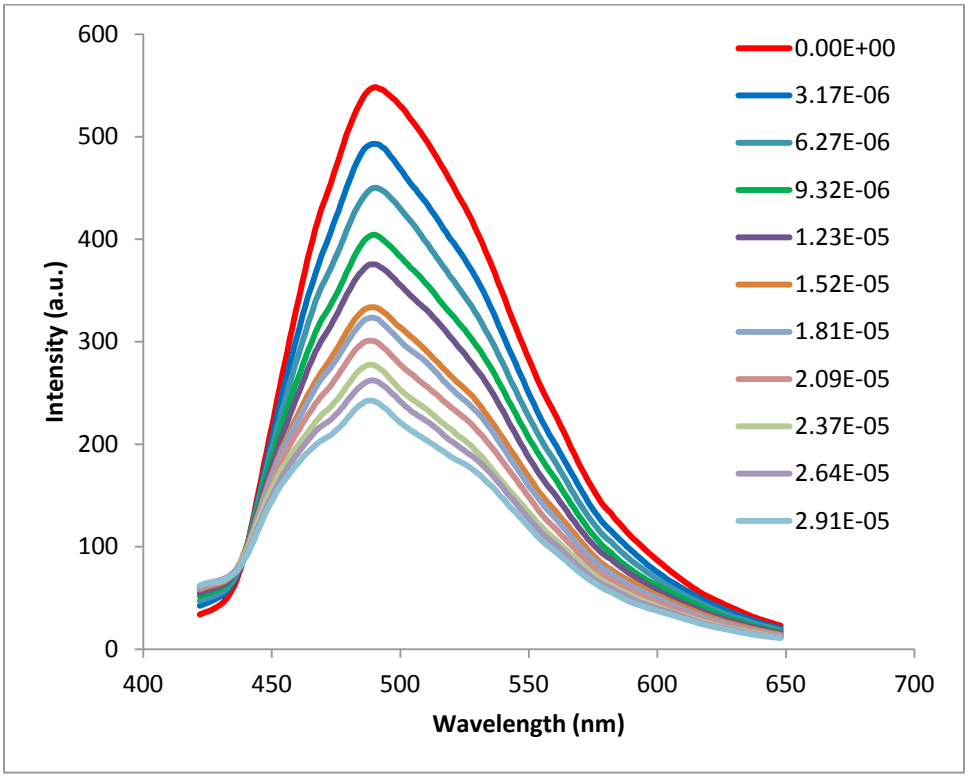

(a)

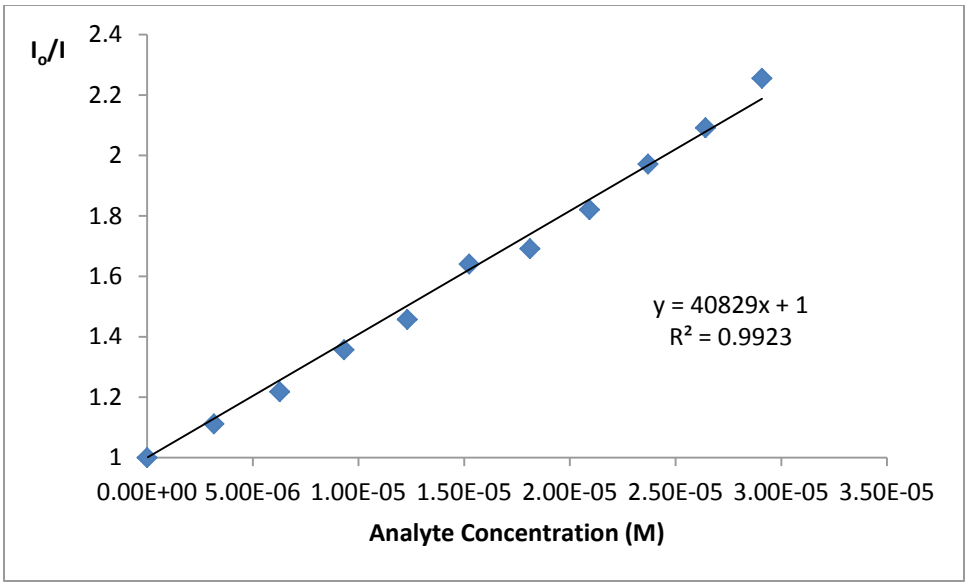

(b)

Figure 42. (a) The PL titration curves of LMOF-221 with the addition of AFB_1 (λ_{ex} = 300 nm). (b) The Stern-Volmer curve of LMOF-221.

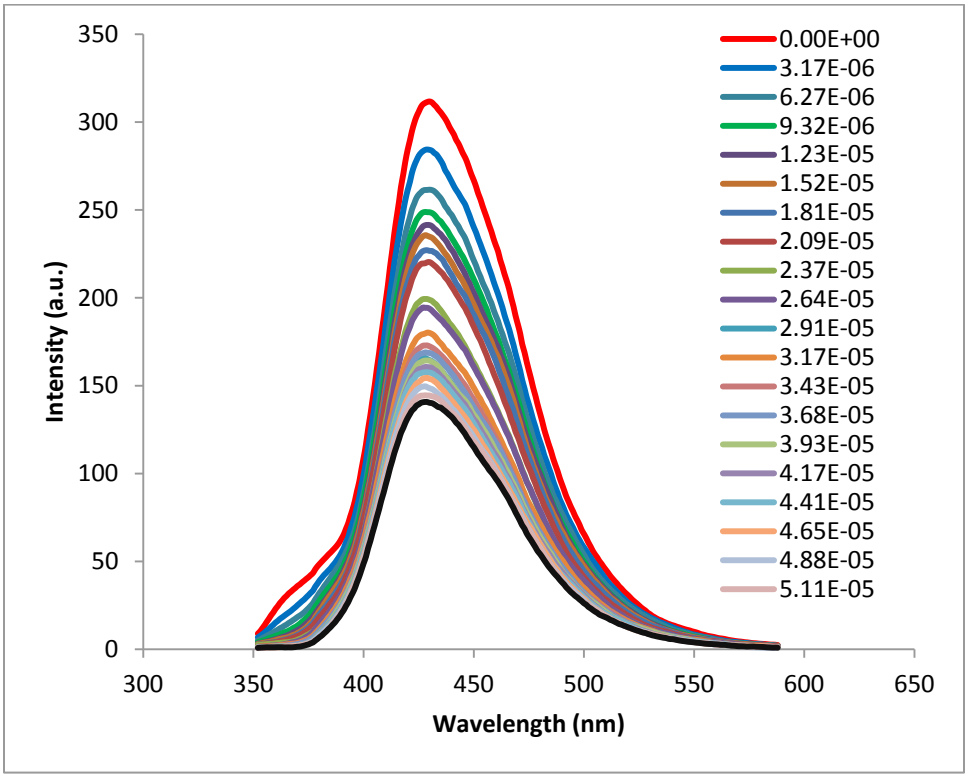

(a)

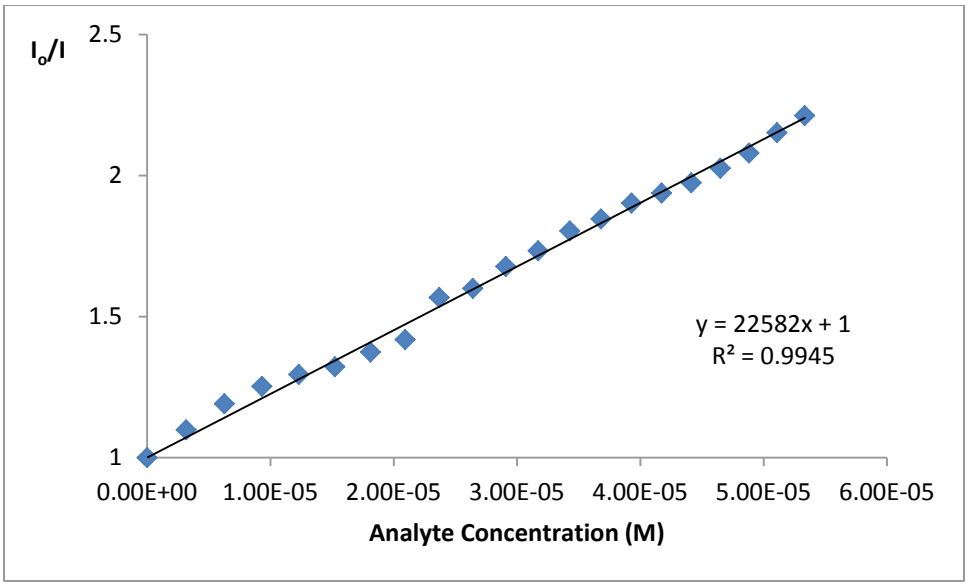

(b)

Figure 43. (a) The PL titration curves of LMOF-281 with the addition of AFB_1 (λ_{ex} = 325 nm). (b) The Stern-Volmer curve of LMOF-281.

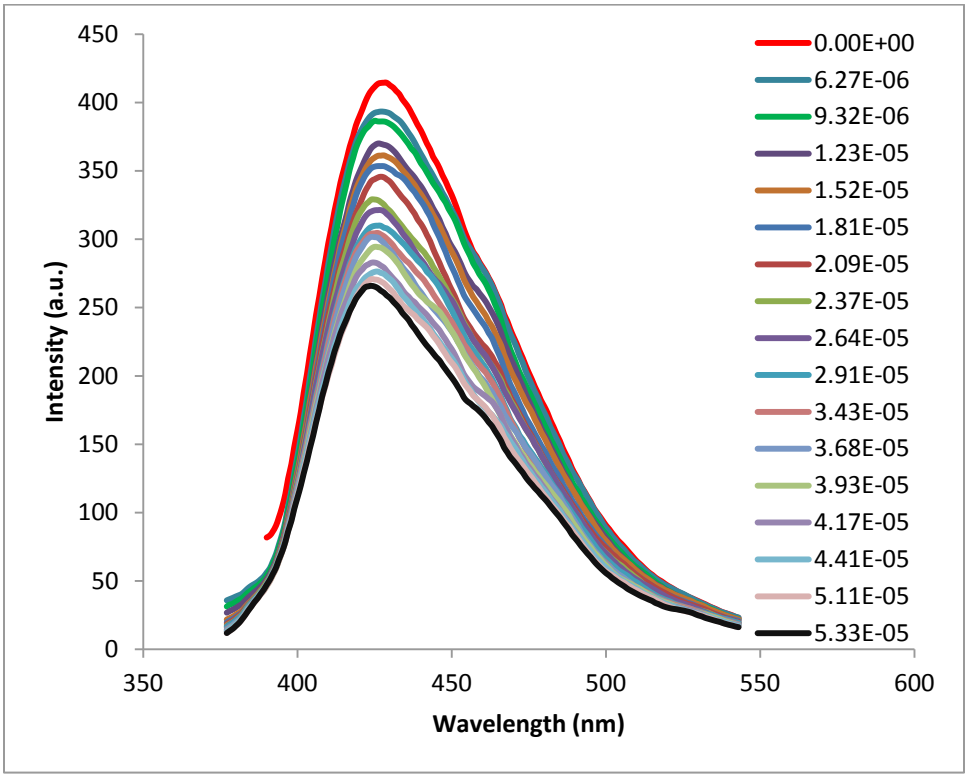

(a)

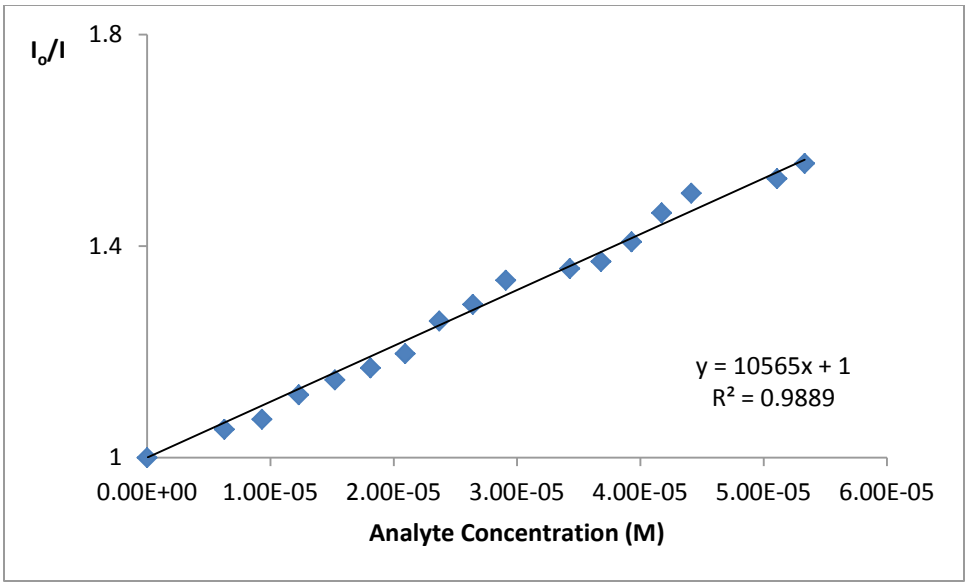

(b)

Figure 44. (a) The PL titration curves of LMOF-282 with the addition of AFB_1 (λ_{ex} = 350 nm). (b) The Stern-Volmer curve of LMOF-282.

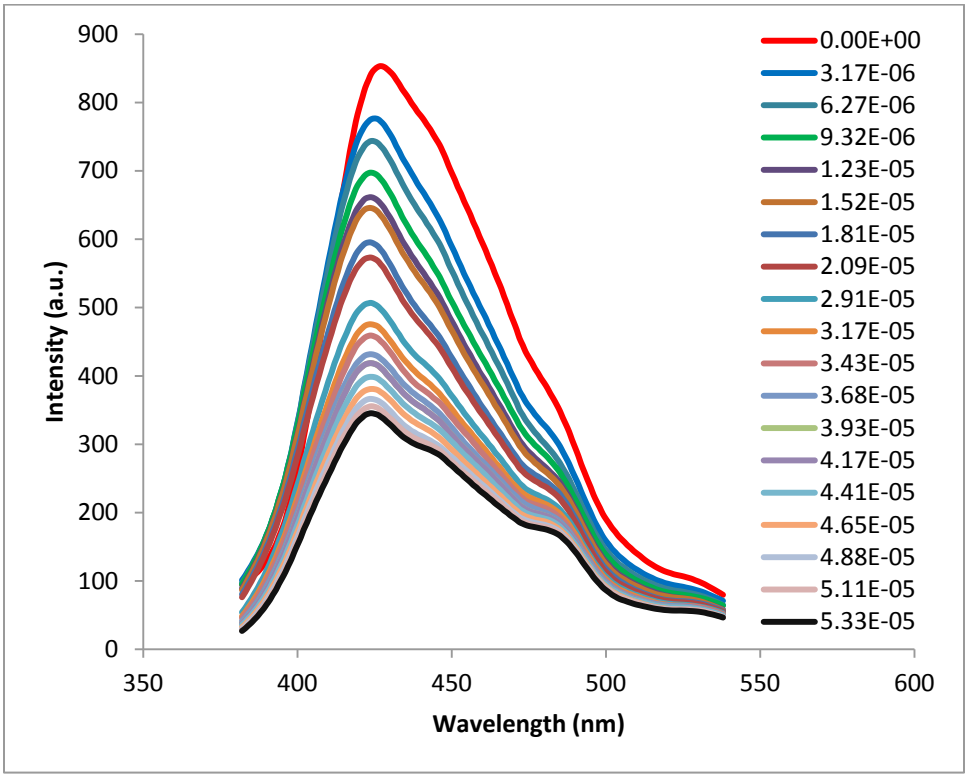

(a)

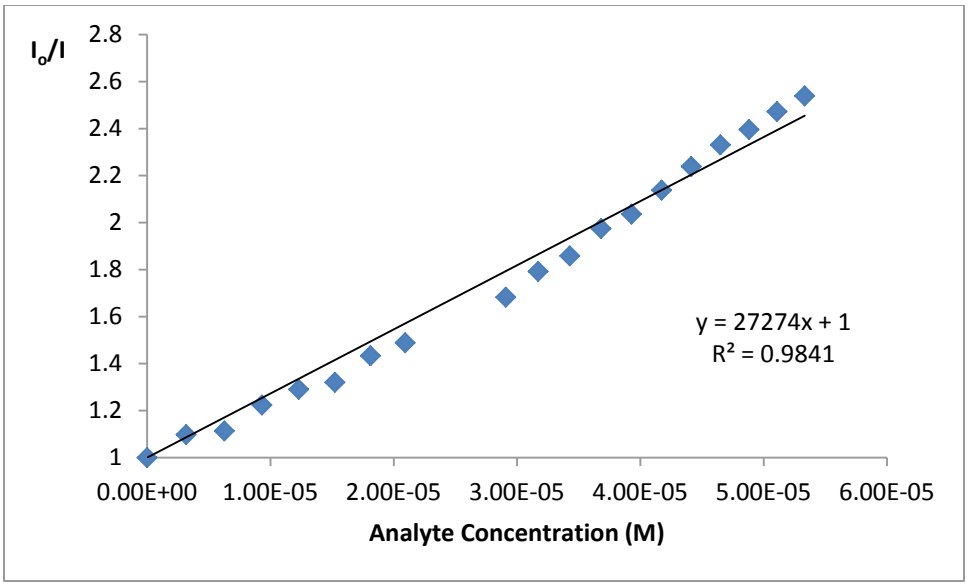

(b)

Figure 45. (a) The PL titration curves of LMOF-292 with the addition of AFB_1 (λ_{ex} = 350 nm). (b) The Stern-Volmer curve of LMOF-292.

Table 9. Summary of K_{sv} for AFB_1

LMOF	Sample ID	Compound	K_{sv}
211	AB1-38A	$Zn_2(ofdc)_2(bpe)$	36940
221	AB1-38C	$Zn_2(ofdc)_2(bpee)$	40829
281	AB1-34B	$Zn_2(bdc\text{-}OH)_2(bpe)$	22582
282	AB1-36B	$Zn_2(bdc\text{-}NH_2)_2(bpe)$	10565
292	AB1-36A	$Zn_2(bdc\text{-}NH_2)_2(bpee)$	27274

Preliminary PL titration data show that AFB1 quenches the emission of the selected LMOFs (Figure 41 to Figure 45 and Table 9). LMOFs with larger pores generally are more sensitive to AFB_1 as indicated by their respective K_{sv} values. For example, LMOF-211 and 221 were constructed of a larger ligand (fdc-based) than that of LMOF-281, 282, and 292 (bdc-based); and the K_{sv} value of LMOF-211 and 221 are greater than those of LMOF-281, 282, and 292.

2.3.3. Conclusions

We have designed and synthesized a new compound, LMOF-241 and demonstrated for the first time the use of this compound for myctotoxin detection. LMOF-241 is capable of differentiating several major Aflatoxins and Orchratoxin A. LMOF-241 is most sensitive of Aflatoxin B_1 with detection limit in the ppb level. We have also studied the the electronic properties of LMOF-241 and selected analytes from a theoretical perspective. Possible electron and energy transfer mechanisms are addressed. LMOF-241 has great potential for effective mycotoxin detection. A preliminary study of a group of LMOFs with same topology but different building units indicates that larger pores might facilitate the diffusion of analyte and lead to greater sensitivity.

3. LMOFs as Phosphors

3.1. The Design and Characterization of a New LMOF Phosphor

3.1.1. Introduction

Light-emitting diodes (LEDs), one of the main branches of solid-state lighting (SSL) technology, have rapidly emerged in various lighting applications, owing to their higher efficiency, longer lifetime, and lower energy consumption relative to incandescent and fluorescent bulbs. White light-emitting diodes (WLEDs) are of particular importance because of the high demand for general illumination and displays. The energy impact of LEDs is profound: The U.S. Environmental Protection Agency (EPA) estimates that the nation can save nearly $700 million per year on energy cost, if every household substitutes just one incandescent lamp with an ENERGY STAR rated LED.[145,146] The U.S. Department of Energy also acknowledges SSL as a significant climate change solution as this technology could cut the nation's lighting energy consumption by almost one half.[147] In one of the largest retrofitting projects in the US, New York City plans to replace all of its 250,000 street

lights with LEDs, aiming at a 30% drop of greenhouse gas emission by 2017.[148] One way to construct WLEDs is by the combination of three single-chip diodes, namely red, green, and blue (RGB) LEDs. A drawback of this multi-chip system is its high cost. Another method is coating phosphors on single-chip LEDs, which are also known as phosphor-converted WLEDs (PC-WLEDs). For example, either a mixture of RGB or other multicomponent phosphors or a white phosphor which emits throughout the visible region can be coated on UV LEDs.[149-155] Similarly, yellow phosphors can be excited by blue LEDs to produce white light, such as the commercially available YAG:Ce^{3+} coupled with blue LEDs.[156-158] Considering the wide availability and low cost of blue LEDs, yellow phosphor based PC-WLEDs are preferred.[159] The vast majority of currently available yellow phosphors rely heavily on the rare-earth elements.[160] However, due to the increasing demand of these elements in many other high-tech applications, their prices have increased by 4 to 49 times from 2001 to 2011. For example, the prices of Y, Eu, and Tb, the three essential ingredients of phosphors used in general lighting technologies have increased by 400%, 600%, and 1600% respectively.[161] The search for rare-earth-free yellow phosphors is becoming increasingly urgent.[161]

Molecular aggregation often plays a key role in the PL properties of a phosphor. Upon aggregation, the PL of a phosphor may be subject to aggregation-caused quenching (ACQ) and/or aggregation-induced emission (AIE).[162] Phosphors with AIE characteristics are generally more appealing. In designing highly efficient yellow-emitting phosphors, our strategy is to preselect an AIE type ligand with appropriate emission energy. We began by evaluating the HOMO-LUMO energy gap (ΔE) of a series of conjugated organic ligands with a focus on chromophores containing the tetraphenylethylene (tpe) core, which is a typical AIE moiety.[162,163] As shown in Figure 46, varying the conjugation of organic

chromophores can systematically tune ΔE. For example, H_4tcpe (tetrakis(4-carboxyphenyl)ethylene) (L_3) is a reasonable starting point since its internal quantum yield (IQY) is as high as 47%.[164] However, its emission is too close to blue (λ_{em} = 480 nm).[51] To red-shift the emission peak, we decrease ΔE by increasing the arm length extended from the tpe core (e.g. L_4 to L_8 in Figure 46). Thus we synthesized the targeted ligand H_4tcbpe (L_7), 4',4''',4'''',4'''''-(ethene-1,1,2,2-tetrayl)tetrakis ([1,1'-biphenyl]-4-carboxylic acid) which emits near 540 nm.[165]

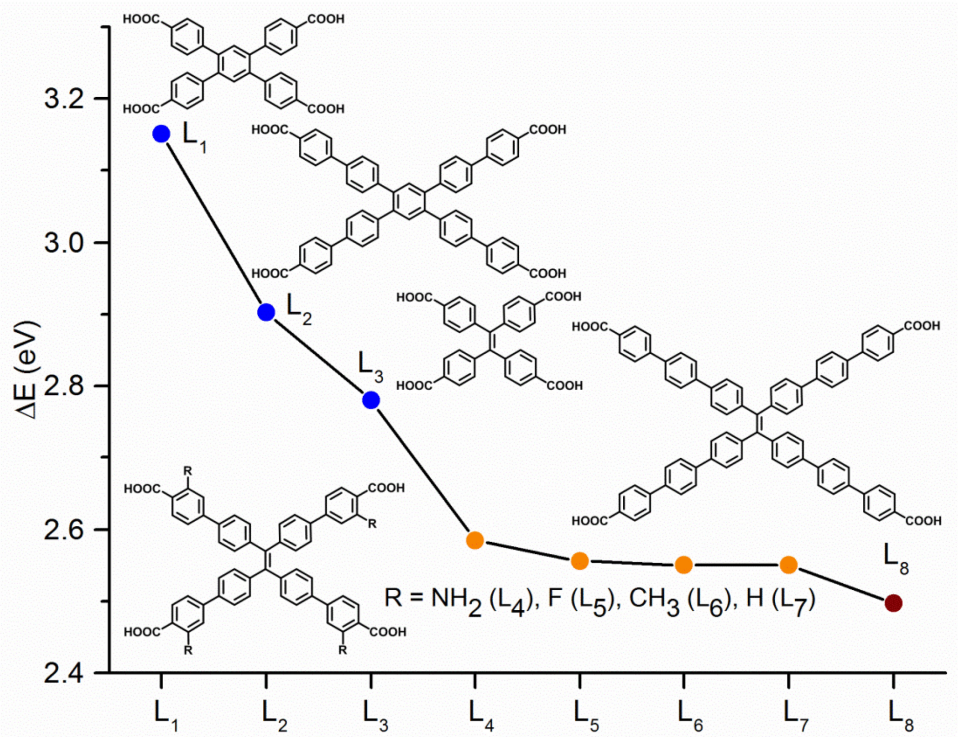

Figure 46. Estimated HOMO-LUMO energy gaps of ligands at B3LYP/DGDZVP. ΔE is normalized to the experimental value of L_7 (or H_4tcbpe) extrapolated from the diffuse reflectance spectrum.

MOFs have been extensively studied for various potential applications.[8,9,13,14,17,39,116,163,166-169] The strong luminescence of a number of MOFs, and especially their ability in immobilizing molecular chromophores, have further facilitated their

possible use as phosphors.[28,30,170] As potential phosphors, LMOFs have several intrinsic advantages: The diverse building components available for the construction of LMOFs offer various sources of fluorescence, which makes it possible to design phosphors independent of rare-earth elements or elements with adverse environmental impacts (such as cadmium and selenium) — the former are the essential ingredients in current commercially available inorganic phosphors, and the latter are the key components in quantum-dot based phosphors.[171] The synthesis conditions for LMOFs are much milder than those for solid-state inorganic phosphors; the fabrication process only requires moderate heating or even no heating (e.g. reactions at room temperature), which conserves energy from the very beginning of their life cycle. Anchoring organic chromophores, especially the AIE-type, into the rigid MOF backbone effectively inhibits non-radiative decay involving ligand rotation, vibration, and torsion, potentially enhancing the overall fluorescence of the resulting compounds.[51] Our recent studies on Zn-based LMOFs have revealed that PL emissions in these structures are primarily ligand based or involve LLCT, depending on the number and nature of the chosen ligands.[62,70-72,94,124,144] Here, we assemble an LMOF using zinc (II) as nodes and the highly luminescent near-yellow emitting chromophore, H_4tcbpe, as linker. Upon blue excitation, the resulting LMOF compound shows ligand-based yellow emission with exceptionally high quantum yield.

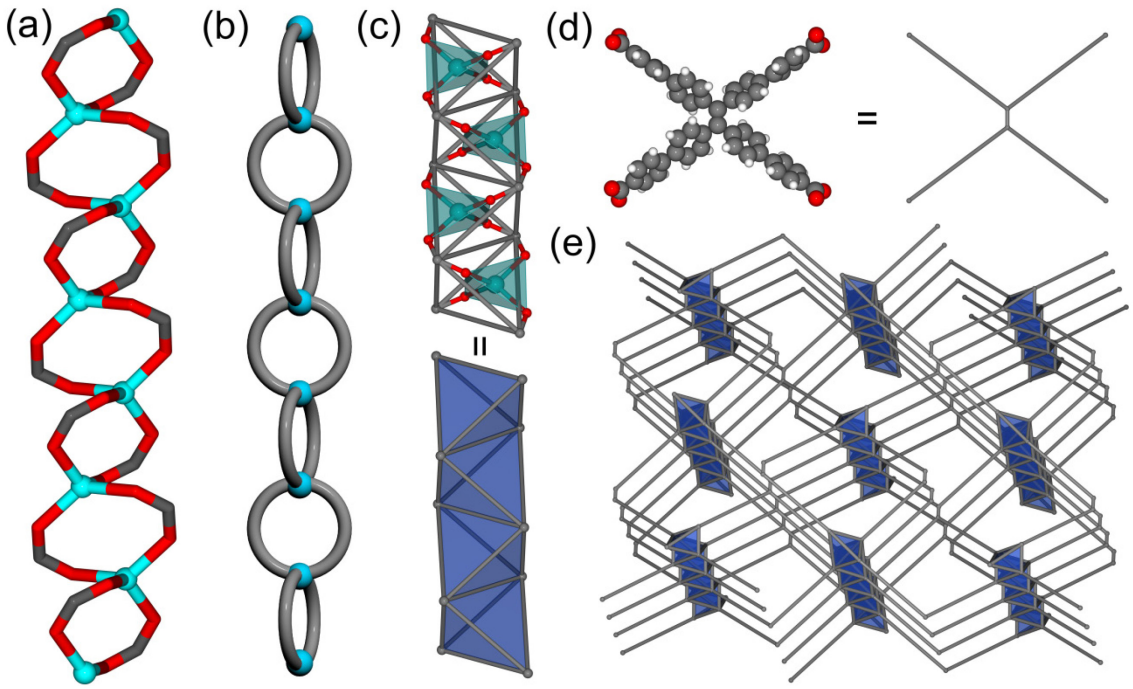

Figure 47. (a) A chain formed along the c axis containing alternating eight-membered rings. (b) An illustration of the chain emphasizing the alternating rings. (c) The polyhedral representation of the SBU as an infinite rod of edge-sharing tetrahedra. (d) The tcbpe ligand simplified as a butterfly shape. (e) The overall simplified structure of LMOF-231 showing 1D rod SBU and 1D open channel along the c axis. Color code: H (white in (d), omitted for clarity in (a) and (c)), C (grey), O (red), Zn (aqua).

Table 10. Single crystal data of LMOF-231 based on the SQUEEZE model

Compound	Zn_2(tcbpe)·*x*DMA (LMOF-231)
Formula	$C_{54}H_{32}O_8Zn_2$
M	939.53
Crystal system	Monoclinic
Space group	C 2/c
a/Å	36.929(5)
b/Å	31.080(4)
c/Å	11.8533(17)
α/°	90.00
β/°	99.228(2)
γ/°	90.00
V, Å^3	13429(3)
Z	8
Temperature (K)	100(2)
λ (radiation wavelength) Å	0.7749
D, g/cm^3	0.929
Reflections collected	76786
R1^a [I > 2σ(*I*)]	0.0898

wR2[b] [I > 2σ(*I*)]	0.2803
Goodness-of-fit	1.058
CCDC No.	1004908

[a] $R1 = \sum | F_o - F_c | / \sum | F_o |$
[b] $wR2 = \sum[w(F_o^2 - F_c^2)^2] / w(F_o^2)^2]^{1/2}$

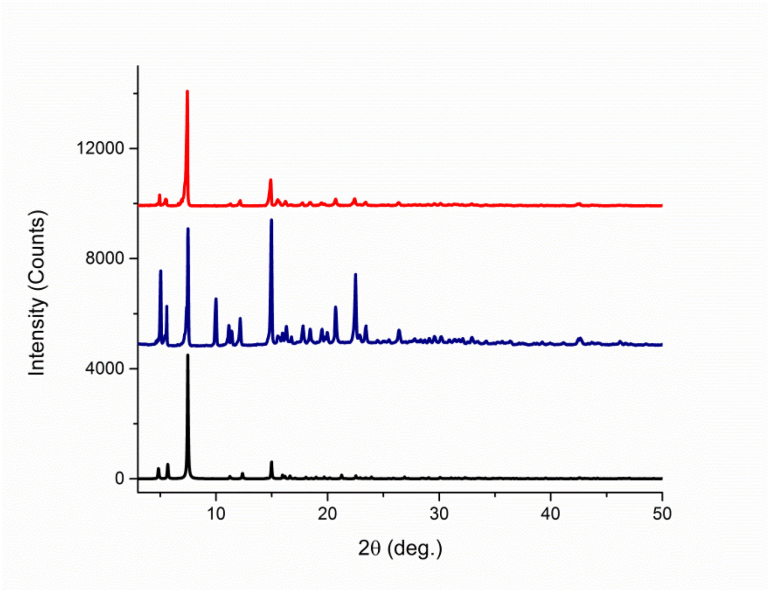

Figure 48. PXRD patterns of actived sample LMOF-231' (top), as-made sample LMOF-231 (middle), and simulated pattern from the single crystal data (bottom).

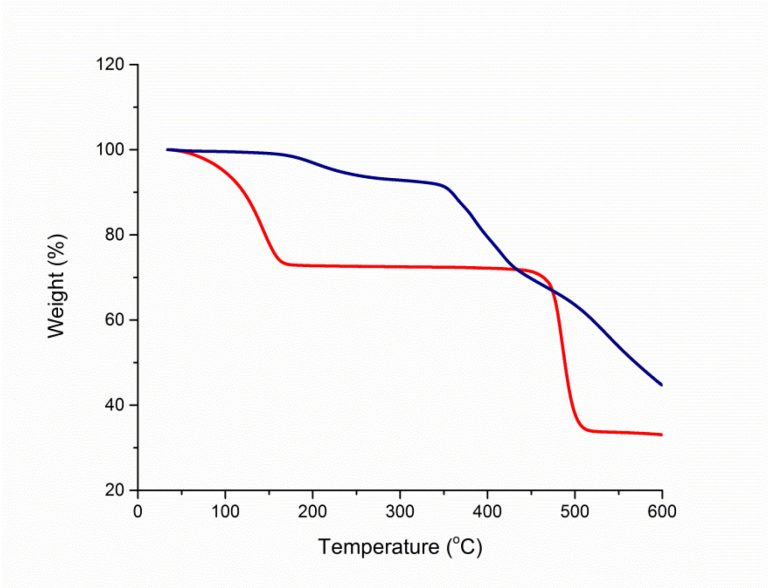

Figure 49. Thermogravimetric profile of H_4tcbpe (blue) and LMOF-231 (red) under nitrogen flow.

3.1.2. Results and Discussion

Zn_2(tcbpe)·*x*DMA (DMA = N, N-dimethylacetamide) or LMOF-231 was synthesized solvothermally (120 °C, 48 hours). It crystallizes in the monoclinic crystal system with space group *C2/c* (Table 10). Each Zn (II) tetrahedrally coordinates to O atoms from four different tcbpe ligands. All of the carboxylate groups are bidentate with each O atom connecting a different Zn (II). Two Zn, two C, and four O atoms form an eight-membered ring in a chair-boat confirmation, which differs from the boat-boat confirmation of the rings in Zn(tbip) (H_2tbip = 5-(*tert*-butyl)isophthalic acid).[172] The rings alternate along the *c* axis to form a 1D chain (Figure 47a-c) that can be regarded as an infinite SBU. This type of rod-shaped SBU effectively prevents framework interpenetration.[173,174] Each tcbpe ligand bridges four adjacent chains (rods) to afford the three-dimensional (3D) framework with 1D channel along the *c* axis, as shown in Figure 47. The overall structure is a new (3,6)-c net with Point symbol $\{3^6.4^4.8^4.9\}_2\{8^3\}$ (obtained from TOPOS).[2,140] The framework is porous with a BET surface area of 833 m^2/g. LMOF-231 is thermally stable to 460 °C, making it more robust than H_4tcbpe which decomposes around 350 °C, as indicated by the thermogravimetric analysis (Figure 49).

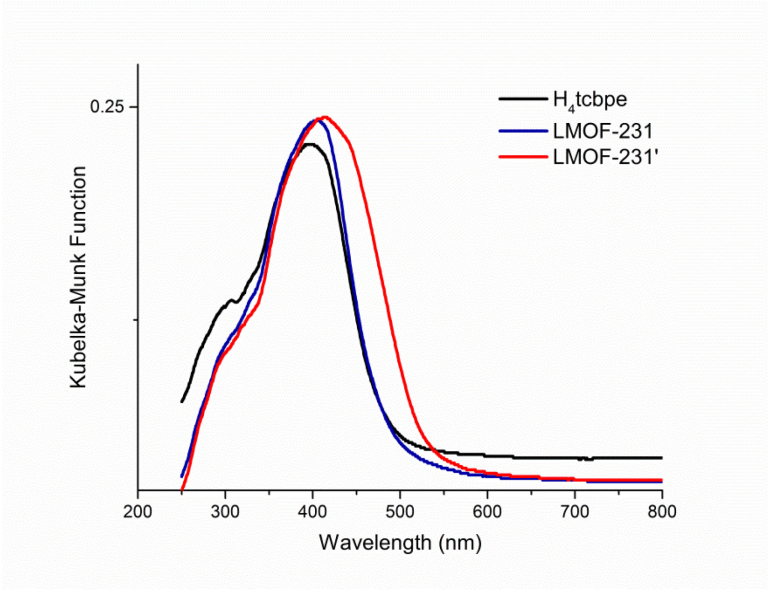
0.25
Kubelka-Munk Function
H4tcbpe
LMOF-231
LMOF-231'
200
300
400
500
600
700
800
Wavelength (nm)

(a)

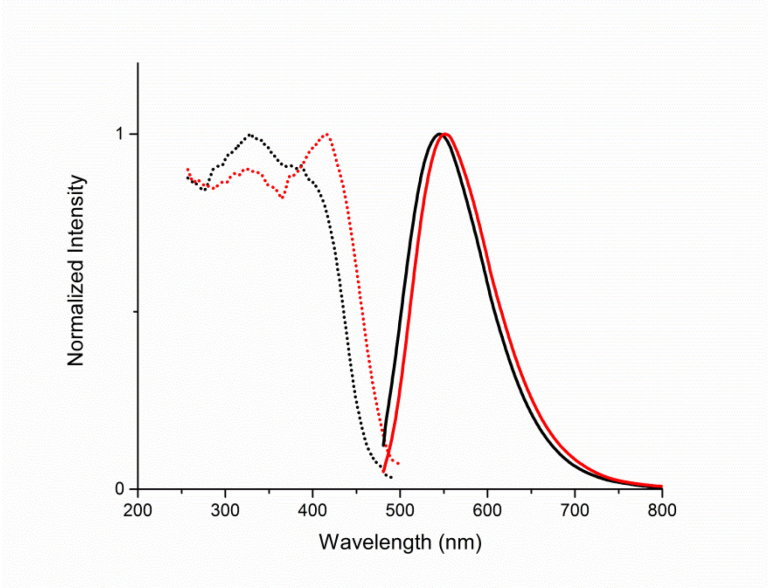
1
0
Normalized Intensity
200
300
400
500
600
700
800
Wavelength (nm)

(b)

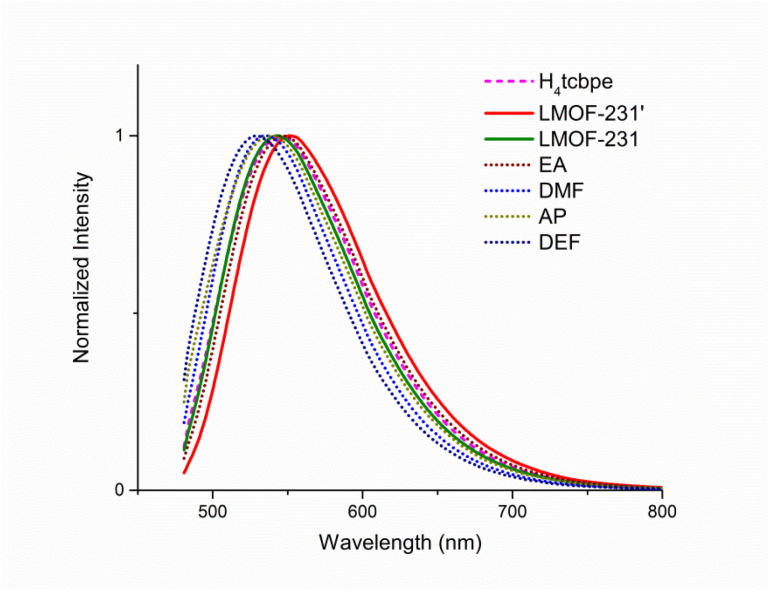

(c)

Figure 50. (a) Optical absorption spectra of H_4tcbpe, LMOF-231, and LMOF-231'. (b) Excitation spectra of H_4tcbpe (black dotted) and LMOF-231' (red dotted). Emission spectra of H_4tcbpe (black solid) and LMOF-231' (red solid) at λ_{ex} = 455 nm. (c) Emission spectra of H_4tcbpe, LMOF-231', and solvent exchanged LMOFs. Solvent abbreviation: ethyl acetate (EA), acetophenone (AP), N,N'-diethylformamide (DEF). All emission spectra were acquired with λ_{ex} = 455 nm.

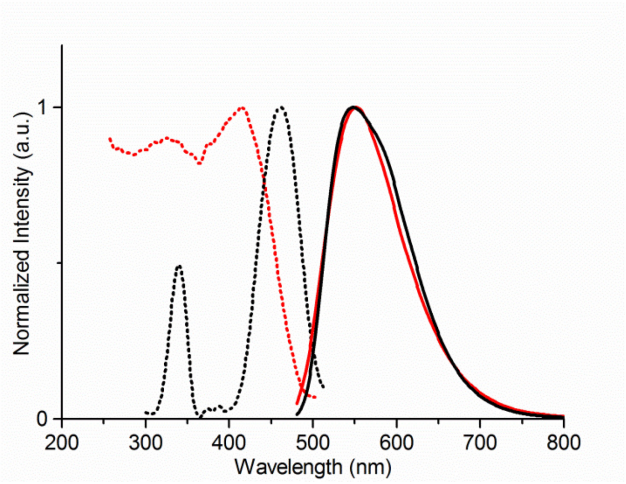

Figure 51. Excitation (dotted line) and emission (solid line) spectra of LMOF-231' (red) and YAG:Ce^{3+} (black)

Table 11. Photophysical properties of H_4tcbpe and LMOF-231

Internal Quantum Yield (%)				
Sample	λ_{ex} = 420 nm	λ_{ex} = 440 nm	λ_{ex} = 455 nm	λ_{em} (nm) [b]
H_4tcbpe	70.3±0.1	63.2±0.1	62.3±0.1	540
LMOF-231'	95.1±0.2	81.3±0.1	76.4±0.2	550
TF@LMOF-231' [a]	92.2±0.1 [c]	80.9±0.1	73.2±0.1	550
LMOF-231'·DMA	82.5±0.1	74.7±0.1	72.2±0.1	540
LMOF-231'·DMF	92.4±0.1	73.6±0.1	73.7±0.1	535
LMOF-231'·DEF	81.0±0.1	71.7±0.1	71.5±0.1	530
LMOF-231'·EA	93.9±0.1	81.1±0.6	76.3±0.1	545
LMOF-231'·AP	72.1±0.1	68.0±0.1	60.3±0.1	540

External Quantum Yield (expressed as % of Internal Quantum Yield)					
Sample	λ_{ex} = 400 nm	λ_{ex} = 415 nm	λ_{ex} = 440 nm	λ_{ex} = 455 nm	λ_{em} (nm) [b]
LMOF-231	96.0	94.2	80.6	64.6	540
LMOF-231'	96.5	96.0	93.3	88.7	550

Thermal stability [d] (Decrease in Percent Intensity, ±2%)					
Sample	100 °C	120 °C	150 °C	160 °C	λ_{em} (nm) [b]
TF@LMOF-231'	1	2	10	15	550

[a] Teflon protected sample in 120 °C oven for 12 h. [b] λ_{ex} = 455 nm. λ_{em} has a ±2 nm deviation. [c] λ_{ex} = 415 nm [d] Sample under different temperatures for 12 h, λ_{ex} = 455 nm.

Room temperature optical absorption, emission, and quantum yield measurements were performed on both as-made and outgassed samples of LMOF-231 in air. With a 2.55 eV optical band gap, LMOF-231 exhibits ligand based emission in the near-yellow region. The evacuation of LMOF-231 gives rise to the guest-free LMOF-231' with a lower band gap of 2.30 eV (Figure 50). Susceptible to a wide range of excitation energy, the emission of LMOF-231' falls right into the yellow region (Figure 51). The immobilization of the H_4tcbpe ligand into a rigid framework has two advantages: The rotation and torsion of phenyl rings are further inhibited, leading to increased quantum yield (Table 11).[175] The emission peak is red shifted to 550 nm in the guest-free sample producing a more yellow

color (Figure 50). The IQYs of the as-made and outgassed LMOF-231 measured at blue excitation (λ_{ex} = 420 nm) are 82.5% and 95.1%, respectively (Table 11), which rival that of the commercial available phosphor YAG:Ce^{3+} (IQY = ~95%) and are the highest among all rare-earth-free blue-excitable yellow phosphors reported to date. In addition, high external quantum yield (EQY) values are obtained (Table 11). For outgassed sample, the value is as high as 96.5% of its internal QY when excited at 400 nm. This result indicates that the material is a very efficient light absorber (close to 100% absorption). The Commission International de I'Eclairage (CIE) coordinates (Figure 52) of LMOF-231' are (0.42, 0.54), nearly identical to those of YAG:Ce^{3+} (0.43, 0.54). The similarity of their emission properties makes LMOF-231' a great candidate as a YAG:Ce^{3+} substitute.

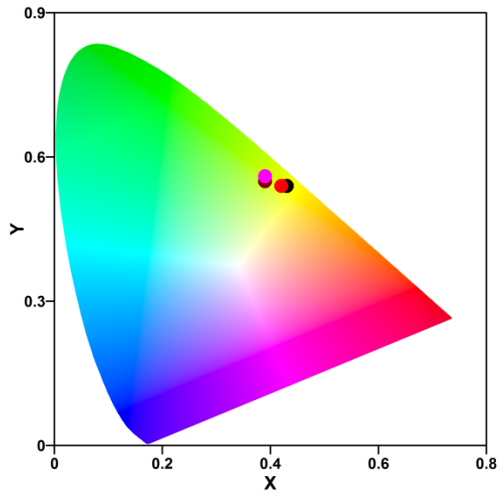

Figure 52. CIE coordionates of YAG:Ce^{3+}, black dot, (0.43, 0.54), H_4tcbpe, burgundy dot, (0.39, 0.55), LMOF-231, pink dot, (0.39, 0.56), and LMOF-231', red dot, (0.42, 0.54) calculated from their emission spectra respectively (λ_{ex} = 455 nm)

The emission color of LMOF-231' is tunable by incorporating different solvents in its pores. To investigate the solvent effect, we studied the photo-physical properties of several solvent exchanged samples. The solvent free form emits closest to yellow, while all

solvents selected in this study unanimously shift the emission peak to the higher energy region (Figure 50): N,N-diethylformamide (DEF) shifts the emission mostly dramatically by 20 nm; (ethyl acetate) EA has the minimal effect (within 5 nm). It is also worth mentioning that solvent incorporation decreases the IQY, possibly due to non-radiative excitation relaxation facilitated by solvent molecules. Therefore, the activation of LMOF-231 serves two purposes: (i) driving the emission peak more towards yellow; (ii) further boosting the IQY of the LMOF (the first boost being the anchoring effect of the framework on the AIE chromophore). We are currently working to find solvents or guest molecules which can shift the emission towards lower energy or drastically change the overall emission profile, as research of this aspect is fundamentally interesting.

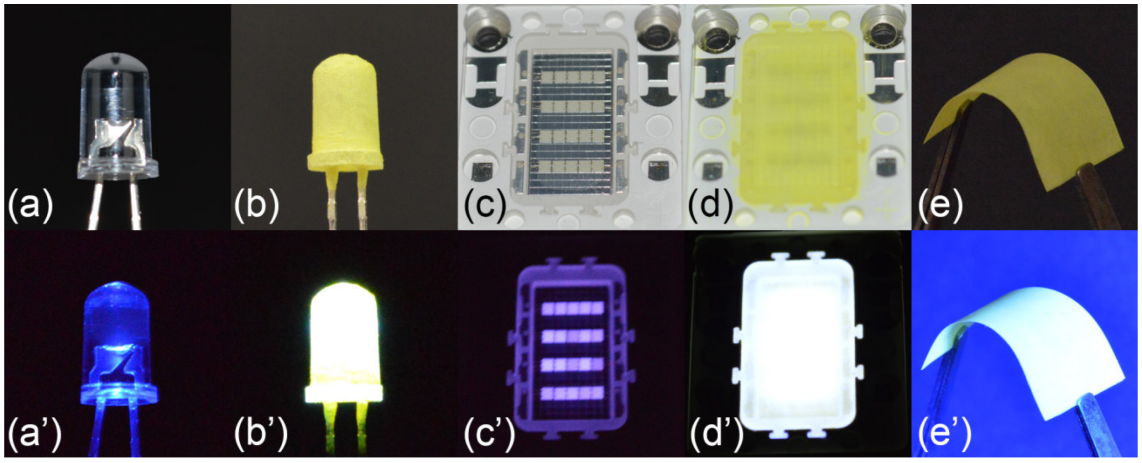

Figure 53. (a) to (d). Blue LED bulb (455-460 nm, (a) and (b)) and plate (450-455 nm, (c) and (d)), before and after coating with solution-processed LMOF-231' to create PC-WLEDs, with the top and bottom rows corresponding to device states 'off' and 'on', respectively. (e) A flexible ribbon coated with LMOF-231' under day light, and blue light (450-470 nm, LED lamp, (e'))

To further assess the performance of LMOF-231' as a yellow phosphor, we built PC-WLED assemblies by coating commercially available blue LEDs with a solution processed sample of LMOF-231'. The solution processiblity of LMOF-231' allows the application of this compound to different types of surfaces, accommodating either LED

bulb or plate, as shown in Figure 53. The luminous efficacy of the PC-WLED (bulb type, 455-460 nm, 5 mm chip, 20 mA, 3V) is as high as 58.9±1.5 lm/W, which is above the current thresholds for LED directional lamps (40 lm/W) and omnidirectional lamps (50 lm/W) with less than 10 W input power set by the US EPA's ENERGY STAR program.[176]

To mimic an actual LED assembly where the phosphor is encapsulated in a transparent plastic shell and test its thermal stability, we sealed the activated powder sample in Teflon (TF@LMOF-231'). A thermal-gravimetric analysis on LMOF-231 indicates the as-made sample loses its solvent content near 160 °C, and the structure maintains its integrity until near 460 °C. Heating TF@LMOF-231' at different temperatures for 12 h has minimum effect on its emission, as the decrease in emission intensity is within 15% after heat treatment from 100 to 160 °C (Table 11). Thus LMOF-231', resistant to elevated temperatures, makes a great phosphor candidate for WLEDs.

3.1.3. Conclusions

In summary, we have designed and synthesized a new AIE-type chromophore, H_4tcbpe. The immobilization of H_4tcbpe into a rigid framework structure shifts the emission of the resulting compound (LMOF-231') further into the yellow region with increased IQY and very high EQY, rivalling that of the commercially available YAG:Ce^{3+}. The thermally stable, rare-earth-free LMOF-231' can be mounted upon various type of surfaces through solution-mediated processes. With all the above merits, this material has great potential as a yellow phosphor for use in PC-WLEDs. Studies on other MOF phosphors built on high performance AIE-type ligands and their derivatives to achieve further enhanced and systematically tunable emission are currently under way.

4. Conclusions

My graduate research revolves around a class of inorganic-organic hybrid materials, namely MOFs. MOFs are crystalline solids constructed via self-assembly of metal cations and organic ligands. The organic ligands often contain aromatic moieties that are subject to excitation, giving rise to optical emission upon irradiation. My primary research interests are exploring the ligand-based emissions in MOFs and studying their applications to chemical sensing and solid-state lighting.

The detection of hazardous chemicals such as explosives and toxins plays a crucial role in anti-terrorism operations, and therefore has significant impact on homeland security and civilian safety. LMOFs are excellent candidates for chemosensing because their unique structural features, such as tunable porosity and easy-to-functionalize surface, promote strong guest-host interactions. By monitoring the changes in LMOFs' optical emission profiles caused by adsorbed guest molecules, the accurate identification of analytes can be achieved. I also use DFT computations to study the nature of analyte-sensor interactions.

LMOFs can be used as highly efficient rare-earth-free phosphors in PC-WLEDs as well. A common way to fabricate a PC-WLED is to coat a blue-emitting LED with a yellow phosphor such as YAG:Ce^{3+}. Since the price of the crucial component of commercially available phosphors, rare-earth elements, has drastically increased over the past decade, the development of rare-earth-free phosphors becomes increasingly urgent. LMOFs are feasible platforms for developing rare-earth-free phosphors, as we could achieve exceptionally high quantum yields with ligand-based emission. Through our experience, the anchoring effect of LMOFs could increase the quantum yield and thermal stability of their constituent molecular chromophores. With DFT computations, we are able to predict and survey the emissions of molecular chromophores, which allows us to construct LMOFs with desired emissions.

Overall, my research is centered on LMOFs and their applications to chemical sensing and solid-state lighting. I also study the electronic properties of luminescent materials and guest-host interactions from a theoretical perspective.

Appendices

List of Abbreviations

ACQ	aggregation-caused quenching
AIE	aggregation induced emission
AP	acetophenone
bdc-NH_2	2-aminoterephthalate
bdc-OH	2-hydroxyterephthalate
bpdc	4,4'-biphenyldicarboxylate
bpe	1,2-bis(4-pyridyl)ethane)
bpee	1,2-bis(4-pyridyl)ethylene
bpy	4,4'-bipyridine
BuCN	butyronitrile
BZ	benzene
CB	conduction band
CIE	Commission International de I'Eclairage
Cl-BZ	chlorobenzene
CTAB	hexadecyltrimethyl-ammonium bromide
DEF	N,N'-diethylformamide
DFT	density functional theory
DMA	N,N'-dimethylacetamide
DMF	N,N'-dimethylformamide
DMNB	2,3-dimethyl-dinitrobutane
DNT	2,4-dinitrotoluene
DOS	density of states
EA	ethyl acetate
EQY	external quantum yield
Et-BZ	ethylbenzene
H_2tbip	5-(tert-butyl)isophthalic acid
H_4tcbpe	4',4''',4'''',4'''''-(ethene-1,1,2,2-tetrayl)tetrakis ([1,1'-biphenyl]-4-carboxylic acid
H_4tcpe	tetrakis(4-carboxyphenyl)ethylene
hfdc	9H-fluorene-2,7-dicarboxylate
HOMO	highest occupied molecular orbital
IQY	internal quantum yield
IR	infrared
LBS	Lewis basic site
LED	light-emitting diode
LLCT	ligand to ligand charge transfer
LMCT	ligand to metal charge transfer

LMOF	luminescent metal-organic framework
LUMO	lowest unoccupied molecular orbital
mDNB	1,3-dinitrobenzene
MeCN	acetonitrile
MLCT	metal to ligand charge transfer
MOF	metal-organic framework
NB	nitrobenzene
ndc	2,6-naphthalenedicarboxylate
NE	nitroethane
NM	nitromethane
NP	1-nitropropane
NT	2-nitrotoluene
oba	4,4'-oxybis(benzoate)
ofdc	9-oxo-9H-fluorene-2,7-dicarboxylate
OMS	open metal site
PC-WLED	phosphor-converted white light-emitting diode
p-DNB	1,4-dinitrobenzene
PL	photoluminescence
PXRD	powder X-ray diffraction
Q_{st}	heat of adsorption
QY	quantum yield
RDX	1,3,5-trinitroperhydro-1,3,5-triazine
TF	Teflon
TNP	2,4,6-trinitrophenol
TNT	2,4,6-trinitrotoluene
TO	toluene
tpe	tetraphenylethylene
VB	valence band
WLED	white light-emitting diode
YAG:Ce^{3+}	Yttrium Aluminum Garnet doped with Cerium

Notes on Computation

The electronic properties of LMOFs and analytes were evaluated using DFT computations on Gaussian 09 (Chapter 2.1 on Gaussian 03).[105,127] A hybrid functional, B3LYP is most frequently used throughout the study. Through our experience, B3LYP is efficient at locating the true minimum on a potential energy surface. For small molecules (non-metal), the 6-31+G* basis set is recommended. More polarization functions can be added if the system contains substantial amount of long pair electrons; more diffusion functions can be

added if the system contains negative charges. However, neutral systems should be used when possible as computation on a neutral molecule is the most reliable. This means when computing MOF fragments, the dangling bonds (usually carboxylates) should be terminated by hydrogen or methyl groups to ensure a neutral fragment. If the system contains metal elements, the full electron basis set, DGDZVP is recommended, as this basis set can be applied to both metal and non-metal elements and runs fairly fast (does not take much computation time). Basis sets with effective core potentials (ECP) such as SDD, LANL2DZ, and LANL2TZ can be applied to metal elements as well. ECP basis sets are expected to produce more accurate results (especially entropy and enthalpy), but they normally require more computation time. A frequency calculation is recommended at the end of geometry optimization for small molecules to ensure a true minimum (no imaginary frequency). If a system is too large (e.g. a MOF fragment), single-point calculation is recommended to roughly evaluate its electronic properties.

Computational results are only comparable if they are acquired under the same functional and basis set. However, given a certain functional, when an ECP basis set is used for metal elements, computational results are still comparable (e.g. evaluating molecular orbital energy levels between a MOF fragment which contains both metal and non-metal elements and an analyte which only contains non-metal elements) as long as the same basis set is used for the non-metal elements. Another functional M06L, less explored in this study, might be useful for future studies as it is sensitive to weak interactions (e.g. evaluating MOF-analyte interactions). But M06 family is arguably less efficient than B3LYP as it takes more cycles to fully converge and seemingly produces flatter potential energy surface (hard to locate minimum). The choice of functional and basis set should be based on a case-by-case

scenario. There are no perfect functional or basis set for every system. Computational results should always be testified by experimental data if possible.

List of LMOFs

Name	Formular
LMOF-111	RPM**3** $Zn_2(bpdc)_2(bpee)\cdot 2DMF$
LMOF-121	$Zn_2(oba)_2(bpy)\cdot DMA$
LMOF-131	RPM**1** $Zn_3(bpdc)_3(bpy)\cdot 4DMF\cdot H_2O$
LMOF-132	RPM**7** $Zn_3(bpdc)_3(2,2'\text{-dmbpy})\cdot xDMF\cdot yH_2O$
LMOF-133	RPM**8** $Zn_3(bpdc)_3(3,3'\text{-dmbpy})\cdot xDMF\cdot yH_2O$
LMOF-141	RPM**4** $Zn_2(bpdc)_2(bpe)\cdot 2DMF$
LMOF-151	RPM**5** $Zn(bpdc)(bpe)\cdot DMF$
LMOF-161	$Zn_2(ndc)_2(bpe)\cdot 2.25DMF\cdot 0.25H_2O$
LMOF-162	$Zn_2(ndc)_2(bpee)\cdot 2.25DMF\cdot 0.5H_2O$
LMOF-171	$Zn_2(ndc)_2(ted)\cdot xDMF\cdot yH_2O$
LMOF-181	$Zn_2(ndc)_2(bpy)\cdot xDMF$
LMOF-191	$Zn_2(bdc\text{-}OH)_2(ted)\cdot 1.5DMF\cdot 0.3H_2O$
LMOF-192	$Zn_2(bdc\text{-}NH2)_2(ted)\cdot xDMF\cdot yH_2O$
LMOF-201	$Zn_2(ofdc)_2(bpy)\cdot 2.5DMF\cdot 1.25H_2O$
LMOF-202	$Zn_2(hfdc)_2(bpy)\cdot xDMA$
LMOF-211	$Zn_2(ofdc)_2(bpe)$
LMOF-212	$Zn_2(hfdc)_2(bpe)\cdot xDMA$
LMOF-221	$Zn_2(ofdc)_2(bpee)\cdot xDMF$
LMOF-222	$Zn_2(hfdc)_2(bpee)$
LMOF-231	$Zn_2(tcbpe)\cdot xDMA$
LMOF-232	$Zr_x(tcbpe)_y\cdot zDMF$
LMOF-233	$Zr_x(tcbpe)_y\cdot zDMA$
LMOF-234	$Zr_x(tcbpe)_y\cdot zDEF$
LMOF-241	$Zn_2(bpdc)_2(tppe)$
LMOF-251	$[Zn_6(btc)_4(tppe)_2(DMA)_2]\cdot 9DMA\cdot 12H_2O$
LMOF-252	$[Zn_x(btc\text{-}f)_y(tppe)_z(DMA)_m]\cdot nDMA$
LMOF-261	$Zn_x(ofdc)_y(tppe)_z$
LMOF-262	$Zn_x(hfdc)_y(tppe)_z$
LMOF-271	$Zn_x(hfipbb)_y(tppe)_z$
LMOF-281	$Zn_2(bdc\text{-}OH)_2(bpe)$
LMOF-282	$Zn_2(bdc\text{-}NH_2)_2(bpe)$
LMOF-291	$Zn_2(bdc\text{-}OH)_2(bpee)$
LMOF-292	$Zn_2(bdc\text{-}NH_2)_2(bpee)$

References

(1) Perry Iv, J. J.; Perman, J. A.; Zaworotko, M. J. *Chemical Society Reviews* **2009**, *38*, 1400.

(2) O'Keeffe, M.; Yaghi, O. M. *Chemical Reviews* **2012**, *112*, 675.
(3) Furukawa, H.; Cordova, K. E.; O'Keeffe, M.; Yaghi, O. M. *Science* **2013**, *341*.
(4) Li, M.; Li, D.; O'Keeffe, M.; Yaghi, O. M. *Chemical Reviews* **2014**, *114*, 1343.
(5) Cook, T. R.; Zheng, Y.-R.; Stang, P. J. *Chemical Reviews* **2013**, *113*, 734.
(6) Janiak, C. *Dalton Transactions* **2003**, 2781.
(7) Meek, S. T.; Greathouse, J. A.; Allendorf, M. D. *Advanced Materials* **2011**, *23*, 249.
(8) Murray, L. J.; Dinca, M.; Long, J. R. *Chemical Society Reviews* **2009**, *38*, 1294.
(9) Makal, T. A.; Li, J.-R.; Lu, W.; Zhou, H.-C. *Chemical Society Reviews* **2012**, *41*, 7761.
(10) Suh, M. P.; Park, H. J.; Prasad, T. K.; Lim, D.-W. *Chemical Reviews* **2012**, *112*, 782.
(11) Sumida, K.; Rogow, D. L.; Mason, J. A.; McDonald, T. M.; Bloch, E. D.; Herm, Z. R.; Bae, T.-H.; Long, J. R. *Chemical Reviews* **2012**, *112*, 724.
(12) Li, J.-R.; Sculley, J.; Zhou, H.-C. *Chemical Reviews* **2012**, *112*, 869.
(13) Wu, H.; Gong, Q.; Olson, D. H.; Li, J. *Chemical Reviews* **2012**, *112*, 836.
(14) Zhang, Z.; Zhao, Y.; Gong, Q.; Li, Z.; Li, J. *Chemical Communications* **2013**, *49*, 653.
(15) Nugent, P.; Belmabkhout, Y.; Burd, S. D.; Cairns, A. J.; Luebke, R.; Forrest, K.; Pham, T.; Ma, S.; Space, B.; Wojtas, L.; Eddaoudi, M.; Zaworotko, M. J. *Nature* **2013**, *495*, 80.
(16) Lee, J.; Farha, O. K.; Roberts, J.; Scheidt, K. A.; Nguyen, S. T.; Hupp, J. T. *Chemical Society Reviews* **2009**, *38*, 1450.
(17) Ma, L.; Abney, C.; Lin, W. *Chemical Society Reviews* **2009**, *38*, 1248.
(18) Yoon, M.; Srirambalaji, R.; Kim, K. *Chemical Reviews* **2012**, *112*, 1196.
(19) Zhang, J.; Biradar, A. V.; Pramanik, S.; Emge, T. J.; Asefa, T.; Li, J. *Chemical Communications* **2012**, *48*, 6541.
(20) Moon, H. R.; Lim, D.-W.; Suh, M. P. *Chemical Society Reviews* **2013**, *42*, 1807.
(21) Allendorf, M. D.; Bauer, C. A.; Bhakta, R. K.; Houk, R. J. T. *Chemical Society Reviews* **2009**, *38*, 1330.
(22) Chen, B.; Xiang, S.; Qian, G. *Accounts of Chemical Research* **2010**, *43*, 1115.
(23) Cui, Y.; Yue, Y.; Qian, G.; Chen, B. *Chemical Reviews* **2012**, *112*, 1126.
(24) Kreno, L. E.; Leong, K.; Farha, O. K.; Allendorf, M.; Van Duyne, R. P.; Hupp, J. T. *Chemical Reviews* **2012**, *112*, 1105.
(25) Liu, B. *Journal of Materials Chemistry* **2012**, *22*, 10094.
(26) Zhang, W.; Xiong, R.-G. *Chemical Reviews* **2012**, *112*, 1163.
(27) Wang, C.; Zhang, T.; Lin, W. *Chemical Reviews* **2012**, *112*, 1084.
(28) Sava, D. F.; Rohwer, L. E. S.; Rodriguez, M. A.; Nenoff, T. M. *Journal of the American Chemical Society* **2012**, *134*, 3983.
(29) Rybak, J.-C.; Hailmann, M.; Matthes, P. R.; Zurawski, A.; Nitsch, J.; Steffen, A.; Heck, J. G.; Feldmann, C.; Götzendörfer, S.; Meinhardt, J.; Sextl, G.; Kohlmann, H.; Sedlmaier, S. J.; Schnick, W.; Müller-Buschbaum, K. *Journal of the American Chemical Society* **2013**, *135*, 6896.
(30) Sun, C.-Y.; Wang, X.-L.; Zhang, X.; Qin, C.; Li, P.; Su, Z.-M.; Zhu, D.-X.; Shan, G.-G.; Shao, K.-Z.; Wu, H.; Li, J. *Nature Communications* **2013**, *4*.
(31) Li, Y.; Pang, A.; Wang, C.; Wei, M. *Journal of Materials Chemistry* **2011**, *21*, 17259.
(32) Narayan, T. C.; Miyakai, T.; Seki, S.; Dincă, M. *Journal of the American Chemical Society* **2012**, *134*, 12932.
(33) Morozan, A.; Jaouen, F. *Energy & Environmental Science* **2012**, *5*, 9269.
(34) Sun, L.; Miyakai, T.; Seki, S.; Dincă, M. *Journal of the American Chemical Society* **2013**, *135*, 8185.
(35) Wu, H. B.; Wei, S.; Zhang, L.; Xu, R.; Hng, H. H.; Lou, X. W. *Chemistry – A European Journal* **2013**, *19*, 10804.
(36) Shimizu, G. K. H.; Taylor, J. M.; Kim, S. *Science* **2013**, *341*, 354.

(37) Horcajada, P.; Chalati, T.; Serre, C.; Gillet, B.; Sebrie, C.; Baati, T.; Eubank, J. F.; Heurtaux, D.; Clayette, P.; Kreuz, C.; Chang, J.-S.; Hwang, Y. K.; Marsaud, V.; Bories, P.-N.; Cynober, L.; Gil, S.; Ferey, G.; Couvreur, P.; Gref, R. *Nat Mater* **2010**, *9*, 172.
(38) Della Rocca, J.; Liu, D.; Lin, W. *Accounts of Chemical Research* **2011**, *44*, 957.
(39) Horcajada, P.; Gref, R.; Baati, T.; Allan, P. K.; Maurin, G.; Couvreur, P.; Férey, G.; Morris, R. E.; Serre, C. *Chemical Reviews* **2012**, *112*, 1232.
(40) Tranchemontagne, D. J.; Mendoza-Cortes, J. L.; O'Keeffe, M.; Yaghi, O. M. *Chemical Society Reviews* **2009**, *38*, 1257.
(41) Rocha, J.; Carlos, L. D.; Paz, F. A. A.; Ananias, D. *Chemical Society Reviews* **2011**, *40*, 926.
(42) Zhan, S.-Z.; Li, M.; Zhou, X.-P.; Ni, J.; Huang, X.-C.; Li, D. *Inorganic Chemistry* **2011**, *50*, 8879.
(43) Kang, Y.; Wang, F.; Zhang, J.; Bu, X. *Journal of the American Chemical Society* **2012**, *134*, 17881.
(44) Knorr, M.; Guyon, F.; Khatyr, A.; Strohmann, C.; Allain, M.; Aly, S. M.; Lapprand, A.; Fortin, D.; Harvey, P. D. *Inorganic Chemistry* **2012**, *51*, 9917.
(45) Ni, J.; Wei, K.-J.; Min, Y.; Chen, Y.; Zhan, S.; Li, D.; Liu, Y. *Dalton Transactions* **2012**, *41*, 5280.
(46) Shan, X.-c.; Jiang, F.-l.; Yuan, D.-q.; Zhang, H.-b.; Wu, M.-y.; Chen, L.; Wei, J.; Zhang, S.-q.; Pan, J.; Hong, M.-c. *Chemical Science* **2013**, *4*, 1484.
(47) Zacher, D.; Shekhah, O.; Woll, C.; Fischer, R. A. *Chemical Society Reviews* **2009**, *38*, 1418.
(48) Shekhah, O.; Liu, J.; Fischer, R. A.; Woll, C. *Chemical Society Reviews* **2011**, *40*, 1081.
(49) Lakowicz, J. R. *Principles of Fluorescence Spectroscopy*; 3rd ed.; Springer, 2006.
(50) Sauer, M.; Hofkens, J.; Enderlein, J. *Handbook of Fluorescence Spectroscopy and Imaging: From Single Molecules to Ensembles*; Wiley-VCH Verlag GmbH & Co. KGaA, 2011.
(51) Shustova, N. B.; McCarthy, B. D.; Dincă, M. *Journal of the American Chemical Society* **2011**, *133*, 20126.
(52) Dai, J.-C.; Wu, X.-T.; Fu, Z.-Y.; Hu, S.-M.; Du, W.-X.; Cui, C.-P.; Wu, L.-M.; Zhang, H.-H.; Sun, R.-Q. *Chemical Communications* **2002**, 12.
(53) Chen, W.; Wang, J.-Y.; Chen, C.; Yue, Q.; Yuan, H.-M.; Chen, J.-S.; Wang, S.-N. *Inorganic Chemistry* **2003**, *42*, 944.
(54) Senchyk, G. A.; Bukhan'ko, V. O.; Lysenko, A. B.; Krautscheid, H.; Rusanov, E. B.; Chernega, A. N.; Karbowiak, M.; Domasevitch, K. V. *Inorganic Chemistry* **2012**, *51*, 8025.
(55) He, J.; Zha, M.; Cui, J.; Zeller, M.; Hunter, A. D.; Yiu, S.-M.; Lee, S.-T.; Xu, Z. *Journal of the American Chemical Society* **2013**, *135*, 7807.
(56) Manna, B.; Chaudhari, A. K.; Joarder, B.; Karmakar, A.; Ghosh, S. K. *Angewandte Chemie International Edition* **2013**, *52*, 998.
(57) Tang, Q.; Liu, S.; Liu, Y.; Miao, J.; Li, S.; Zhang, L.; Shi, Z.; Zheng, Z. *Inorganic Chemistry* **2013**, *52*, 2799.
(58) Yang, J.-S.; Swager, T. M. *Journal of the American Chemical Society* **1998**, *120*, 11864.
(59) Toal, S. J.; Trogler, W. C. *Journal of Materials Chemistry* **2006**, *16*, 2871.
(60) Sanchez, J. C.; DiPasquale, A. G.; Rheingold, A. L.; Trogler, W. C. *Chemistry of Materials* **2007**, *19*, 6459.
(61) Germain, M. E.; Knapp, M. J. *Chemical Society Reviews* **2009**, *38*, 2543.
(62) Pramanik, S.; Zheng, C.; Zhang, X.; Emge, T. J.; Li, J. *Journal of the American Chemical Society* **2011**, *133*, 4153.
(63) Wang, J.; Mei, J.; Yuan, W.; Lu, P.; Qin, A.; Sun, J.; Ma, Y.; Tang, B. Z. *Journal of Materials Chemistry* **2011**, *21*, 4056.

(64) Ramachandra, S.; Popovic′ , Z. D.; Schuermann, K. C.; Cucinotta, F.; Calzaferri, G.; De Cola, L. *Small* **2011**, *7*, 1488.
(65) Wei, W.; Huang, X.; Chen, K.; Tao, Y.; Tang, X. *RSC Advances* **2012**, *2*, 3765.
(66) Nagarkar, S. S.; Joarder, B.; Chaudhari, A. K.; Mukherjee, S.; Ghosh, S. K. *Angewandte Chemie International Edition* **2013**, *52*, 2881.
(67) Thomas, S. W.; Joly, G. D.; Swager, T. M. *Chemical Reviews* **2007**, *107*, 1339.
(68) Jayaramulu, K.; Narayanan, R. P.; George, S. J.; Maji, T. K. *Inorganic Chemistry* **2012**, *51*, 10089.
(69) Ma, J.-x.; Huang, X.-f.; Song, X.-q.; Liu, W.-s. *Chemistry – A European Journal* **2013**, *19*, 3590.
(70) Hu, Z.; Pramanik, S.; Tan, K.; Zheng, C.; Liu, W.; Zhang, X.; Chabal, Y. J.; Li, J. *Crystal Growth & Design* **2013**, *13*, 4204.
(71) Banerjee, D.; Hu, Z.; Pramanik, S.; Zhang, X.; Wang, H.; Li, J. *CrystEngComm* **2013**, *15*, 9745.
(72) Pramanik, S.; Hu, Z.; Zhang, X.; Zheng, C.; Kelly, S.; Li, J. *Chemistry – A European Journal* **2013**, *19*, 15964.
(73) Gole, B.; Bar, A. K.; Mukherjee, P. S. *Chemistry – A European Journal* **2014**, *20*, 2276.
(74) Shustova, N. B.; Cozzolino, A. F.; Reineke, S.; Baldo, M.; Dincă, M. *Journal of the American Chemical Society* **2013**, *135*, 13326.
(75) Xu, H.; Rao, X.; Gao, J.; Yu, J.; Wang, Z.; Dou, Z.; Cui, Y.; Yang, Y.; Chen, B.; Qian, G. *Chemical Communications* **2012**, *48*, 7377.
(76) Li, Y.; Zhang, S.; Song, D. *Angewandte Chemie International Edition* **2013**, *52*, 710.
(77) Lin, C.-K.; Zhao, D.; Gao, W.-Y.; Yang, Z.; Ye, J.; Xu, T.; Ge, Q.; Ma, S.; Liu, D.-J. *Inorganic Chemistry* **2012**, *51*, 9039.
(78) Sun, R.; Li, Y.-Z.; Bai, J.; Pan, Y. *Crystal Growth & Design* **2007**, *7*, 890.
(79) Wang, X.-L.; Bi, Y.-F.; Lin, H.-Y.; Liu, G.-C. *Crystal Growth & Design* **2007**, *7*, 1086.
(80) Tian, Z.; Lin, J.; Su, Y.; Wen, L.; Liu, Y.; Zhu, H.; Meng, Q.-J. *Crystal Growth & Design* **2007**, *7*, 1863.
(81) Li, J.-R.; Yu, J.; Lu, W.; Sun, L.-B.; Sculley, J.; Balbuena, P. B.; Zhou, H.-C. *Nature Communications* **2013**, *4*, 1538.
(82) Chen, B.; Wang, L.; Xiao, Y.; Fronczek, F. R.; Xue, M.; Cui, Y.; Qian, G. *Angewandte Chemie International Edition* **2009**, *48*, 500.
(83) Chen, B.; Yang, Y.; Zapata, F.; Lin, G.; Qian, G.; Lobkovsky, E. B. *Advanced Materials* **2007**, *19*, 1693.
(84) Chen, B.; Wang, L.; Zapata, F.; Qian, G.; Lobkovsky, E. B. *Journal of the American Chemical Society* **2008**, *130*, 6718.
(85) Chaudhari, A. K.; Nagarkar, S. S.; Joarder, B.; Ghosh, S. K. *Crystal Growth & Design* **2013**, *13*, 3716.
(86) Hendon, C. H.; Tiana, D.; Fontecave, M.; Sanchez, C.; D'arras, L.; Sassoye, C.; Rozes, L.; Mellot-Draznieks, C.; Walsh, A. *Journal of the American Chemical Society* **2013**, *135*, 10942.
(87) Sanchez, J. C.; Trogler, W. C. *Journal of Materials Chemistry* **2008**, *18*, 3143.
(88) Cox, J. R.; Müller, P.; Swager, T. M. *Journal of the American Chemical Society* **2011**, *133*, 12910.
(89) Salinas, Y.; Martinez-Manez, R.; Marcos, M. D.; Sancenon, F.; Costero, A. M.; Parra, M.; Gil, S. *Chemical Society Reviews* **2012**, *41*, 1261.
(90) Yoon, M.; Srirambalaji, R.; Kim, K. *Chemical Reviews* **2011**, *112*, 1196.

(91) Lin, Q.; Wu, T.; Zheng, S.-T.; Bu, X.; Feng, P. *Journal of the American Chemical Society* **2012**, *134*, 784.
(92) Li, B.; Zhang, Z.; Li, Y.; Yao, K.; Zhu, Y.; Deng, Z.; Yang, F.; Zhou, X.; Li, G.; Wu, H.; Nijem, N.; Chabal, Y. J.; Lai, Z.; Han, Y.; Shi, Z.; Feng, S.; Li, J. *Angewandte Chemie International Edition* **2012**, *51*, 1412.
(93) Tanh Jeazet, H. B.; Staudt, C.; Janiak, C. *Dalton Transactions* **2012**, *41*, 14003.
(94) Lan, A.; Li, K.; Wu, H.; Olson, D. H.; Emge, T. J.; Ki, W.; Hong, M.; Li, J. *Angewandte Chemie International Edition* **2009**, *48*, 2334.
(95) Lan, A.; Li, K.; Wu, H.; Kong, L.; Nijem, N.; Olson, D. H.; Emge, T. J.; Chabal, Y. J.; Langreth, D. C.; Hong, M.; Li, J. *Inorganic Chemistry* **2009**, *48*, 7165.
(96) Wagner, B. D.; McManus, G. J.; Moulton, B.; Zaworotko, M. J. *Chemical Communications* **2002**, 2176.
(97) Lee, E. Y.; Jang, S. Y.; Suh, M. P. *Journal of the American Chemical Society* **2005**, *127*, 6374.
(98) Maspoch, D.; Ruiz-Molina, D.; Veciana, J. *Chemical Society Reviews* **2007**, *36*, 770.
(99) McManus, G. J.; Perry; PerryPerry, M.; Wagner, B. D.; Zaworotko, M. J. *Journal of the American Chemical Society* **2007**, *129*, 9094.
(100) Chen, B.; Ma, S.; Zapata, F.; Lobkovsky, E. B.; Yang, J. *Inorganic Chemistry* **2006**, *45*, 5718.
(101) van Heijnsbergen, D.; von Helden, G.; Meijer, G.; Maitre, P.; Duncan, M. A. *Journal of the American Chemical Society* **2002**, *124*, 1562.
(102) Chaquin, P.; Costa, D.; Lepetit, C.; Che, M. *The Journal of Physical Chemistry A* **2001**, *105*, 4541.
(103) Ma, R.; Yuan, D.; Chen, M.; Zhou, M. *The Journal of Physical Chemistry A* **2009**, *113*, 1250.
(104) Steill, J. D.; Oomens, J. *International Journal of Mass Spectrometry* **2011**, *308*, 239.
(105) M. J. Frisch; G. W. Trucks; H. B. Schlegel; G. E. Scuseria; M. A. Robb; J. R. Cheeseman; J. A. Montgomery; Jr., T. V.; K. N. Kudin; J. C. Burant; J. M. Millam; S. S. Iyengar; J. Tomasi; V. Barone; B. Mennucci; M. Cossi; G. Scalmani; N. Rega; G. A. Petersson; H. Nakatsuji; M. Hada; M. Ehara; K. Toyota; R. Fukuda; J. Hasegawa; M. Ishida; T. Nakajima; Y. Honda; O. Kitao; H. Nakai; M. Klene; X. Li; J. E. Knox; H. P. Hratchian; J. B. Cross; C. Adamo; J. Jaramillo; R. Gomperts; R. E. Stratmann; O. Yazyev; A. J. Austin; R. Cammi; C. Pomelli; J. W. Ochterski; P. Y. Ayala; K. Morokuma; G. A. Voth; P. Salvador; J. J. Dannenberg; V. G. Zakrzewski; S. Dapprich; A. D. Daniels; M. C. Strain; O. Farkas; D. K. Malick; A. D. Rabuck; K. Raghavachari; J. B. Foresman; J. V. Ortiz; Q. Cui; A. G. Baboul; S. Clifford; J. Cioslowski; B. B. Stefanov; G. Liu; A. Liashenko; P. Piskorz; I. Komaromi; R. L. Martin; D. J. Fox; T. Keith; M. A. Al-Laham; C. Y. Peng; A. Nanayakkara; M. Challacombe; P. M. W. Gill; B. Johnson; W. Chen; M. W. Wong; C. Gonzalez; Pople, J. A. Gaussian 03, Revision B.01, Gaussian, Inc., Pittsburgh PA, 2003.
(106) Che, Y.; Gross, D. E.; Huang, H.; Yang, D.; Yang, X.; Discekici, E.; Xue, Z.; Zhao, H.; Moore, J. S.; Zang, L. *Journal of the American Chemical Society* **2012**, *134*, 4978.
(107) Ma, M.; Zacher, D.; Zhang, X.; Fischer, R. A.; Metzler-Nolte, N. *Crystal Growth & Design* **2010**, *11*, 185.
(108) Gopalakrishnan, D.; Dichtel, W. R. *Journal of the American Chemical Society* **2013**, *135*, 8357.
(109) Kolla, P. *Angewandte Chemie International Edition in English* **1997**, *36*, 800.
(110) Uchimiya, M.; Gorb, L.; Isayev, O.; Qasim, M. M.; Leszczynski, J. *Environmental Pollution* **2010**, *158*, 3048.
(111) Ivy, M. A.; Gallagher, L. T.; Ellington, A. D.; Anslyn, E. V. *Chemical Science* **2012**, *3*, 1773.

(112) Lorenzo, N.; Wan, T.; Harper, R.; Hsu, Y.-L.; Chow, M.; Rose, S.; Furton, K. *Analytical and Bioanalytical Chemistry* **2003**, *376*, 1212.
(113) Lai, H.; Leung, A.; Magee, M.; Almirall, J. *Analytical and Bioanalytical Chemistry* **2010**, *396*, 2997.
(114) Zheng, S.-T.; Bu, J. T.; Li, Y.; Wu, T.; Zuo, F.; Feng, P.; Bu, X. *Journal of the American Chemical Society* **2010**, *132*, 17062.
(115) Uebler, J. W.; Pochodylo, A. L.; Staples, R. J.; LaDuca, R. L. *Crystal Growth & Design* **2013**, *13*, 2220.
(116) Hu, Z.; Deibert, B. J.; Li, J. *Chemical Society Reviews* **2014**, *43*, 5815.
(117) Wanderley, M. M.; Wang, C.; Wu, C.-D.; Lin, W. *Journal of the American Chemical Society* **2012**, *134*, 9050.
(118) Li, G.-B.; Fang, H.-C.; Cai, Y.-P.; Zhou, Z.-Y.; Thallapally, P. K.; Tian, J. *Inorganic Chemistry* **2010**, *49*, 7241.
(119) Jiang, H.-L.; Feng, D.; Wang, K.; Gu, Z.-Y.; Wei, Z.; Chen, Y.-P.; Zhou, H.-C. *Journal of the American Chemical Society* **2013**, *135*, 13934.
(120) Xu, H.; Liu, F.; Cui, Y.; Chen, B.; Qian, G. *Chemical Communications* **2011**, *47*, 3153.
(121) Gole, B.; Bar, A. K.; Mukherjee, P. S. *Chemical Communications* **2011**, *47*, 12137.
(122) Xiao, J.-D.; Qiu, L.-G.; Ke, F.; Yuan, Y.-P.; Xu, G.-S.; Wang, Y.-M.; Jiang, X. *Journal of Materials Chemistry A* **2013**, *1*, 8745.
(123) Xue, Y.-S.; He, Y.; Zhou, L.; Chen, F.-J.; Xu, Y.; Du, H.-B.; You, X.-Z.; Chen, B. *Journal of Materials Chemistry A* **2013**, *1*, 4525.
(124) Banerjee, D.; Hu, Z.; Li, J. *Dalton Transactions* **2014**, *43*, 10668.
(125) Hoffmann, R. *Journal of Chemical Physics* **1963**, *39*, 1397.
(126) Whangbo, M.-H.; Hoffmann, R.; Woodward, R. B. *Proceedings of the Royal Society of London. A. Mathematical and Physical Sciences* **1979**, *366*, 23.
(127) M. J. Frisch; G. W. Trucks; H. B. Schlegel; G. E. Scuseria; M. A. Robb; J. R. Cheeseman; G. Scalmani; V. Barone; B. Mennucci; G. A. Petersson; H. Nakatsuji; M. Caricato; X. Li; H. P. Hratchian; A. F. Izmaylov; J. Bloino; G. Zheng; J. L. Sonnenberg; M. Hada; M. Ehara; K. Toyota; R. Fukuda; J. Hasegawa; M. Ishida; T. Nakajima; Y. Honda; O. Kitao; H. Nakai; T. Vreven; J. A. Montgomery, J.; J. E. Peralta; F. Ogliaro; M. Bearpark; J. J. Heyd; E. Brothers; K. N. Kudin; V. N. Staroverov; T. Keith; R. Kobayashi; J. Normand; K. Raghavachari; A. Rendell; J. C. Burant; S. S. Iyengar; J. Tomasi; M. Cossi; N. Rega; J. M. Millam; M. Klene; J. E. Knox; J. B. Cross; V. Bakken; C. Adamo; J. Jaramillo; R. Gomperts; R. E. Stratmann; O. Yazyev; A. J. Austin; R. Cammi; C. Pomelli; J. W. Ochterski; R. L. Martin; K. Morokuma; V. G. Zakrzewski; G. A. Voth; P. Salvador; J. J. Dannenberg; S. Dapprich; A. D. Daniels; O. Farkas; J. B. Foresman; J. V. Ortiz; J. Cioslowski; Fox, D. J. Gaussian 09, Revision C.01, Gaussian, Inc., Wallingford CT, 2010.
(128) Gao, D.; Wang, Z.; Liu, B.; Ni, L.; Wu, M.; Zhang, Z. *Analytical Chemistry* **2008**, *80*, 8545.
(129) Saxena, A.; Fujiki, M.; Rai, R.; Kwak, G. *Chemistry of Materials* **2005**, *17*, 2181.
(130) Al-Taher, F.; Banaszewski, K.; Jackson, L.; Zweigenbaum, J.; Ryu, D.; Cappozzo, J. *Journal of Agricultural and Food Chemistry* **2013**, *61*, 2378.
(131) David G. Schmale III; Munkvold, G. P. *The Plant Health Instructor* **2009**, *DOI: 10.1094/PHI-I-2009-0715-01*.
(132) USFDA *Compliance Program Guidance Manual* **2007**.
(133) Bhat, R.; Rai, R. V.; Karim, A. A. *Comprehensive Reviews in Food Science and Food Safety* **2010**, *9*, 57.
(134) Shephard, G. S. *Chemical Society Reviews* **2008**, *37*, 2468.

(135) Song, S.; Liu, N.; Zhao, Z.; Njumbe Ediage, E.; Wu, S.; Sun, C.; De Saeger, S.; Wu, A. *Analytical Chemistry* **2014**, *86*, 4995.
(136) Yue, S.; Jie, X.; Wei, L.; Bin, C.; Dou Dou, W.; Yi, Y.; QingXia, L.; JianLin, L.; TieSong, Z. *Analytical Chemistry* **2014**, *86*, 11797.
(137) USFDA *CPG Sec. 683.100 Action Levels for Aflatoxins in Animal Feeds* **2014**.
(138) You, L.; Zha, D.; Anslyn, E. V. *Chemical Reviews* **2015**, DOI: 10.1021/cr5005524.
(139) Basabe-Desmonts, L.; Reinhoudt, D. N.; Crego-Calama, M. *Chemical Society Reviews* **2007**, *36*, 993.
(140) Blatov, V. A.; Shevchenko, A. P.; Proserpio, D. M. *Crystal Growth & Design* **2014**, *14*, 3576.
(141) Blatov, V. A.; Proserpio, D. M. *Acta Crystallographica Section A: Foundations of Crystallography* **2009**, *65*, 202.
(142) Farnum, G. A.; LaDuca, R. L. *Crystal Growth & Design* **2010**, *10*, 1897.
(143) Liu, L.; Chen, X.; Qiu, J.; Hao, C. *Dalton Transactions* **2015**, *44*, 2897.
(144) Hu, Z.; Tan, K.; Lustig, W. P.; Wang, H.; Zhao, Y.; Zheng, C.; Banerjee, D.; Emge, T. J.; Chabal, Y. J.; Li, J. *Chemical Science* **2014**, *5*, 4873.
(145) http://www.energystar.gov/?c=cfls.pr_cfls_savings.
(146) http://www.npr.org/2014/01/28/267185097/in-the-dark-about-picking-a-light-bulb-this-faq-can-help.
(147) http://energy.gov/eere/ssl/solid-state-lighting.
(148)http://www.nytimes.com/2013/10/25/nyregion/city-to-fit-all-streetlights-with-energy-saving-led-bulbs.html.
(149) Sheu, J. K.; Chang, S. J.; Kuo, C. H.; Su, Y. K.; Wu, L. W.; Lin, Y. C.; Lai, W. C.; Tsai, J. M.; Chi, G. C.; Wu, R. K. *Photonics Technology Letters, IEEE* **2003**, *15*, 18.
(150) Ki, W.; Li, J. *Journal of the American Chemical Society* **2008**, *130*, 8114.
(151) Ki, W.; Li, J.; Eda, G.; Chhowalla, M. *Journal of Materials Chemistry* **2010**, *20*, 10676.
(152) Roushan, M.; Zhang, X.; Li, J. *Angewandte Chemie International Edition* **2012**, *51*, 436.
(153) Fang, X.; Roushan, M.; Zhang, R.; Peng, J.; Zeng, H.; Li, J. *Chemistry of Materials* **2012**, *24*, 1710.
(154) Zhang, X.; Liu, W.; Wei, G. Z.; Banerjee, D.; Hu, Z.; Li, J. *Journal of the American Chemical Society* **2014**, *136*, 14230.
(155) Dohner, E. R.; Hoke, E. T.; Karunadasa, H. I. *Journal of the American Chemical Society* **2014**, *136*, 1718.
(156) Xie, R.-J.; Hirosaki, N.; Sakuma, K.; Yamamoto, Y.; Mitomo, M. *Applied Physics Letters* **2004**, *84*, 5404.
(157) Jang, H. S.; Jeon, D. Y. *Applied Physics Letters* **2007**, *90*, 041906.
(158) Sava Gallis, D. F.; Rohwer, L. E. S.; Rodriguez, M. A.; Nenoff, T. M. *Chemistry of Materials* **2014**, *26*, 2943.
(159) Xu, H.; Chen, R.; Sun, Q.; Lai, W.; Su, Q.; Huang, W.; Liu, X. *Chemical Society Reviews* **2014**, *43*, 3259.
(160) Shang, M.; Li, C.; Lin, J. *Chemical Society Reviews* **2014**, *43*, 1372.
(161) Bauer, D.; Diamond, D.; Li, J.; McKittrick, M.; Sandalow, D.; Telleen, P.; Shore, J.; Hackworth, J.; Lieder, C.; Consultancy., J.; Fields, F.; Campbell, A.; Vashishat, D.; Wanner, B.; Sandalow, D.; al., e. *Critical Materials Strategy*, U.S. DEPARTMENT OF ENERGY, 2011.
(162) Hu, R.; Leung, N. L. C.; Tang, B. Z. *Chemical Society Reviews* **2014**, *43*, 4494.
(163) Zhang, Y.; Li, D.; Li, Y.; Yu, J. *Chemical Science* **2014**, *5*, 2710.
(164) Shustova, N. B.; Cozzolino, A. F.; Dincă, M. *Journal of the American Chemical Society* **2012**, *134*, 19596.

(165) Li, J.; Hu, Z.; Gong, Q. **4/25/2014**, US Provisional 61984154.
(166) Lin, Q.; Wu, T.; Zheng, S.-T.; Bu, X.; Feng, P. *Chemical Communications* **2011**, *47*, 11852.
(167) He, Y.; Zhou, W.; Qian, G.; Chen, B. *Chemical Society Reviews* **2014**, *43*, 5657.
(168) Motkuri, R. K.; Annapureddy, H. V. R.; Vijaykumar, M.; Schaef, H. T.; Martin, P. F.; McGrail, B. P.; Dang, L. X.; Krishna, R.; Thallapally, P. K. *Nat Commun* **2014**, *5*, 4368.
(169) Deibert, B. J.; Li, J. *Chemical Communications* **2014**, *50*, 9636.
(170) Wang, M. S.; Guo, S. P.; Li, Y.; Cai, L. Z.; Zou, J. P.; Xu, G.; Zhou, W. W.; Zheng, F. K.; Guo, G. C. *Journal of the American Chemical Society* **2009**, *131*, 13572.
(171) Shirasaki, Y.; Supran, G. J.; Bawendi, M. G.; Bulovic, V. *Nat Photon* **2013**, *7*, 13.
(172) Pan, L.; Parker, B.; Huang, X.; Olson, D. H.; Lee; Li, J. *Journal of the American Chemical Society* **2006**, *128*, 4180.
(173) Rosi, N. L.; Eddaoudi, M.; Kim, J.; O'Keeffe, M.; Yaghi, O. M. *Angewandte Chemie International Edition* **2002**, *41*, 284.
(174) Rosi, N. L.; Kim, J.; Eddaoudi, M.; Chen, B.; O'Keeffe, M.; Yaghi, O. M. *Journal of the American Chemical Society* **2005**, *127*, 1504.
(175) Shustova, N. B.; Ong, T.-C.; Cozzolino, A. F.; Michaelis, V. K.; Griffin, R. G.; Dincă, M. *Journal of the American Chemical Society* **2012**, *134*, 15061.
(176) Pacific Northwest National Laboratory, *SSL Pricing and Efficacy Trend Analysis for Utility Program Planning*, U.S. DEPARTMENT OF ENERGY, 2013.
(177) Hu, Z.; Huang, G.; Lustig, W. P.; Wang, F.; Wang, H.; Teat, S.; Banerjee, D.; Zhang, D.; Li, J. *Chemical Communications* **2015**, *51*, 3045.

Acknowledgements of Previous Publications

Chapter 1 is adapted with permission from reference 116. Copyright 2014 The Royal Society of Chemistry.

Chapter 2.1 (including figures and tables) is adapted with permission from reference 70. Copyright 2013 American Chemical Society.

Chapter 2.2 (including figures and tables) is adapted with permission from reference 144. Copyright 2014 The Royal Society of Chemistry.

Chapter 2.3 will be published in the near future.

Chapter 3 (including figures and tables) is adapted with permission from reference 177. Copyright 2015 The Royal Society of Chemistry.